

Smoothed Particle Radiation Hydrodynamics: Two-Moment method with Local Eddington Tensor Closure

T. K. Chan^{*}, Tom Theuns, Richard Bower and Carlos Frenk

Institute for Computational Cosmology, Department of Physics, Durham University, South Road, Durham DH1 3LE, UK

6 July 2021

ABSTRACT

We present a new radiative transfer method (SPH-M1RT) that is coupled dynamically with smoothed particle hydrodynamics (SPH). We implement it in the (task-based parallel) SWIFT galaxy simulation code but it can be straightforwardly implemented in other SPH codes. Our moment-based method simultaneously solves the radiation energy and flux equations in SPH, making it adaptive in space and time. We modify the M1 closure relation to stabilize radiation fronts in the optically thin limit. We also introduce anisotropic artificial viscosity and high-order artificial diffusion schemes, which allow the code to handle radiation transport accurately in both the optically thin and optically thick regimes. Non-equilibrium thermo-chemistry is solved using a semi-implicit sub-cycling technique. The computational cost of our method is independent of the number of sources and can be lowered further by using the reduced speed of light approximation. We demonstrate the robustness of our method by applying it to a set of standard tests from the cosmological radiative transfer comparison project of Iliev et al. The SPH-M1RT scheme is well-suited for modelling situations in which numerous sources emit ionising radiation, such as cosmological simulations of galaxy formation or simulations of the interstellar medium.

Key words: Physical Data and Processes: radiative transfer — software: development — ultraviolet: galaxies — radiation: dynamics — ISM: H II regions

1 INTRODUCTION

Almost everything we know about galaxies and most of what we know about stars comes from studying their radiation. However, radiation is not just a messenger informing us about the sources and sinks of radiation, but may impact gas directly, for example through photo-heating or the suppression of cooling, or by affecting its chemistry. Radiation pressure on gas and dust can also affect the dynamics of the gas directly. Unfortunately, including the effects of radiation in numerical models is challenging: the equation that accounts for the change of intensity of a light ray resulting from emission and absorption is 7 dimensional. To make matters worse, radiation travels at the speed of light, requiring dramatically shorter time-steps than those required to solve the associated hydrodynamics equations.

Progress has been made by concentrating on particular aspects of the impact of radiation. We briefly mention some of these aspects and the codes in which they are implemented, without aiming to be exhaustive. The CLOUDY

code, last described by Ferland et al. (2017), implements in great detail the interaction between radiation and matter in simple geometries assuming equilibrium conditions. CLOUDY has been instrumental in interpreting the spectra of galaxies. Accounting for absorption and re-emission of light by dust in more complex geometries has been implemented using Monte-Carlo radiative transfer in for example the SKIRT (Baes & Camps 2015), SUNRISE (Jonsson 2006), CMACIONIZE (Vandenbroucke & Wood 2018), and AREPO-MCRT (Smith et al. 2020) codes. The resonant scattering of Lyman- α has been implemented by, for example Zheng & Miralda-Escudé (2002); Cantalupo et al. (2005); Verhamme et al. (2006); Smith et al. (2015) and others. Radiation can also regulate star formation through radiative feedback. The infrared radiation on the interstellar medium (ISM) is modelled in, e.g., Turner & Stone (2001); Davis et al. (2012). Radiative feedback is also important in the formation of the first stars and galaxies (e.g Bromm et al. 2009; Kim et al. 2019).

In this paper we concentrate on the propagation of (hydrogen) ionizing photons. Radiative transfer (henceforth RT) of ionizing photons is important in the context of galax-

^{*} Email: (TKC)tsang.k.chan@durham.ac.uk

ies, governing the evolution of HII regions in the interstellar medium (ISM), and in the physics of the intergalactic medium (IGM), which is highly ionized (Gunn & Peterson 1965) by radiation from active galactic nuclei (AGN, Sargent et al. 1980) and massive stars in galaxies (Shapiro & Giroux 1987; Madau & Meiksin 1994). In both situations, the following considerations are relevant to the design of a successful RT implementation: (1) there is no useful symmetry to be exploited; (2) radiation is emitted by numerous sources; and (3) gas and radiation interact under non-equilibrium conditions. In addition, even without including RT, simulating the ISM and the IGM is computationally demanding requiring the inclusion of many other physical processes. These considerations motivate us to build RT on top of an existing hydrodynamics code, and implement a method that is independent of the number of sources.

Smooth Particle Hydrodynamics (SPH) (Lucy 1977; Gingold & Monaghan 1977) is a Lagrangian hydrodynamics scheme that has been applied to a large variety of astrophysical problems (from planet to star to galaxy formation simulations) as well as non-astrophysical problems. In this scheme, the hydrodynamic properties of a fluid are carried by a set of discrete *particles* that move with the fluid and are used to interpolate physical quantities such as density using a smooth function called the ‘kernel’. The method is computationally efficient, highly adaptive in space and time, and can easily be coupled to gravity. Many current state-of-the-art astrophysical hydrodynamics codes are SPH based (e.g. Springel 2005; Hopkins et al. 2014; Schaye et al. 2015; Wadsley et al. 2017; Price et al. 2018; Springel et al. 2020).

We briefly discuss available options for including RT in hydrodynamical codes, especially for transporting ionizing photons. Conceptually most intuitive is direct ray tracing (also called ‘long characteristics’), where each source casts a number of rays and the equation for RT is solved along all rays simultaneously. With a computational cost scaling as $N_{\text{source}} \times N_{\text{sink}}^2$, where N_{source} and N_{sink} are the number of sources and sinks, this method may be accurate but it is also computationally extremely demanding. Approximations to full ray-tracing are possible though, for example using short characteristic (Mihalas et al. 1978; Mellema et al. 2006), hybrid characteristic (Rijkhorst et al. 2006), or adaptive ray-tracing (Abel & Wandelt 2002; Wise & Abel 2011; Kim et al. 2017). While the short characteristic method is faster than the long characteristic methods, its angular resolution is lower (Finlator et al. 2009); it is difficult to handle bright point sources (e.g. Davis et al. 2012); and it has not yet been implemented directly on top of irregular meshes or particle-based codes such as SPH (though see Finlator et al. 2009). Adaptive ray-tracing is fast and can be applied to irregular meshes (and particle methods), so it remains a viable option for RT in SPH, although its computational cost still scales with the number of sources. In cases where the radiation field is largely known, reverse ray-tracing (Kessel-Deynet & Burkert 2000; Altay & Theuns 2013) has been used to calculate the attenuation of ionizing radiation in high density regions. A variation of reverse ray-tracing has proved to be efficiently parallelizable in SPH (e.g. Susa 2006; Hasegawa & Umemura 2010).

An alternative to ray-tracing is to discretize radiation directions in a finite number of cones (Pawlik & Schaye 2008; Petkova & Springel 2011). The scaling of this implementa-

tion is independent of the number of sources provided a ‘cone merging scheme’ is implemented. The method has been applied in reionization simulations (Pawlik et al. 2017). However, the method is still relatively expensive, given that a high number of cones is required to avoid excessive loss of angular resolution. It also requires substantial modifications to the hydrodynamics code, e.g. virtual particles and rotation of cones to improve the angular sampling and avoid artificial radiation spikes. Another strategy, the Monte Carlo method (e.g. Altay et al. 2008; Baek et al. 2009; Graziani et al. 2013), is even more expensive requiring a large number of photon packets to reduce shot noise to acceptable levels.

A different starting point for an RT algorithm is to compute angular and spectral moments of the radiative transfer equation and integrate the resulting ‘moment’ equations numerically. It is the radiation equivalent of integrating the fluid equations rather than the full Boltzmann equation. In both cases, doing so leads to a dramatic reduction in the dimensionality of the problem. Just as in the case of the fluid equations, there is an infinite hierarchy of moment equations which needs to be truncated by a ‘closure relation’. The closure relation is not unique and obtaining a good closure relation is challenging, because it needs to be able to handle the very different nature of the transport of optically thick and optically thin radiation.

RT moment methods vary in terms of the order of the moments used and in the choice of closure relation. Ideally, the closure relation uses only local properties of the gas and the radiation: this makes the computational cost independent of the number of sources and makes the implementation easily parallelisable. Moment methods do not require fine angular discretization - unlike cone-based or short characteristic methods - so the computational cost per cell or particle can be lower.

The ‘Flux Limited Diffusion’ method (FLD, Levermore & Pomraning 1981) solves only for the zeroth moment of the RT equation, which is a diffusion equation provided the time derivative of the first moment is neglected. The speed with which a radiation front propagates is not limited by the speed of light but can be infinite; however, it is possible to impose a ‘flux limiter’ to enforce causality. FLD has been used in many astrophysical simulations (e.g. Turner & Stone 2001; Reynolds et al. 2009; Commerçon et al. 2011; Krumholz & Thompson 2012), some of which use SPH (Whitehouse & Bate 2004). Gnedin & Abel (2001) developed the OTVET method, which also evolves a diffusion equation of radiation energy density, but with a closure relation applicable to optically thin radiation. FLD and OTVET are fast with a compute time that is largely independent of the number of sources.

However, the relatively diffusive nature of transport in FLD makes it hard to preserve the propagation direction of radiation accurately. As a consequence, neither standard FLD nor OTVET cast sharp shadows behind optically thick regions, albeit for slightly different reasons (Hayes & Norman 2003; Gnedin & Abel 2001). The time-step for propagating radiation in these methods is very restrictive as a consequence of the infinite propagation speed of information; thus, it may be more efficient to use an implicit integration scheme. Unfortunately, an implicit method is computationally inefficient in a scheme like SPH for a large neighbour number (Whitehouse & Bate e.g. 2004; Petkova & Springel

e.g. 2009; see also the discussion about the efficiency of the implicit FLD scheme in Skinner & Ostriker 2013).

The ‘Two Moment’ method solves the zeroth and first order moments of the RT equation simultaneously. A popular closure relation for this method was introduced by Levermore (1984) to which we will refer as the ‘M1’ closure relation¹. The M1 method was first used in astrophysics by González et al. (2007), and has also been implemented in other hydrodynamics codes, e.g. grid-based (Aubert & Teyssier 2008, Skinner & Ostriker 2013, Rosdahl et al. 2013, and Kannan et al. 2019) and hybrid schemes (Hopkins et al. 2020).

This computational scheme is accurate up to order v/c (the fluid velocity divided by the speed of light; Buchler 1983) for a single source in the optically thin or thick limits (Levermore 1984). In the optically thick case, it captures the minimum entropy (production) principle in the presence of one preferred direction (Levermore 1996; Dubroca & Feugeas 1999). In the optically thin case, it preserves the radiation’s direction - and hence it can cast shadows - with radiation fronts moving at the speed of light. It may be surprising at first, but this second-order method is generally *faster* than FLD or OTVET if solved explicitly. This is a consequence of the hyperbolic nature of the equations which result in a much less restrictive time-step (Thomas 1998). The speed and accuracy of the method makes it a promising scheme for including RT in astrophysical hydrodynamics calculations.

While the M1 method works well on structured and unstructured meshes, to date, it has not been implemented in SPH. One reason is that SPH has zeroth-order errors under irregular particle distributions meaning that the SPH estimate does not converge to the true value in the limit of vanishing smoothing length (Lucy 1977; Raviart 1985; Lanson & Vila 2008; Dehnen & Aly 2012). Secondly, devising a good artificial dissipation scheme in SPH is not trivial. However, such artificial dissipation is necessary in order to suppress numerical oscillations around discontinuities. As we will demonstrate, the usual scheme, e.g. Price (2008), for implementing artificial dissipation fails when applied to the M1 scheme. Finally, the original M1 closure relation artificially amplifies noise in the optically-thin regime which requires changes to the closure relation.

Despite these difficulties, implementing the M1 RT method in SPH would be highly desirable: SPH is highly adaptive and ideal for problems that are characterised by a very large dynamic range, whereas the M1 method is efficient and accurate in both the optically thick and thin limits². Furthermore, the M1 method can be straightforwardly implemented on top of any SPH code, since the structures of the hydrodynamics equations and radiation moment equations are quite similar. This results in an accurate and fast code that can handle a very large number of sources in a computationally efficient way. As such, the method described in this paper goes some way towards enabling the

inclusion of RT in simulations of galaxy formation as a matter of course.

In this paper, we describe how to incorporate the M1 method into SPH and examine its performance through standard RT problems. We begin in §2 by briefly illuminating the analogy between taking moments of the Boltzmann equation to derive the fluid equations, and taking moments of the RT equation to derive the two-moment method. We then discuss closure relations and discuss our modification to the M1 closure. Next, we show how the SPH equations can be discretized to yield the more accurate gradients required for implementing the two-moment method and discuss ways of capturing discontinuities in the radiation field. We finish §2 by discussing the coupling of radiation to the thermodynamics and chemistry of the gas, explain and discuss the advantages and drawbacks of the ‘reduced speed-of-light’ approximation, and discuss how we inject radiation. In §3, we present the results of tests with a known solution and compare more realistic tests without a known solution to those in the RT code comparison project (Iliev et al. 2006, 2009). In §4, we comment on the strengths and weaknesses of our scheme and compare with other radiative transfer methods. In §5, we briefly summarise our findings and foresee possible improvements in the future.

2 METHODS

In the following, we first describe the two moment method including modifications to the M1 closure relation. We continue by discussing the implementation in SPH as well as the thermo-chemistry solver we employ. The equations contain numerous variables which we have collated for easy reference in Table 1.

2.1 The radiative transfer equation

The radiative transfer equation expresses the constancy of the specific intensity (I ; in $\text{erg cm}^{-2}\text{s}^{-1}\text{Hz}^{-1}\text{sr}^{-1}$) of a beam of light in the absence of sources or sinks and fluid motion (e.g. Pomraning 1973)

$$\frac{1}{c} \frac{\partial}{\partial t} I + \hat{\mathbf{n}} \cdot \frac{\partial}{\partial \mathbf{x}} I = \left(\frac{DI}{Dt} \right)_{SS}. \quad (1)$$

Here, I is a function of position (\mathbf{x}), direction ($\hat{\mathbf{n}}$), frequency (ν) and time (t). The right-hand side term represent sources, sinks, and/or the scattering of photons. In the astronomical literature, I is usually called the ‘surface brightness’, and just as surface brightness suffers from redshifting, but this is not included in Eq. 1. We refer the reader to Buchler (1983) for the derivation of the complete RT equation.

Moment methods drastically simplify the solution of this equation by multiplying Eq. (1) with some function of direction and integrating the resulting equation over solid angle. This yields an infinite number of moment equations, with the hierarchy closed after a finite number of moments by a ‘closure relation’. Solving the resulting RT moment equations is the radiation equivalent of solving the fluid equations rather than the collisional Boltzmann equation. We point the interested reader to a sketch of the derivation of these moment equations and the relation to fluid equations in Appendix

¹ The ‘M’ in ‘M1’ refers to Minerbo, who introduced the maximum entropy closure in Minerbo (1978).

² But it has issues in handling multiple sources in the optically thin region; see §4.

D/Dt	Lagrangian Derivative	5	ρ	gas density	5	\mathbf{v}	gas velocity	5
p	gas pressure	6	χ	opacity	6	\tilde{c}	reduced speed of light	9
\mathbf{f}	radiation flux / gas density	8	\mathbf{F}	radiation flux	8	u	gas internal energy	7
ξ	radiation energy density / gas density	8	\mathbb{P}	radiation stress tensor	8	\mathbb{F}	Eddington tensor	10
e	gas thermal energy	7	E	radiation energy density	8	f_{Edd}	Eddington factor	10
$\hat{\mathbf{n}}$	radiation direction	13	ν	photon frequency	3	Ω	solid angle	2
I	specific intensity	1	\hbar	reduced Planck constant	3	$2\pi\hbar\nu$	spectral mean photon energy	3
ε	optical thickness estimator	18	h	SPH particle size	24	m	SPH particle mass	24
D	diffusion coefficient	27	W	SPH kernel	24	v_{sig}	SPH signal speed	30
ϕ	slope limiter	31	n_γ	photon number density	3	\mathbf{f}_γ	photon number flux	3
x, x_{HI}	neutral hydrogen fraction	38	$\alpha_{\mathbf{f}}, \alpha_\xi$	artificial dissipation factor	36	Λ	combined heating and cooling rate	7
S	injection source rate	7	c	physical speed of light		ϵ_γ	photon-ionization heating per ionization	A5 & 41
σ_γ	photon-ionization cross-section	39 & A2	Ω_i	correction for variable smoothing length	23			

Table 1. A list of variables, including their symbols, names, and the equations they are first used.

D. It is worth recalling that fluid equations, being differential equations, do not properly describe the behaviour of a set of particles in case of discontinuities such as shocks or contact discontinuities. Their numerical integration requires the addition of extra terms (such as ‘artificial viscosity’ or ‘artificial conduction’). The same is true for moments of the RT equation, and we describe the discontinuity capturing scheme below, after we introduce the full moment equations for fluid and radiation combined in the next section.

2.2 Radiation Moments

We convert the specific intensity I to angular moments by integrating over the solid angle:

$$\begin{aligned}
 E_\nu &= \frac{1}{c} \int I d\Omega, \\
 \mathbf{F}_\nu^i &= \int \hat{\mathbf{n}}^i I d\Omega, \\
 \mathbb{P}_\nu^{ij} &= \frac{1}{c} \int \hat{\mathbf{n}}^i \hat{\mathbf{n}}^j I d\Omega,
 \end{aligned} \tag{2}$$

When additionally integrated over frequency (in the ‘grey’ approximation, e.g. Turner & Stone 2001), those angular moments become radiation energy density E , radiation flux \mathbf{F} and radiation stress tensor \mathbb{P} , respectively. Integrating over small frequency intervals, in order to mimic

multi-frequency RT, is challenging when Doppler shifts or redshifts are large. This case is not considered here.

The relations between the photon number density, n_γ , and the radiation energy density, E , and between the photon flux, \mathbf{F}_γ and the radiation flux, \mathbf{F} , are

$$n_\gamma = \frac{E}{2\pi\hbar\nu}; \quad \mathbf{F}_\gamma \approx \frac{\mathbf{F}}{2\pi\hbar\nu}, \tag{3}$$

where the mean photon energies $2\pi\hbar\nu$ are

$$\begin{aligned}
 \hbar\nu &= \left[\int I d\Omega d\nu \right] \left[\int (I/\hbar\nu) d\Omega d\nu \right]^{-1}; \\
 \hbar\nu &\approx \left[\int \hat{\mathbf{n}} I d\Omega d\nu \right] \left[\int \hat{\mathbf{n}} (I/\hbar\nu) d\Omega d\nu \right]^{-1}.
 \end{aligned} \tag{4}$$

The second relation is a good approximation when the radiation is either isotropic or optically thin. For reference, the mean photon energy $2\pi\hbar\nu$ of ionizing radiation is 29.6eV for a black-body spectrum at $T = 10^5\text{K}$; \hbar is Planck’s constant divided by 2π (see Appendix A for details).

We further defined the ratio of the radiation energy density over the fluid’s density, $\xi \equiv E/\rho$, and the ratio of radiation flux over the fluid’s density as $\mathbf{f} \equiv \mathbf{F}/\rho$.

2.3 Two-moment equations

The moment equations describing the interaction of gas with radiation are (e.g. Buchler 1983; Mihalas & Mihalas 1984):

$$\frac{D\rho}{Dt} + \rho \nabla \cdot \mathbf{v} = 0, \quad (5)$$

$$\frac{D\mathbf{v}}{Dt} = -\frac{\nabla p}{\rho} - \nabla \phi + \frac{\chi \rho}{\tilde{c}} \mathbf{f} + \mathbf{S}_v, \quad (6)$$

$$\frac{Du}{Dt} = -\frac{p}{\rho} \nabla \cdot \mathbf{v} + \Lambda_u + S_u, \quad (7)$$

$$\frac{D\xi}{Dt} = -\frac{1}{\rho} \nabla \cdot (\rho \mathbf{f}) - \frac{\nabla \mathbf{v} : \mathbb{P}}{\rho} + \Lambda_\xi + S_\xi, \quad (8)$$

$$\frac{1}{\tilde{c}^2} \frac{D}{Dt} \mathbf{f} = -\frac{\nabla \cdot \mathbb{P}}{\rho} - \frac{\chi \rho}{\tilde{c}} \mathbf{f} + \mathbf{S}_f, \quad (9)$$

$$\mathbb{P} = \mathbb{F}E = \mathbb{F}\rho\xi. \quad (10)$$

These equations are series expansions including all terms up to v/c , in which properties of the radiation field are measured in the local fluid frame. As such, they (partially) account for changes in radiation energy density due to fluid velocities (Buchler 1983). A list of variable descriptions is given in Table 1.

Eqs. (5-7) express the local conservation of mass, momentum, and energy respectively. The fluid variables are mass density (ρ), velocity (\mathbf{v}), pressure (p), and thermal energy per unit mass (u); $\nabla \phi$ is the gravitational acceleration. D/Dt is the Lagrangian time derivative. The terms \mathbf{S}_v and S_u are sources or sinks for the injection of momentum and energy respectively, e.g. due to feedback from stars. The term Λ_u is the combined heating and cooling rate. The case of photo-heating and radiative cooling will be discussed in detail in §2.8. Finally, the term $(\chi\rho/\tilde{c})\mathbf{f}$ represents radiation pressure³. Here, \tilde{c} is the reduced speed of light (see §2.11) and χ is the opacity related to the optical depth per unit length as $d\tau/dr = \chi\rho$.

Eqs. (8-9) express the local conservation of radiation energy and momentum respectively. The radiation variables are radiation energy per unit mass (ξ), radiation flux per unit mass (\mathbf{f}), and the ‘radiation stress tensor’ (\mathbb{P}). $\nabla \mathbf{v} : \mathbb{P}$ is short hand for the contraction $\mathbb{P}^{ij}v_{i,j}$. In Eq. (10), the tensor \mathbb{F} is the Eddington tensor, which we will discuss in §2.4.

Some further source/sink terms appear on the right-hand sides of Eqs. (8-9). Λ_ξ is the rate at which the radiation density changes due to heating and cooling, discussed in

³ Currently, we apply radiation pressure inferred from the quantities averaged over the volume of each particle. However, Hopkins & Grudić (2019) demonstrated that it is more accurate to apply radiation pressure to the interface between particles, an improvement we intend to implement in future. In the case of ionizing radiation propagating through a low resolution simulation - for example when simulating cosmic reionization - the resulting differences are expected to be small because the radiation imparts little momentum. However, a more accurate treatment of radiation pressure may be required in high-resolution simulations to capture radiation pressure from massive stars or active galactic nuclei.

more detail in §2.8. S_ξ and \mathbf{S}_f are the source terms for radiation energy and flux, respectively. The injection of radiation will be described in more detail in §2.9.

In this paper we propagate radiation at the speed $\tilde{c} < c$, which is a ‘reduced’ speed of light. The motivation, validity and limitations of this approximation are discussed in §2.11.

In the two-moment method, the time derivatives of the radiation density and radiation flux are kept, unlike in the case of flux limited diffusion (FLD, Levermore & Pomraning 1981). There are some advantages in keeping this term. Firstly, Buchler (1983) showed that the time derivative of \mathbf{f} may be significant in the optically thin (free streaming) regime, making the two-moment method more accurate than FLD. Secondly, because of this time derivative, M1 can maintain the direction of the radiation, whereas in FLD the radiation follows the gradient in energy density and hence incorrectly goes around corners in the optically thin limit.

Finally, including the time derivative yields hyperbolic equations rather than the parabolic equation of FLD. Solving a parabolic differential equation explicitly requires a more restrictive timestep, $\Delta t \propto (\Delta x)^2/\tilde{c}$, compared to the hyperbolic case where $\Delta t \propto \Delta x/\tilde{c}$; where Δx is the spatial resolution. Combined with using a reduced speed of light approximation (\tilde{c} rather than c) improves the efficiency of the RT implementation compared to FLD⁴.

2.4 Closure relation

Taking successive angular moments of the RT relation leads to an infinite set of coupled moment equations (Mihalas & Mihalas 1984). A ‘closure relation’ which relates higher order moments to lower-order ones, is required to break this hierarchy. Unfortunately, the closure relation is not unique and depends on the problem at hand. Levermore (1984) derived a closure relation as follows. We consider the RT equations assuming $\mathbf{v} = 0$ and additionally neglecting the Λ and S terms. Then, Eqs. (8) and (9) simplify to the following two moment equations:

$$\frac{\partial E}{\partial t} = -\nabla \cdot \mathbf{F}, \quad (11)$$

$$\frac{1}{\tilde{c}^2} \frac{\partial}{\partial t} \mathbf{F} = -\nabla \cdot \mathbb{P} - \frac{\chi \rho}{\tilde{c}} \mathbf{F}. \quad (12)$$

Provided that the radiation field is symmetric around a given direction $\hat{\mathbf{n}}$, Levermore (1984) demonstrated that the second moment can be written as

$$\mathbb{P} = \mathbb{F}E = \frac{E}{2}(1 - f_{\text{Edd}})\mathbb{I} + \frac{E}{2}(3f_{\text{Edd}} - 1)\hat{\mathbf{n}}\hat{\mathbf{n}}, \quad (13)$$

where f_{Edd} is called the ‘Eddington factor’.

When the radiation field is *almost* isotropic, $\mathbb{P}_{ij} \approx (E/3)\delta_{ij}$ which corresponds to $f_{\text{Edd}} = 1/3$. Combining the two moment equations with this relation yields

$$\frac{\partial E}{\partial t} = \nabla \cdot \left(\frac{\tilde{c}}{3\chi\rho} \nabla E \right) - \nabla \cdot \left(\frac{1}{\tilde{c}\chi\rho} \frac{\partial \mathbf{F}}{\partial t} \right). \quad (14)$$

This describes isotropic diffusion of the energy density, E , in case the rate of change of the flux (the last term on the

⁴ The M1 method can be faster even if FLD is solved implicitly because the inversion step in the implicit solver is expensive (see, e.g. Skinner & Ostriker 2013).

right hand side) can be neglected. Of course, if the radiation field were exactly isotropic everywhere it has to be uniform as well - but this diffusion approximation can be used, provided E varies sufficiently slowly in space and time (Levermore 1984). This case corresponds to the classical ‘Eddington’ approximation for the propagation of radiation in the isotropic case, and we will refer to as the ‘optically-thick’ solution.

In contrast, the value $f_{\text{Edd}} = 1$ leads to anisotropic radiation propagation with

$$\nabla \cdot \mathbb{P} = \hat{\mathbf{n}} (\hat{\mathbf{n}} \cdot \nabla E). \quad (15)$$

In this ‘optically-thin’ case,

$$\frac{\partial^2 E}{\partial t^2} + \tilde{c}^2 (\hat{\mathbf{n}} \cdot \nabla)^2 E = -\tilde{c} \chi \rho \frac{\partial E}{\partial t}, \quad (16)$$

and radiation ‘streams’ in direction $\hat{\mathbf{n}}$ with speed \tilde{c} , with its intensity decreasing due to absorption as quantified by the right hand side of the equation.

The closure relation of Eq. (13) therefore captures the propagation correctly in the two limiting cases of (1) high-optical depth, with the solution describing isotropic diffusion, and (2) the optically-thin regime of negligible optical depth, where the solution describes free propagation at the speed \tilde{c} in the characteristic direction $\hat{\mathbf{n}}$. The expectation is then that Eq. (13) also provides a good approximation to any intermediate case (Levermore & Pomraning 1981).

One disadvantage of the scheme is that radiation behaves as a ‘collisional’ fluid: beams of light with different propagation directions $\hat{\mathbf{n}}$ that intersect will collide. This is because the local Eddington tensor closure relation of Eq. (13) can only handle one direction $\hat{\mathbf{n}}$ at a time (in addition to an isotropic component). We will discuss this issue in more details in §4.1.1.

2.4.1 Choice of Eddington factor

Next we turn to the choice of f_{Edd} . As shown by Levermore (1984), given that $\mathbf{F}/(\tilde{c}E)$ and \mathbb{P}/E are the first and second moments of a non-negative unit density variable requires that

$$\varepsilon^2 = \left| \frac{\mathbf{F}}{\tilde{c}E} \right|^2 = \left| \frac{\mathbf{f}}{\tilde{c}\xi} \right|^2 \leq f_{\text{Edd}} \leq 1, \quad (17)$$

which we term the ‘original’ closure.

Of course, even if we demanded that the Eddington factor should only depend on the local values of \mathbf{F} and E , then this would not specify f_{Edd} uniquely (see Levermore 1984 for a summary of reasonable choices). One particular choice is the ‘M1’ closure, which Levermore (1984) derived by assuming that there exist inertial frames in which the radiation density is isotropic (not necessarily isotropic in the lab or fluid frame). This original M1 relation is

$$f_{\text{Edd}} = \frac{3 + 4\varepsilon^2}{5 + 2\sqrt{4 - 3\varepsilon^2}}. \quad (18)$$

Dubroca & Feugeas (1999) showed that this corresponds to the simplest moment closure that maximizes the entropy and is anisotropic⁵.

⁵ Note that in the mathematics community, the entropy has the opposite sign compared to that in the physics community.

The evaluation of this expression for M1 is computationally efficient as well as highly parallelisable, as compared to e.g. ray-tracing or Monte Carlo methods, because f_{Edd} depends only on local quantities. Because of this, several astrophysical RT implementations use this M1 closure relation, e.g. González et al. (2007); Aubert & Teyssier (2008); Skinner & Ostriker (2013); Rosdahl et al. (2013); Kannan et al. (2019); Skinner et al. (2019). However, this choice is not without its problems (as are other variants based on local variables). Firstly, consider the case of two otherwise identical beams of radiation propagating in opposite directions. Where the beams hit the net flux is zero, $|\mathbf{f}/(\tilde{c}\xi)| \sim 0$ so that $\varepsilon = 0$ and $f_{\text{Edd}} = 1/3$: this corresponds to the optically-thick solution, even in the system were optically thin. It is as if the beams of radiation collide with each other (see also Rosdahl et al. 2013). Clearly, this behaviour is incorrect.

This choice of closure relation also results in artificial dispersion, since radiation does not move at the same speed when $|\mathbf{f}/(\tilde{c}\xi)|$ varies: radiation propagates with speed between $\tilde{c}/3$ and \tilde{c} , when Eq. (14) or Eq. (16) applies, respectively.

An improved closure relation can be derived from the following considerations. In the optically thick limit, we desire that $f_{\text{Edd}} = 1/3$, since the corresponding isotropic diffusion captures the random walks of photons through the medium as a consequence of numerous independent scattering events. In the opposite limit of an optically thin medium, we desire that $f_{\text{Edd}} = 1$, since that correctly describes streaming of radiation at the speed of light. Note that in this strategy, we set $f_{\text{Edd}} = 1$ only according to the optical depth (τ) and independent of $|\mathbf{f}/(\tilde{c}\xi)|$, since the latter can be small even in the optically thin regime, e.g. head-on collision. Finally, we require that $f_{\text{Edd}} \leq 1$.

Our proposed ‘modified’ M1 closure relation is

$$\varepsilon = \max[\exp(-\tau), |\mathbf{f}/(\tilde{c}\xi)|], \quad (19)$$

where $\tau \equiv \chi \rho h$ is the local optical depth across the extent h of a resolution element. This choice satisfies $\varepsilon \leq 1$, and has the correct limiting behaviour. In the optically thin limit ($\tau \rightarrow 0$), $\varepsilon \rightarrow 1$, while in the optically thick case ($\tau \rightarrow \infty$), $\varepsilon \rightarrow |\mathbf{f}/(\tilde{c}\xi)| \rightarrow 0$, since the flux $|\mathbf{f}|$ is small. In case $|\mathbf{f}|$ is small due to the ‘collision’ of two beams of radiation, ε can still be of order 1 and describe radiation streaming rather than diffusion provided the optical depth is small. We will demonstrate in §4.1.1 that our modified M1 closure (Eq.19) can handle head-on beam collisions and more generally, 1D RT problems.

We choose to modify M1 by the factor $\exp(-\chi \rho h)$ to mimic the diffusion of radiation when the optical depth is large. The choice is also motivated by a desire to help numerical convergence: the combined contributions of two resolution elements, for example two SPH particles with extents h_i and h_j , is approximately $\exp(-\chi \rho h_i) \times \exp(-\chi \rho h_j) = \exp[-\chi \rho (h_i + h_j)]$, which corresponds to the approximate effect of a lower resolution SPH particle with size $(h_i + h_j)$.

We will also show in Fig.1 that our scheme is more stable than the original M1 closure in optically thin regions when simulated with SPH. However, the scheme does not solve the problem of the artificial collision of radiation beams in case they are not head on (§4.1.1), since the radiation directions will still merge locally according to Eq. (13). For-

tunately, even in this case, our closure (Eq. 19) will still prevent the numerical diffusion in the optically thin limit.

Finally, we justify the use of physical quantities other than radiation energy and flux in the Eddington factor. The Eddington tensor should be derived from the RT equation, which contains information about the gas, e.g. density, velocity, and the opacity (through the collisional term). Thus, the Eddington tensor should be also a function of these gas properties. In fact, in the absence of the collision term ($\chi = 0$), the radiation should always be free streaming at the speed of light regardless of the value of ξ and \mathbf{f} .

2.5 SPH forms for the two moment method and the numerical solution to the propagation equation

In the standard formulation of SPH (e.g. Monaghan 2002), the density, ρ_i , at the location of particle i is calculated through interpolating over ‘neighbouring’ particles in a gather approach,

$$\rho_i = \sum_j m_j W_{ij}(h_i), \quad (20)$$

where the kernel $W_{ij}(h_i) = W(|\mathbf{r}_i - \mathbf{r}_j|, h_i)$ is a function with compact support (by default the M_4 cubic B-spline function), h_i is the smoothing length and m_i the mass of particle i . We follow the variable smoothing length treatment similar to that in Springel & Hernquist (2002) such that the number of neighbour particles that contribute to the sum is $N_{\text{ngb}} (=48 \text{ in } 3\text{D})$ (see the GADGET-2 SPH section in Schaller et al. 2015 for more details, including the SPH formulation of the hydrodynamics in SWIFT).

In the radiation hydrodynamics tests presented below, we do not use the standard SPH formulation but rather the modifications introduced by Borrow et al. (2020) called SPHENIX, which uses the density and energy hydrodynamic variables, rather than pressure and energy. SPHENIX applies the Cullen & Dehnen (2010) shock detector to minimize artificial viscosity away from shocks and the artificial diffusion term to capture fluid mixing described by Price (2008).

One of the main hurdles to overcome for implementing a moment method in SPH is that such a higher-order method requires the calculation of derivatives, and these tend to be noisy when the particle distribution is irregular. For example, there are several ways to estimate the divergence of a vector field \mathbf{X} , which include (e.g. Tricco & Price 2012) the ‘symmetric’ estimate:

$$(\nabla \cdot \mathbf{X})_i|_{\text{sym}} = \rho_i \sum_j m_j \left[\frac{\mathbf{X}_i}{\Omega_i \rho_i^2} \cdot \nabla_i W_{ij}(h_i) + \frac{\mathbf{X}_j}{\Omega_j \rho_j^2} \cdot \nabla_j W_{ij}(h_j) \right], \quad (21)$$

and the ‘difference’ estimate:

$$(\nabla \cdot \mathbf{X})_i|_{\text{diff}} = - \sum_j \frac{m_j}{\Omega_i \rho_i} (\mathbf{X}_i - \mathbf{X}_j) \cdot \nabla_i W_{ij}(h_i), \quad (22)$$

where \mathbf{X} is an arbitrary vector or tensor associated with each particle, and

$$\Omega_i = 1 + \frac{h_i}{3\rho_i} \sum_j m_j \frac{\partial W_{ij}(h_i)}{\partial h_i}, \quad (23)$$

is a correction factor introduced by Springel & Hernquist (2002) to account for spatial variations in the value of the smoothing length, h .

We use the difference form to evaluate Eqs.(8) and (9):

$$\begin{aligned} \left(\frac{D\xi_i}{Dt} \right) \Big|_{\text{diff}} &= \left[-\frac{1}{\rho} \nabla \cdot (\rho \mathbf{f}) \right] \Big|_i \\ &= - \sum_j \frac{m_j}{\Omega_i \rho_i^2} (\rho_i \mathbf{f}_i - \rho_j \mathbf{f}_j) \cdot \nabla_i W_{ij}(h_i), \end{aligned} \quad (24)$$

and

$$\begin{aligned} \left(\frac{1}{\tilde{c}^2} \frac{D\mathbf{f}_i}{Dt} \right) \Big|_{\text{diff}} &= \left[-\frac{\nabla \cdot \mathbb{P}}{\rho} - \frac{\chi \rho \mathbf{f}}{\tilde{c}} \right] \Big|_i \\ &= - \sum_j \frac{m_j}{\Omega_i \rho_i^2} (\rho_i \xi_i \mathbb{F}_i - \rho_j \xi_j \mathbb{F}_j) \cdot \nabla_i W_{ij}(h_i) - \frac{\chi_i \rho_i}{\tilde{c}} \mathbf{f}_i. \end{aligned} \quad (25)$$

The difference formulation subtracts the zeroth-order errors that occur in SPH explicitly, yielding first-order accuracy regardless of the underlying particle distribution. This results in superior numerical estimates of the divergence particularly near steep gradients. However, the difference estimate does not manifestly conserve flux, unlike the ‘symmetric’ estimate⁶. Fortunately, we find that the level of non-conservation of flux is small in our experiments (Typically less than one percent, better accuracy could be reached by increasing the order of the scheme, if required.). There is no known formulation that simultaneously avoids zeroth-order errors and is manifestly conservative in SPH (see the discussion in Price 2012).

We add the term $-\chi_i \rho_i \mathbf{f}_i / \tilde{c}$ to Eq. (9) using operator splitting,

$$\mathbf{f}_i(t + \Delta t) = \exp(-\chi_i \rho_i \tilde{c} \Delta t) \times \mathbf{f}_i(t). \quad (26)$$

Though this scheme is unconditionally stable, it nevertheless yields the wrong answer when the time-step, Δt , is too long. This could be avoided by limiting the time-step to $\Delta t \leq 1/(\chi \rho \tilde{c})$, but that would result in unacceptably short time-steps in regions of high optical depth. Since in such regions the impact of radiation may be small anyway, we will limit the time-step by the usual⁷ Courant–Friedrichs–Lewy (CFL) condition, $\Delta t \leq 0.1 h / \tilde{c}$. To ensure that our results are physically meaningful, numerically stable and satisfy causality, we apply the following additional limiters at the beginning of each time-step: (i) $|\mathbf{f}| \leq \tilde{c} \xi$, (ii) $\xi \geq 0$, and (iii) we zero unused components of \mathbf{f} in 1D or 2D simulations. The latter limiter corrects for any numerical scatter of radiation into unused dimensions, as may happen if the Eddington tensor is non-zero but $|\mathbf{f}|$ is small.

⁶ The ‘symmetric’ SPH form can also help to regularize the particle distribution in hydrodynamics calculations, albeit by introducing purely numerical forces (Price 2012). This is less important when propagating ionising radiation which does not usually exert strong forces on the gas particles.

⁷ In the time-step determination, we will use the smallest h of all neighbouring SPH particles and of the particle itself, to ensure stability and conservation.

2.5.1 Optically thin radiation

In general, we set the propagation direction, $\hat{\mathbf{n}}$, to be that of the local flux, $\hat{\mathbf{n}} = \hat{\mathbf{f}}$. However, radiation propagates in a constant direction in the optically thin case. Since the flux is computed numerically, round-off errors or numerical noise may rotate the flux vector so that imposing $\hat{\mathbf{n}} = \hat{\mathbf{f}}$ does not guarantee that radiation travels in a straight line, even in the optically thin case.

In some special cases, for example of light emanating from a single point source or the propagation of a plane parallel radiation front, the direction $\hat{\mathbf{n}}$ is known a priori, and we can therefore choose to simply impose the propagation direction, and use that direction to compute the optically thin Eddington tensor, Eq. (13).

Not surprisingly, imposing the direction of radiation propagation yields spherical ionization regions around a point source (Fig.8) and casts sharp shadows behind optically thick absorbers even at low resolution (Fig.11). Of course in general, the propagation direction $\hat{\mathbf{n}}$ is not generally known, for example, there may be several sources or an additional isotropic background, which require improvements of our scheme.

2.6 Discontinuity-capturing dissipation terms

The fluid equations encoded in SPH are differential equations and hence need to be supplemented with extra terms in order to correctly capture discontinuities such as shocks and contact discontinuities. These terms broaden discontinuities by introducing numerical dissipation so that they can be resolved by the interpolation scheme (see e.g. Monaghan 1997; Agertz et al. 2007; Price 2008).

The SPH implementation of the moment method needs to be extended with similar dissipation terms to handle discontinuities in the radiation field, and we base these on the artificial diffusion and artificial viscosity terms of the SPH fluid equations. The energy dissipation term is similar to the *artificial diffusion* term in SPH hydrodynamics,

$$\left(\frac{D\xi_i}{Dt}\right)\Big|_{\text{diss}} = \sum_{j=1}^N D_{\xi,ij} \frac{m_j}{\bar{\rho}^2} (\rho_i \tilde{\xi}_i - \rho_j \tilde{\xi}_j) \frac{\hat{\mathbf{r}}_{ij} \cdot \nabla_i \overline{W_{ij}}}{r_{ij}}, \quad (27)$$

where $\bar{\rho} = \sqrt{\rho_i \rho_j}$ is the geometric mean of the densities of the pair of interacting particles i and j . If the density contrast is larger than 10, we found the scheme to be more stable with the choice $\bar{\rho} = \min(\rho_i, \rho_j)$, but this choice is not used in the tests in this paper.

Flux dissipation can be modelled with the *artificial viscosity* term in SPH hydrodynamics⁸,

$$\left(\frac{D\mathbf{f}_i}{Dt}\right)\Big|_{\text{diss}} = \begin{cases} \sum_{j=1}^N D_{\mathbf{f},ij} \frac{m_j}{\bar{\rho}^2} (\rho_i \mathbf{f}_i - \rho_j \mathbf{f}_j) \cdot \hat{\mathbf{r}}_{ij} \frac{\nabla_i \overline{W_{ij}}}{r_{ij}}, & \text{if } (\rho_i \mathbf{f}_i - \rho_j \mathbf{f}_j) \cdot \hat{\mathbf{r}}_{ij} < 0, \\ 0, & \text{otherwise.} \end{cases} \quad (28)$$

In these expressions, $D_{\xi,ij}$ and $D_{\mathbf{f},ij}$ are the ‘artificial dissipation’ coefficients, they have the units of a diffusion constant

and we write them as

$$\begin{aligned} D_{\xi,ij} &= \alpha_{\xi,i} v_{\text{sig},i} h_i + \alpha_{\xi,j} v_{\text{sig},j} h_j, \\ D_{\mathbf{f},ij} &= \alpha_{\mathbf{f},i} v_{\text{sig},i} h_i + \alpha_{\mathbf{f},j} v_{\text{sig},j} h_j. \end{aligned} \quad (29)$$

Here, v_{sig} is the signal speed,

$$v_{\text{sig}} = |\hat{\mathbf{f}} \cdot \hat{\mathbf{r}}_{ij}| \tilde{c}, \quad (30)$$

and $(\alpha_{\mathbf{f}}, \alpha_{\xi}) \leq 1$ are dimensionless numbers that quantify the strength of the numerical dissipation. The forms of Eqs. (27) and (28) are consistent with the Riemann solver across the boundary of two SPH particles (Monaghan 1997). The kernel averaged over smoothing length is $\nabla_i \overline{W_{ij}} = 0.5[\nabla_i W_{ij}(h_j) + \nabla_i W_{ij}(h_j)]$.

Eqs. (27) and (28) are diffusion equations (see e.g. Jubelgas et al. 2004; Price 2008). The maximum value of the diffusion speed is $h\tilde{c}$, where h is the particle size and \tilde{c} is the propagation speed of the radiation. A numerical diffusion coefficient larger than this maximum value will result in numerical instabilities if the time-step is set by the CFL condition, $\Delta t \lesssim h/\tilde{c}$.

Price (2008) set $\rho_i \tilde{\xi}_i = \rho_i \xi_i$, the values associated with individual SPH particles, and minimized the amount of numerical dissipation by choosing how the signal speed depends on local quantities. However, another way to minimize artificial dissipation is by reconstructing fluid quantities at the interface between particles (see e.g. Frontiere et al. 2017; Rosswog 2020a). To do so, we reconstruct the radiation energy density at the interface using a Taylor series expansion,

$$\begin{aligned} \rho_i \tilde{\xi}_i - \rho_j \tilde{\xi}_j &= |\hat{\mathbf{f}} \cdot \hat{\mathbf{r}}_{ij}| \{(\rho_i \xi_i - \rho_j \xi_j) \\ &+ \phi \left[\frac{h_i}{h_i + h_j} \mathbf{r}_{ji} \cdot \nabla(\rho_i \xi_i) - \frac{h_j}{h_i + h_j} \mathbf{r}_{ij} \cdot \nabla(\rho_j \xi_j) \right] \}, \end{aligned} \quad (31)$$

where ϕ is the slope limiter (implemented using the *minmod* function, $\text{minmod}(x) = \max(0, \min(x, 1))$) to minimize spurious oscillations. The term $\hat{\mathbf{f}} \cdot \hat{\mathbf{r}}_{ij}$ limits unwanted dissipation perpendicular to direction of the flux. We find that for $\alpha_{\xi} = 1$, discontinuity-capturing is good while dissipation is small in smooth regimes. A discontinuity ‘detector’ for artificial diffusion is therefore not required.

Chow & Monaghan (1997) suggested turning off artificial dissipation when $(\rho_i \mathbf{f}_i - \rho_j \mathbf{f}_j) \cdot \hat{\mathbf{r}}_{ij} > 0$, in order to reduce unnecessary diffusion, e.g. behind a discontinuity. However in our experiments we found that such a switch makes the scheme unstable, in particular in cases where radiation beams collide in the optically thin regime. The instability results in significant non-conservation of energy. We therefore do not use the Chow & Monaghan (1997) switch, but instead apply a discontinuity detector to minimize the artificial viscosity as described in §2.6.1.

The artificial flux dissipation term of Eq. (28) causes numerical dissipation of the flux in directions perpendicular to the flux. This is problematic, in particular in the optically thin case⁹ where it leads to the destruction of a packet of radiation as shown in Fig.1. To avoid this, it requires that

⁹ In the optically thick regime, χ already provides the necessary dissipation. This is one of the reason why the flux-limited diffusion does not require artificial dissipation. Another reason is that there are no artificial oscillations when solving a diffusion equation).

⁸ This is not our default choice, see Eq. (32) below.

any artificial flux dissipation should be in the direction of the flux itself. Simply multiplying the right hand side of Eq. (28) by $\hat{\mathbf{f}} \cdot \hat{\mathbf{r}}_{ij}$ does not work: any component of numerical flux perpendicular to the actual flux, for example due to numerical noise, will still lead to the artificial destruction of an optically thin radiation packet¹⁰.

A better solution is to implement the dissipation scheme as anisotropic diffusion¹¹.

Here we outline our *default* choice of *artificial flux dissipation*. We begin by rewriting Eq. (28) in the form of an anisotropic diffusion equation,

$$\left(\frac{D\mathbf{f}}{Dt} \right) \Big|_{\text{diss}} = \frac{1}{\rho} \nabla \cdot \left[\mathbb{D}^{\mathbf{f}} \nabla \cdot (\rho \mathbf{f}) \right],$$

$$\equiv \frac{1}{\rho} \nabla \cdot \left[\rho \mathbb{D}^{\mathbf{f}} \psi \right], \quad (32)$$

where the tensor $\mathbb{D}^{\mathbf{f}}$ and the scalar ψ are given by

$$\mathbb{D}^{\mathbf{f}} = \alpha_{\mathbf{f}} v_{\text{sig}} h \hat{\mathbf{n}} \hat{\mathbf{n}}$$

$$\psi \equiv \rho^{-1} \nabla \cdot (\rho \mathbf{f}). \quad (33)$$

We implement the diffusion equation in SPH as

$$\psi_i = - \sum_j \frac{m_j}{\Omega_i \rho_i^2} (\rho_i \mathbf{f}_i - \rho_j \mathbf{f}_j) \cdot \nabla_i W_{ij}(h_i), \quad (34)$$

$$\left(\frac{D\mathbf{f}}{Dt} \right) \Big|_{i,\text{diss}} = - \sum_j \frac{m_j}{\Omega_i \rho_i^2} \left(\rho_i \psi_i \mathbb{D}_i^{\mathbf{f}} - \rho_j \psi_j \mathbb{D}_j^{\mathbf{f}} \right) \cdot \nabla_i W_{ij}(h_i). \quad (35)$$

This formulation of anisotropic viscosity in SPH is novel and we suggest that it may be applicable to other situations as well, for example when implementing magneto-hydrodynamics or cosmic ray propagation.

2.6.1 A switch for applying flux dissipation

Clearly it would be advantageous to activate flux dissipation only near discontinuities in the radiation, which requires efficient detection of such discontinuities. Such switches are also regularly used to activate dissipation in the SPH equations for hydrodynamics itself.

Morris & Monaghan (1997) proposed to use the divergence of the velocity as a measure of how discontinuous the fluid flow evolves, but this cannot distinguish compression - which conserves entropy - from true discontinuities. In addition, flux dissipation may be activated unnecessarily in the case of wave-like disturbances. Rosswog (2020b) suggested to use changes in entropy as a discontinuity detector, however it is not clear how to apply this in the case of radiation. (Cullen & Dehnen 2010) suggested to track the time derivative of the velocity divergence, $\nabla \cdot \mathbf{v}$, so that the diffusion coefficient is of the form $h^2 |\dot{\nabla} \mathbf{v}| / v_{\text{sig}}^2$, where v_{sig} is the signal velocity. This effectively corresponds to a switch that is based on the second time-derivative of the density and hence

¹⁰ It is possible to use Eq. 28 without disrupting radiation directions if the optically thin direction is imposed, as in §2.5.1. In this case, we will only consider the dissipation component (in Eq. 28) along the optically thin direction, and only consider the flux difference in that direction.

¹¹ ‘Anisotropic artificial viscosity’ was also considered by Owen 2004, but our SPH form is simpler and different from theirs.

can distinguish between gas in the pre- and post-shock regions. Such a switch is implemented in SPHENIX.

Inspired by the Cullen & Dehnen (2010) switch and after experimenting with various forms of how their expression can be applied to the case of radiation, we settled on the following target value for the diffusion coefficient,

$$\alpha_{\mathbf{f},\text{aim}} = \min \left(\max \left\{ - \frac{Ah^2}{\rho \xi \tilde{c}^2} \frac{D[\nabla \cdot (\rho \mathbf{f})]}{Dt}, 0 \right\}, 1 \right). \quad (36)$$

The denominator is $\rho \xi \tilde{c}^2$ rather than $\rho |\mathbf{f}| \tilde{c}$ because $\rho c \xi \gg |\rho \mathbf{f}|$ in the optically thick limit where artificial dissipation is not needed. $A(=200)$ is a constant multiplication factor to compensate for the large \tilde{c}^2 in the equation.

Upstream from a discontinuity, we require that the diffusion coefficient be large enough so that the discontinuity can be captured by the interpolation scheme. Downstream from the discontinuity, a smaller level of diffusion is still required to suppress any numerical oscillations. We follow Morris & Monaghan (1997) and implement this by making the diffusion coefficient time-dependent, as follows: (1) when $\alpha \leq \alpha_{\text{aim}}$, we set $\alpha = \alpha_{\text{aim}}$; (2) when $\alpha \geq \alpha_{\text{aim}}$, we evolve α back to α_{aim} by solving

$$\frac{D}{Dt} (\alpha - \alpha_{\text{aim}}) = - \frac{1}{\tau_{\text{relax}}} = - (\tilde{c}/h + \tilde{c} \chi \rho), \quad (37)$$

where τ_{relax} is the relaxation time scale. The term $\tilde{c} \chi \rho$ ensures that a large value for the α quickly relaxes back to the target value in the optically thick yet smooth regime. Finally, for gas particles in which we inject radiation we set $\alpha = 1$ to better capture any discontinuities associated with radiation injection.

Before ending this section, we comment on the required number of SPH neighbour loops associated with our RT scheme. If the radiation moment and hydrodynamics equations (Eqs. 5-9) are solved simultaneously, then at least three neighbour loops are required to compute the right-hand-side of the anisotropic diffusion equation, Eq. (32): the variable ψ in Eq. (33) requires (1) a loop to compute ρ and (2) a second loop to compute the gradient; and finally the scheme requires (3) a third loop to compute the gradient of ψ Eq. (32). Similarly, the dissipation switch of Eq. (36) requires three loops. The scheme may be optimized by solving the radiation transport equation on a shorter time-scale than used to update the hydrodynamics. During such sub-cycling, the density is kept a constant, in which case the radiation transport only requires two SPH neighbour loops. We will report on such improvements elsewhere.

2.7 Tests of the Eddington tensor closure and artificial dissipation schemes

A test of the artificial dissipation scheme and the choice of the Eddington tensor closure by propagating a single short beam of light is illustrated in Fig. 1. The underlying 48×192 particle distribution is glass-like. The figure shows four choices of the artificial dissipation and closure relation labelled *default*, *isomax*, *none*, and *original*:

- *default*: uses the *default* artificial dissipation of Eqs. 27, 31, and 32 described in §2.6.1, and the *default* modified closure M1 scheme of Eq. (19);

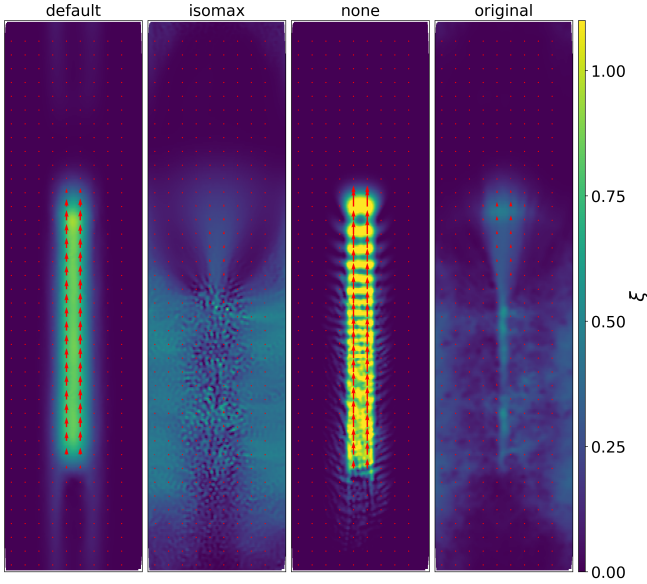


Figure 1. A packet of radiation propagating upwards (from $x = 0$ to $x = 2$) over a 2D glass-like distribution of 48×192 particles shown at time $t = 0.4$; the reduced speed of light is $\tilde{c} = 1$ and the extent of the simulation volume is $\Delta x = 2$ in the vertical direction and $\Delta y = 0.5$ in the horizontal direction. Colours represent the radiation energy density ξ and small red-arrows the radiation flux density, \mathbf{f} . Panels from left to right illustrate the *default*, *isomax*, *none* and *original* choices for the artificial dissipation and closure scheme (see text). The optical depth of the medium is zero and the packet should propagate freely at the speed of light while retaining its square form. With isotropic artificial dissipation (*isomax*) or with the *original* closure scheme, the radiation packet incorrectly dissolves quickly. The case without artificial dissipation (*none*) results in strong oscillations which leads to significant non-conservation of energy. The *default* choice correctly maintains the morphology of the beam while suppressing artificial numerical oscillations.

- *isomax*: uses isotropic artificial dissipation of Eqs. 27 and 28, setting $\alpha_{\mathbf{f}} = \alpha_{\xi} = 1$, see Eq. (29), and the *default* modified closure scheme;
- *none*: does not use any artificial dissipation (i.e. $\alpha_{\mathbf{f}} = \alpha_{\xi} = 0$ in Eq. 29) and the *default* closure scheme;
- *original*: uses the *default* artificial dissipation but the ‘*original*’ closure Eq. (17).

Figure 1 demonstrates that artificial diffusion is needed to suppress the artificial oscillations seen in panel *none*: oscillations lead to non-physical negative values of ξ , which, if zeroed, lead to a catastrophic artificial increase in radiation energy. However, such diffusion should be anisotropic to avoid that the beam artificially diffuses perpendicular to the propagation direction as seen in panel *isomax*. The *original* scheme fails to preserve the beam’s shape: it does not handle well non-uniform particle distributions. Fortunately, our *default* scheme preserves the beam shape, suppresses artificial oscillations and conserves energy.

2.8 Thermo-chemical processes

In this section we briefly describe how we implement the interaction between matter and radiation, limiting the dis-

cussion to the particular case of ionizing radiation in a pure hydrogen gas.

2.8.1 Pure Hydrogen Gas thermo-chemistry

The processes of collisional ionization and photo-ionization, photo-heating, and collisional and radiative cooling in a hydrogen gas are (e.g. Aubert & Teyssier 2008):

$$\frac{\partial n_{\gamma}}{\partial t} = \frac{\rho(\Lambda_{\xi} + S_{\xi})}{2\pi\hbar\nu} = -n_{\text{HI}}\tilde{c}\sigma_{\gamma}n_{\gamma} + n_en_{\text{HII}}(\alpha_A - \alpha_B) + S_{\gamma}, \quad (38)$$

$$\frac{\partial \mathbf{f}_{\gamma}}{\partial t} = -\chi\rho\tilde{c}\mathbf{f}_{\gamma} + \frac{\rho\mathbf{S}_{\mathbf{f}}}{2\pi\hbar\nu} = -n_{\text{HI}}\tilde{c}\sigma_{\gamma}\mathbf{f}_{\gamma} + \mathbf{S}_{\gamma}, \quad (39)$$

$$\frac{\partial n_{\text{HI}}}{\partial t} = -n_{\text{HI}}\tilde{c}\sigma_{\gamma}n_{\gamma} + n_en_{\text{HII}}\alpha_A - n_en_{\text{HI}}\beta, \quad (40)$$

$$\begin{aligned} \frac{\partial e_{\text{tot}}}{\partial t} &= \rho \frac{\partial u}{\partial t} = \rho(S_u + \Lambda_u) \\ &= \epsilon_{\gamma}n_{\text{HI}}\tilde{c}\sigma_{\gamma}n_{\gamma} - n_{\text{HI}}n_e\Gamma_{e\text{HI}} - n_{\text{HII}}n_e\Gamma_{e\text{HII}}. \end{aligned} \quad (41)$$

Eq. (38) accounts for changes in the photon density due to the sink term Λ and the source term S (see §2.3). In the second line, we specialize the sink term to photo-ionization (σ_{γ} is the photo-ionization cross-section and n_{HI} is the neutral hydrogen number density) and add recombination as a source term (α_A and α_B are the ‘case A’ and ‘case B’ recombination coefficients, respectively). The final term S_{γ} represents any other source of photons. Eq. (39) is the corresponding equation for the photon flux \mathbf{f}_{γ} , which includes a photo-ionization term and a source term.

Eq. (40) accounts for the corresponding changes in the density of neutral hydrogen, n_{HI} . The terms on the right hand side are the photo-ionization, recombination, and collisional ionization rates respectively (n_{HII} is the density of ionized hydrogen, n_e is the electron density and β is the collisional ionization coefficient).

Eq. (41) is the corresponding thermal energy equation (e_{tot} is the internal energy per unit volume and u is the internal energy per unit mass). In the second line, terms from left to right are, respectively, photo-ionization heating (ϵ_{γ} is the excess thermal energy per ionization) and gas cooling (quantified by the coefficients Γ). The values of the various constants and coefficients, together with any dependence on photon frequency, ν , and/or gas temperature, T , are summarized in Appendix A.

The above set of differential equations is in general numerically stiff, meaning that the numerical solution is unstable unless the equations are integrated in time using a very short time-step, Δt . The reason is that the coefficients in these equations are large in some situations, e.g. $n_{\text{HI}}\tilde{c}\sigma_{\gamma}n_{\gamma}$ is large in the neutral region near radiation sources. The usual remedy is to use an implicit scheme because this is stable, however its solution may not be sufficiently accurate. Our strategy described below is to combine explicit and implicit methods.

2.8.2 Solving the thermo-chemistry equations with a semi-implicit scheme combined with sub-cycling

To illustrate the solution method we make the ‘on-the-spot’ approximation by assuming that recombinations directly to

the ground state produce an ionizing photon that is absorbed close to where it was emitted (*i.e.* ‘on the spot’). In this approximation we set $\alpha_A = \alpha_B$, resulting in the following set of three coupled differential equations,

$$\frac{\partial n_\gamma}{\partial t} = -x n_H \tilde{\sigma}_\gamma n_\gamma, \quad (42)$$

$$\rho \frac{\partial u}{\partial t} = \epsilon_\gamma x n_H \tilde{\sigma}_\gamma n_\gamma - n_H^2 x(1-x) \Gamma_{eHI} - n_H^2 (1-x)^2 \Gamma_{eHII}, \quad (43)$$

$$\frac{\partial x}{\partial t} = -x \tilde{\sigma}_\gamma n_\gamma + (1-x)^2 n_H \alpha_B - x(1-x) n_H \beta, \quad (44)$$

where $x = n_{HI}/n_H$ is the neutral hydrogen fraction. Note that we denote neutral fraction as x_{HI} in the figures for clarity and as x in text for simplicity.

The partial time derivatives refer to changes due to interaction between radiation and gas only. There may be additional terms, for example, due to other photon sources or sinks, and heating and cooling due to adiabatic processes or shocks. Here, we restrict ourselves to solving these radiative equations, treating any other source/sink terms in operator split fashion.

We integrate these equations following the approach of Petkova & Springel (2009): solve the first two equations explicitly and use that solution to solve the third equation (the chemistry equation) implicitly. However, we additionally perform *sub-cycling*, requiring that n_γ and u do not change by more than 10% in each sub-cycle.

We do so by requiring that $\Delta t \leq 0.1 \min(1/(x n_H \tilde{\sigma}_\gamma), u/|\partial u/\partial t|)$. While the implicit solver for the neutral fraction x is unconditionally stable, it can be inaccurate if the time-step is too large. Therefore, we further limit the sub-cycle time-step to $\Delta t \leq C x/|\partial x/\partial t|$, where C is a parameter we choose to be 0.1 (but can be larger depending on the tolerance). So in summary, we take the sub-cycling step to be

$$\Delta t = 0.1 \min\left(\frac{n_\gamma}{|\partial n_\gamma/\partial t|}, \frac{u}{|\partial u/\partial t|}, \frac{x}{|\partial x/\partial t|}\right). \quad (45)$$

Fig. 2 illustrates the semi-implicit sub-cycle scheme.

We update n_γ using the analytic solution of Eq. (42) in case x and n_H are held constant,

$$n_\gamma(t^{n+1}) = n_\gamma(t^n) \exp(-\Delta t \sigma_\gamma c n_H x). \quad (46)$$

Doing so guarantees that n_γ is always positive, as it should be, and that the solution is asymptotically correct when recombinations are negligible. We update u using the corresponding analytical solution of Eq. (43).

The implicit solution to the chemistry equation uses the updated values for the radiation and internal energies,

$$\frac{x(t^{n+1}) - x(t^n)}{\Delta t} = -\tilde{\sigma}_\gamma n_\gamma(t^{n+1}) x(t^{n+1}) + n_H \alpha_B(t^{n+1}) [1 - x(t^{n+1})]^2 - n_H \beta(t^{n+1}) x(t^{n+1}) [1 - x(t^{n+1})]. \quad (47)$$

which is a quadratic equation for $x(t^{n+1})$.

This method can be generalised to the case of more elements by adopting the approach of Anninos et al. (1997), *i.e.* updating each element implicitly one by one in order of increasing timescale. A possible alternative scheme uses

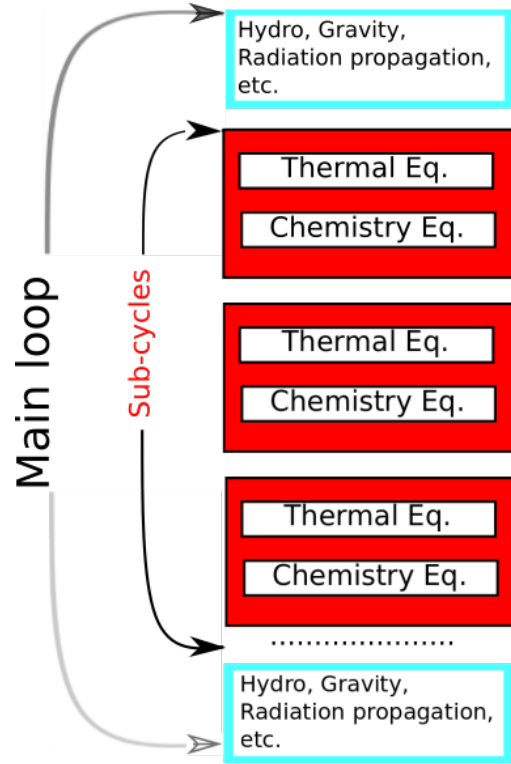


Figure 2. A schematic diagram illustrating the sub-cycling method for solving non-equilibrium thermo-chemistry equations. In the main loop, we advance the radiation, hydrodynamics, gravity, and radiation injection equations, and any other equations not related to radiation (*e.g.* sub-grid schemes). In between we sub-cycle the thermo-chemistry equations (Eqs. 42, 43 & 44), with a smaller time-step. Note that the whole set of the thermo-chemistry equations is solved sequentially within one sub-cycle, accurately accounting for any rapid changes of ionization state or photon density.

the CVODE library (Cohen et al. 1996) to solve these stiff equation, *e.g.* Kannan et al. (2019).

For now, we have restricted this discussion to the on-the-spot approximation. This limitation can be relaxed by adding recombination radiation as a source terms to each gas particle. Given that the computing time of our RT scheme is independent of the number of sources, this could be feasibly implemented in the future.

Our semi-implicit sub-cycling scheme is accurate, as we show below, as well as computationally efficient, as shown in Appendix B. Sub-cycles are initiated only when the system is out of equilibrium, for example when a source of photons is suddenly switched on. But even in such situations, we find that only a few dozen sub-cycles occur. Sub-cycling should also help with load balancing the computation. Without sub-cycling, most of the computing time will be spent in the vicinity of ionization fronts, where the thermo-chemistry is highly out of equilibrium. With sub-cycling enabled, the time-step of the main loop is instead limited by the overall CFL time-step. We proceed by showing some tests of the thermo-chemistry implementation.

2.8.3 Thermo-chemistry test I: ionizing a single gas parcel

This test is a variation of Test 0 in Iliev et al. (2006): an initially neutral parcel of pure hydrogen gas at low temperature is suddenly ionized and heated by a source of ionizing radiation with a specified spectrum of ionizing photons. After a specified time, the ionizing source is switched off. The total density of the gas parcel is kept constant. The radiation is assumed to be optically thin at all times. The test involves following the evolution of the neutral fraction, x , and of the temperature of the gas, T . To enable a fair comparison between codes, it is, of course, important to make sure that the physical constants used - such as, for example, the frequency dependence of the ionization cross section - are the same.

As the source is switched on and the hydrogen gas gets ionized, the temperature increases to a value that depends on the shape of the ionizing spectrum. The gas is then in ionization equilibrium. However, it takes longer for the gas to be in thermal equilibrium - where photo-heating balances radiative cooling. When the source is switched off, the gas starts to recombine and cool. We do not include molecule formation in the calculation, and hence the cooling rate drops with decreasing T .

• **Analytical description** The evolution can be understood by writing Eq. (44) as a Ricatti equation,

$$\frac{dx}{dt} = -\frac{x}{\tau_i} + \frac{(1-x)^2}{\tau_r} - \frac{x(1-x)}{\tau_e} \equiv \frac{1}{\tau}(x-x_1)(x-x_2), \quad (48)$$

where we defined three characteristic time-scales,

$$\tau_i \equiv \frac{1}{c\sigma_\gamma n_\gamma}; \quad \tau_e \equiv \frac{1}{n_H \beta}; \quad \tau_r \equiv \frac{1}{n_H \alpha_B}, \quad (49)$$

and

$$\frac{1}{\tau} = \frac{1}{\tau_e} + \frac{1}{\tau_r}; \quad x_1 + x_2 = 2 + \frac{\tau_r}{\tau_i}; \quad x_1 x_2 = \frac{\tau}{\tau_r}. \quad (50)$$

Choosing initial condition $x = x_0$ at $t = 0$, the general solution in case all τ 's are constant, is

$$x(t) = \frac{x_2(x_0 - x_1) - x_1(x_0 - x_2)f(t)}{(x_0 - x_1) - (x_0 - x_2)f(t)} \\ f(t) = \exp[-(x_1 - x_2)t/\tau]. \quad (51)$$

In the special case where collisional ionizations are neglected, $\tau_e \rightarrow \infty$ and when $\tau_i \ll \tau_r$, this solution simplifies to approximately $x(t) = x_0 \exp(-t/\tau_i) + \tau_i/\tau_r$: the neutral fraction approaches its *ionization equilibrium* exponentially on the ionization timescale, τ_i .

This approximate description assumes that τ_r - and hence the temperature of the gas - remains a constant. An estimate of the change in temperature following rapid ionization, $\tau_i \ll \tau_r$, follows from neglecting radiative cooling in the short time it takes to ionize the gas, so that

$$\rho \frac{du}{dt} \approx -\epsilon_\gamma \frac{dn_{\text{HI}}}{dt} = -\epsilon_\gamma n_H \frac{dx}{dt}, \quad (52)$$

where ϵ_γ is the mean energy injected into the gas per photo-ionization, see §A. Writing the thermal energy per unit mass, u , in terms of the neutral fraction, x , as $u = k_B T / (\mu m_H)$ with $\mu = (2-x)^{-1}$, yields the following relation between the initial temperature $T = T_0$ at $t = 0$, and the temperature T

when the neutral fraction is x :

$$k_B T = \frac{2-x_0}{2-x} k_B T_0 + \frac{2\epsilon_\gamma}{3} \frac{x_0 - x}{2-x}. \quad (53)$$

In the test described below, the gas is initially neutral, $x_0 = 1$, and at low temperature, $k_B T_0 \ll \epsilon_\gamma$, and the photo-ionization rate is high so that in photo-ionization equilibrium, $x \ll 1$. In this case, the photo-ionization equilibrium temperature is $T_1 \approx \epsilon_\gamma / (3k_B)$, which depends only on the ionization energy per photon, regardless of radiation intensity or gas density.

On a longer timescale, the parcel of gas will reach thermal equilibrium (temperature T_2), where photo-heating balances radiative cooling. Provided $T_2 > T_1$, the timescale to reach this equilibrium can be estimated by simply neglecting cooling and noting that the rate at which the gas is heated is approximately the product of the ionization rate, x/τ_i , times the energy injected per photo-ionization per hydrogen atom, ϵ_γ/m_H , hence

$$\frac{du}{dt} = \frac{\epsilon_\gamma}{m_H} \frac{x}{\tau_i} \approx \frac{\epsilon_\gamma}{m_H \tau_r}. \quad (54)$$

Therefore it takes approximately a recombination time to reach thermal equilibrium (see also Pawlik & Schaye 2011).

When the source is suddenly switched off, gas will start to recombine. This is still described by a Ricatti equation of the form of Eq. (51), except that now

$$x(t) = \frac{x_2(x_{\text{eq}} - x_1) - x_1(x_{\text{eq}} - x_2)f(t)}{(x_{\text{eq}} - x_1) - (x_{\text{eq}} - x_2)f(t)} \\ f(t) = \exp[-(x_1 - x_2)(t - t_{\text{eq}})/\tau], \quad (55)$$

where x_{eq} is the neutral fraction in thermal equilibrium, t_{eq} is the time that the ionizing source is switched off, and $x_1 + 1/x_1 = 1 + \tau/\tau_r$ with $x_2 = 1/x_1$. If the gas is no longer heated, it will of course simply keep on cooling and there is no further equilibrium state.

• **Numerical solution** For the numerical values for this test, we take¹² $\tilde{c} = c$, $n_H = 1 \text{ cm}^{-3}$, $x_0 = 1$ and $T_0 = 100 \text{ K}$. From time $t = 0$, the parcel of gas is being irradiated with a black body spectrum of temperature $T = 10^5 \text{ K}$ (for which $\epsilon_\gamma = 6.33 \text{ eV}$ in the optically thin limit) and photon flux $F_{\text{photon}} = 10^{12} \text{ photons s}^{-1} \text{ cm}^{-2}$. The source is switched off after a time $t_s = 5 \times 10^7 \text{ yr}$ and we follow the evolution until time $t_e = 10^8 \text{ yr}$.

For a reference temperature of $T = 10^4 \text{ K}$, the three timescales are $\tau_i \approx 10^{-2.3} \text{ yr}$, $\tau_r \approx 10^{5.1} \text{ yr}$ and $\tau_e \approx 10^{9.3} \text{ yr}$, so that $\tau_i \ll \tau_r \approx \tau \ll t_e < \tau_e$. The temperature in photo-ionization equilibrium is $T = 6.33 \text{ eV} / (3k_B) \approx 10^{4.39} \text{ K}$, and the temperature in thermal equilibrium is about twice that. The timescale for the gas to reach thermal equilibrium can be estimated as follows. The heating rate of the gas, when in photo-ionization equilibrium, is $du/dt \approx \epsilon_\gamma/\tau_r \approx 8.3 \times 10^{-11} \text{ erg Myr}^{-1}$. Therefore the timescale to reach thermal equilibrium is approximately

$$t_{\text{eq}} \approx \frac{\Delta u}{du/dt} = \frac{u_{\text{eq}} - u_i}{du/dt} \approx \frac{u_i}{du/dt} \approx 10^{5.1} \text{ yr}, \quad (56)$$

where we have used the fact that for the parameters of this

¹² Note that the value of \tilde{c} is irrelevant to the solution since the pure thermo-chemistry equation is independent of \tilde{c} if F_{photon} is given.

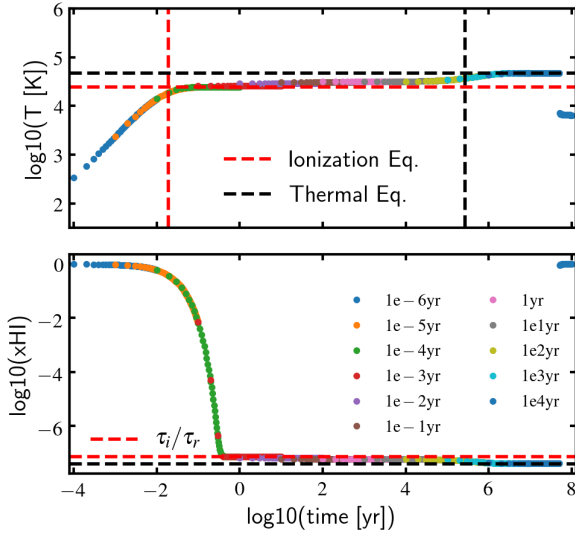


Figure 3. A variation of Iliev et al. (2006) Test 0: photo-heating of a single gas parcel irradiated with black body radiation of temperature $T = 10^5$ K. The source is switched off after time $t_s = 5 \times 10^7$ yr. Vertical dashed lines indicate the ionization timescale τ_i (red) and the time to reach thermal equilibrium, t_{eq} (black), horizontal dashed lines indicate the expected photo-ionization equilibrium temperature (or neutral fraction) (red) and the thermal equilibrium temperature (black). Points with different colours show the evolution computed with different, fixed, global time-steps, as per the legend. Simulations with different Δt step sizes yield the same evolution, which also matches the analytical estimate as well as the curves in Iliev et al. (2006) and Pawlik & Schaye (2011) (not shown here).

test, $u_{eq} \approx 2u_i$. In summary: the gas should reach its photo-ionization equilibrium temperature by a time τ_i , reach its thermal equilibrium temperature by the time t_{eq} , and start to cool and recombine after time t_s .

We want to verify that the combination of explicit sub-cycling and implicitly solving the chemistry equations yields the correct solution, independently of a globally imposed time-step. To demonstrate the accuracy of the integration scheme, we also want to compare to a run in which we integrate the equations with a short, fixed time-step. However, the ionization timescale τ_i is much smaller than the evolution timescale t_e , and it is impractical to simulate the whole time evolution with a time-step much shorter than τ_i . Here we follow Pawlik & Schaye (2011) and perform a dozen simulations with different (fixed) time-steps, from $\Delta t \ll \tau_i$ to $\Delta t \gg \tau_i$.

Results are shown in Fig. 3, where differently coloured curves show the evolution for different values of the global time-step, Δt . All curves follow the analytical expectation: gas heats and gets almost fully ionized on a timescale τ_i (vertical dashed red line), reaching its photo-ionization equilibrium temperature (horizontal dashed line), continues to be heated on a timescale τ_r (vertical dashed black line) to reach thermal equilibrium (horizontal dashed black line), and finally starts to recombine and cool when the source is switched off. All simulation runs fall on top of each other,

demonstrating that the numerical solution is independent of the global fixed value of Δt .

After the radiation is switched off, gas recombines and cools rapidly to $T \sim 10^4$ K, below which the cooling rate drops rapidly as we only include cooling by neutral hydrogen.

There are two major takeaways from Fig. 3. Firstly, the simulated evolution follows the analytical expectation as well as the results from other simulation codes in Iliev et al. (2006) (see their Fig. 5), therefore the scheme is accurate. Secondly, the evolution is independent of the global time-step, demonstrating the convergence of the sub-cycle thermo-chemistry solver. With this solver, the (main) time-step of the simulation is only limited by the Courant condition in solving the moment equation (§2.3).

2.9 Radiation injection

In our implementation, radiation is injected by ‘star particles’ which, in our SPH implementation, have a smoothing length h , which is calculated in the same way as that of gas particles (*i.e.* by requiring that each star particle interacts with the desired number of kernel-weighted gas neighbours).

A star particle i with time-step Δt_i and energy injection rate $\dot{e}_{i,rad}$ distributes a total amount of radiation $\dot{e}_{i,rad}\Delta t_i$ into all of its neighbouring gas particles. Each individual neighbouring gas particle j receives an amount of energy equal to

$$\Delta e_{ij} = m_j \Delta \xi_j = \frac{m_j}{N_{nor} \rho_j r_{ij}^2} \dot{e}_{i,rad} \Delta t_i. \quad (57)$$

This kernel-weighted energy transfer is normalized by N_{nor} , computed such that $\sum_j \Delta e_{ij} = \dot{e}_{i,rad} \Delta t_i$, where the sum is performed over all of i ’s gas neighbours j .

We inject the corresponding isotropic radiation flux, $m_j \Delta \mathbf{f}_j$, as if the surrounding medium were optically thin:

$$\Delta \mathbf{f}_j = \tilde{c} \mathbf{r}_{ji} \Delta \xi_j. \quad (58)$$

Because the distribution of gas neighbours around any star particle is generally relatively disordered, the resulting radiation field may not be very isotropic unless energy is injected over a sufficiently large number of gas particles. To avoid that the source of photons is unacceptably anisotropic, we increase the smoothing lengths of star particles to be a few times the smoothing length of gas particles, *e.g.* $h_{star} = 2h_{gas}$ (see Fig. 7).

An alternative way of ensuring isotropic radiation around sources is to impose the radiation direction in the optically thin limit (§2.5.1). In some tests, *e.g.* tests of Ström-gren spheres, we calculate the total radiation energy within the injection region, and then reset the radiation distribution according to the optically thin expectation¹³.

¹³ It is possible to inject radiation energy only - without updating the radiation flux - provided we apply the original M1 closure (Eq.17), since the moment equations will generate an isotropic radiation field in the absence of initial flux. But this is not possible with the modified M1 closure in the optically thin environment for which the (initial) direction of the Eddington tensor needs specifying.

2.10 Implementation details

Our RT scheme is implemented in the public version of the SWIFT (SPH with interdependent fine-grained tasking) code (Schaller et al. 2016)¹⁴, which has been applied in galaxy formation and planetary giant impact simulations (Kegerreis et al. 2019). The target application of SWIFT are zoomed cosmological simulations and simulations in representative volumes, with subgrid physics modules similar to EAGLE (Schaye et al. 2015).

SWIFT is an SPH code that solves cosmological or non-cosmological hydrodynamic equations, including self-gravity, and is designed to work on hybrid shared/distributed memory computer architectures. Load balance is optimised using task-based parallelism, with tasks assigned by a graph-based domain decomposition, and using dynamic, asynchronous communication. For hydrodynamics, Borrow et al. (2018) found SWIFT to have good weak scaling from 1 to 4096 codes (losing only 25% performance) in low redshift cosmological galaxy simulations (with EAGLE physics from Schaye et al. 2015).

The time-stepping of the RT scheme follows the Hernquist & Katz (1989) factor-of-two time-step hierarchy implemented in SWIFT: a particle with time-step Δt is assigned to the time-step bin N such that $2^N \leq \Delta t/t_{\min} < 2^{N+1}$, where t_{\min} is some small minimum time-step. At each step in time, the radiation field in particles in all bins N with $N \leq M$ are updated with a forward Euler method, where $2^M t_{\min}$ is the time-step of the active particles with the largest time step (see Borrow et al. 2018 for the time-stepping strategy in SWIFT in the absence of RT).

When hydrodynamics and other processes are included, the time-step of each individual particle is the minimum time-step required by all these processes combined, although typically the radiation time-step ($\Delta t_{\text{rad}} \sim 0.1h/\tilde{c}$) is the most limiting. We do not (yet) sub-cycle the radiative transport step, therefore all processes (including gravity and hydrodynamics) are integrated using the smallest time-step. This is an avenue for future optimization. However, we *do* sub-cycle the thermo-chemistry differential equations, as described in §2.8. This leads to significant saving in computation time, since the time-step associated with these chemistry equations can be orders of magnitude shorter than the RT time step.

2.11 The Reduced Speed of Light approximation

When radiation travels at the speed of light, the time-step to advance a radiation front correctly is of order $\Delta t_c \sim h/c$, for a smoothing length h of an SPH particle. This is, of course, much shorter than the CFL step, which is of order $\Delta t_s \sim h/v_s$, where v_s is the sound speed. However, ionising radiation with flux F moves at the speed of the ionization front, $v_I \sim F/(2\pi n_H h\nu)$, through neutral gas with density n_H . When $v_I \ll c$, the code can be sped up by a large factor by reducing the speed of light, from c to \tilde{c} . As long as $\tilde{c} > v_I$, the speed of an ionization front can still be correct for a given F (see e.g. the discussion in Rosdahl et al. 2013).

This ‘reduced speed of light’ (RSL) approximation was

introduced by Gnedin & Abel (2001) to simulate radiative transfer efficiently and has been applied to other radiative transfer simulations, e.g. by Aubert & Teyssier (2008). They demonstrate that RSL performs well in problems involving ionization, photo-heating, and expansion of HII regions.

However, there is no unique way to implement RSL. Skinner & Ostriker (2013) implemented the RSL approximation in simulating RT in the interstellar medium, e.g. modeling radiation reprocessed by dust. However, their approach does not conserve total radiation plus matter energy and momentum, and the non-equilibrium solution might not be correct.

Ocvirk et al. (2019) examined the ‘dual speed of light’ (DSL) approximation, where $c \rightarrow \tilde{c}$ in the propagation equation but not in the thermo-chemistry equations. Unfortunately, DSL fails to reproduce the correct equilibrium gas properties. This is because when c is reduced to \tilde{c} in the propagation equation, the photon-matter interaction rate does not change accordingly in DSL. This can be seen by considering the analytical solution of the Strömgren sphere (Appendix C),

$$n_{\text{HI}} c \sigma_{\gamma} n_{\gamma} = \left(\frac{c}{\tilde{c}}\right) \frac{n_{\text{HI}} \sigma_{\gamma} \dot{N}_{\gamma}}{4\pi r^2} \exp\left(-\int_0^r n_{\text{HI}} \sigma_{\gamma} dr\right) \\ = n_e n_{\text{HI}} \alpha_B, \quad (59)$$

where the factor \tilde{c} arises from the propagation equation in the optically thin limit, and the factor c comes from the thermo-chemistry equation. The equilibrium neutral fraction will deviate from the correct solution due to the c/\tilde{c} factor.

Thus, our *default* treatment is to replace $c \rightarrow \tilde{c}$ in all equations (Aubert & Teyssier 2008; Rosdahl et al. 2013), including the propagation and thermo-chemistry equations. For a fixed photon flux, F , (or photon injection rate), this choice reduces the interaction strength between light and matter (e.g. $\sigma_{\gamma} \tilde{c}$) to compensate for higher photon density (due to the slower photon propagation speed). As a result, the photo-ionization rate will be independent of \tilde{c} (as long as \tilde{c} is larger than other speeds). Furthermore, the choice of \tilde{c} will *not* affect the equilibrium gas properties, as demonstrated in Eq. 59 (and see the tests in next sections).

However, there are limitations to RSL. First, \tilde{c} should exceed the speed v_I of any ionization front. For example, Bauer et al. (2015) showed that using $\tilde{c} = c/10$ affects the timing of reionization. Another issue of RSL is that using $\tilde{c} < c$ increases the momentum term $\nabla(\mathbb{F}E)$, and if this is not corrected for then the radiation pressure will be too large (see also Jiang et al. 2012; Jiang & Oh 2018). This may be problematic in cases where radiation pressure is crucial, for example when modelling radiation pressure from AGN. In the case of reionization simulations, the photon-density is low and radiation pressure is mostly neglected anyway.

3 VALIDATION

This section contains an extensive series of tests to validate the numerical scheme and its implementation in the SWIFT code. The tests combine the *default* scheme for radiation (§2.7) with the SPHENIX SPH formulation for hydrodynamics (§2.5), unless explicitly stated otherwise. Some test

¹⁴ <http://swift.dur.ac.uk/>

impose the optically thin direction in the Eddington tensor (§2.5.1). Otherwise, the flux propagates in the direction $\hat{\mathbf{n}} = \hat{\mathbf{f}}$, as computed for each gas particle. In all except the shadowing test (§3.2), we apply periodic boundary conditions. We will make the on-the-spot approximation in all of the tests (§2.8.2). We do not use the reduced speed of light (RSL) approximation in §3.1 in which we aim to compute the radiation distribution, but we *do* use the RSL approximation in §3.2-3.4, which focuses on properties of the gas (see §2.11).

3.1 Optically Thin Propagation tests

3.1.1 Propagation in one dimension

The setup propagates a finite radiation packet in an optically thin medium. We test whether the radiation front travels at the correct speed, $c = 1$, without excessive smoothing of the front and without generating artificial oscillations in the radiation density, $E(x)$, behind the radiation packet. Initially, the radiation energy density and flux are uniform and non-zero only for $x < 0$, with the radiation flux is pointing in the $+x$ direction initially. Fig. 4 shows the initial condition and the configuration at $t = 5$, when the radiation front has propagated 100 times the mean inter-particle spacing. While there is small broadening of the radiation front caused by the artificial dissipation, numerical oscillations are suppressed significantly and the scheme is stable. The front propagates at the correct speed ($c = 1$) and the radiation energy density E remains constant inside the radiation package, unaffected by the artificial dissipation. The lower panel demonstrates the excellent energy conservation of our scheme in this test problem.

3.1.2 Propagation in two dimensions

We repeat the previous test but now in two-dimensions: a rectangular radiation package propagates in empty space in 2D. The constant-mass SPH particle distribution is glass-like, with 256×1024 particles filling the computational volume of horizontal extent $\Delta x = 0.5$ and vertical extent $\Delta y = 2.0$.

This tests the extent to which radiation leaks out of the package artificially, either perpendicular or parallel to the propagation direction, as a consequence of the artificial dissipation. The propagation direction of the radiation on individual particles is not imposed, but computed from $\hat{\mathbf{n}} = \hat{\mathbf{f}}$. Results are shown in Fig. 5 where the radiation package moves upwards from the initial state at time $t = 0$ (left panel) to time $t = 0.5$ (right panel).

The top panel of the figure demonstrates the ability of the implementation to maintain the direction of the radiation, with little artificial leakage of radiation perpendicular to the beam. At $t = 1$, the packet has propagated upwards over 256 mean particle spacings. Two small ‘tails’ of radiation trail the package, where radiation leaked out of the beam.

In the rightmost panel, labelled ‘var. ρ ’, we test the radiation propagation in the presence of a particle density gradient. Constant-mass SPH particles are distributed ac-

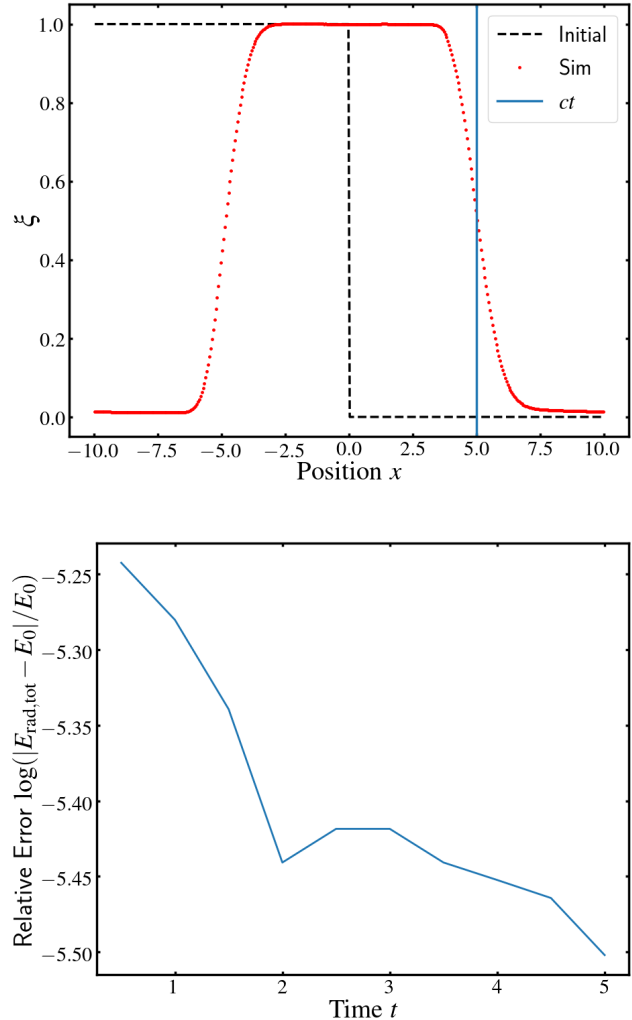


Figure 4. Propagation in 1D: *Upper panel:* radiation energy density, $\xi(x)$ of a package of radiation propagating to the right at the speed of light ($c = 1$ in these units). The *black dashed line* is the initial profile in units of the initial value of E , the *blue line* is the edge of the initial profile shifted to the right by $\Delta x = 5$, the *red points* are the simulated values of E for individual SPH particles at time $t = 50$. The simulation uses 400 SPH particles located on the vertices of a regular grid. The test shows that the front moves at the correct speed. *Lower panel:* the relative error in total radiation energy as a function of time, where E_0 and $E_{\text{rad,tot}}$ are the total radiation energy at the beginning and at time t , respectively. The deviation from energy conservation is less than 0.01% at all times.

cording to a cored power-law density profile $\rho(y)$:

$$\rho(y) = \begin{cases} \rho_c, & 0.5 < y < 1.5 \\ \rho_c [0.5/(y-1)]^2, & \text{elsewhere.} \end{cases} \quad (60)$$

Here, y is the direction of propagation of the radiation. The particle density inside the core ρ_c is the same as that in the uniform density test. The radiation distribution is similar to the uniform density case, except that the beam broadens slightly once it enters the low density region at the top of the panel, where the spatial resolution is lower. The total radiation energy increases by $\sim 1\%$ at $t=1$, mainly because of the numerical oscillations at the beam front. Because we

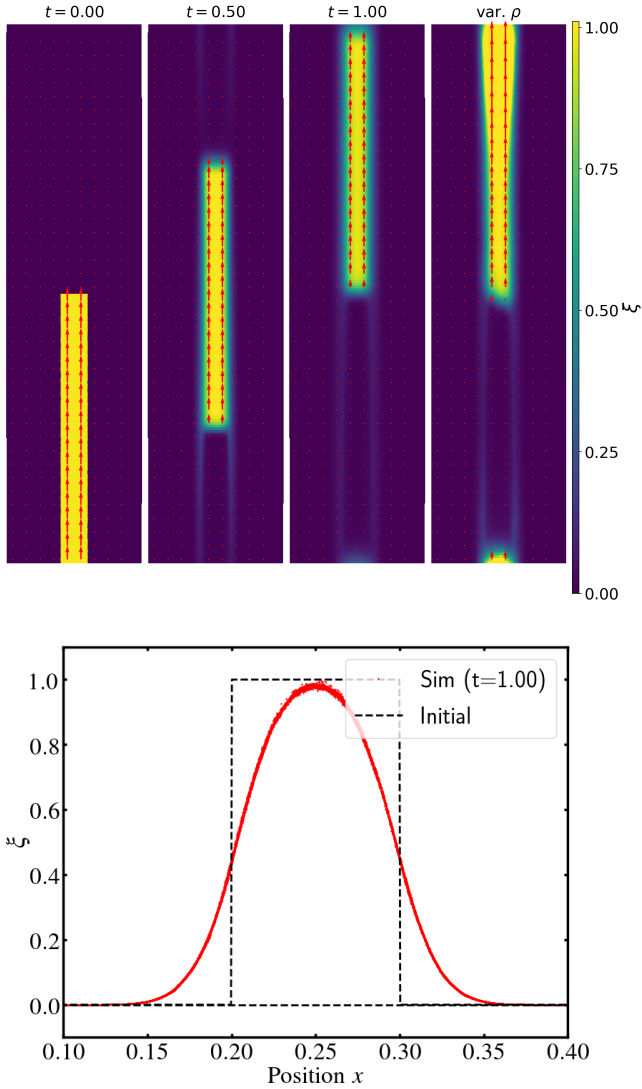


Figure 5. Propagation in 2D: propagation of a packet of radiation in two dimension at the speed of light, $c = 1$. *Upper panels:* Radiation energy density of the packet in units of its initial value. The *left panel* shows the initial state, where the packet has length $\delta y = 1$. The central panels show the system at different times at a constant particle density. The rightmost panel labelled ‘var. ρ ’ shows the radiation beam in case of an underlying density gradient (see main text) at $t=1$. Colors represent the radiation energy density and *red arrows* show the radiation fluxes. *Lower panel:* radiation energy density, $\xi(x, y)$, of SPH particles with $1.4 \leq y \leq 1.6$ at time $t = 1.00$ (*red line*), the *dashed-black line* is the initial shape of the packet.

enforce that radiation energy density remains positive everywhere, clipping negative radiation densities increase the total radiation energy.

Smoothing perpendicular to the beam is quantified in more in detail in the lower panel, which is a cut through the middle of the beam at time $t = 1$. This profile has approximately Gaussian-shaped edges, as expected from artificial diffusion (§2.6); the diffusion coefficient is proportional to hc . The dependence on the smoothing length, h , means that the beam can propagate further without distortion at higher resolution. Due to the finite resolution and, in general, non-

uniform underlying SPH particle distribution, it is not possible to completely eliminate radiation leakage perpendicular to the propagation direction without causing instabilities; higher-order shock-capturing schemes (e.g. Liu et al. 1994) might suppress such artificial leakage more efficiently.

The next test is that of radiation propagating isotropically away from a source in two dimensions, see Fig. 6. The figure confirms that the radiation front preserves rotational symmetry as it propagates out at the speed of light. The radiation energy density is smooth in the radial shell, with no appreciable noise even though the underlying particle distribution is non-uniform. The energy density is small behind the shell. The absence of significant artificial ‘left over’ radiation results from the artificial dissipation switch.

3.2 Radiation tests without hydrodynamics: constant temperature

3.2.1 Static Stromgren Sphere with Constant temperature

The first test is Test 1 in Iliev et al. (2006). This tests the radiative transfer scheme and the thermo-chemistry solver against an analytical solution: uniform density, neutral gas is photoionized by a source that emits ionizing photons at a constant rate. We keep the density and temperature of the gas constant, *i.e.* the gas is not allowed to move, heat or cool. The ionization front propagates into the gas cloud until it reaches its Strömgen radius. The analytical solution (assuming grey opacity) is derived and summarised in Appendix C.

The numerical parameters are taken to be identical to those used by Iliev et al. (2006) to allow for a direct comparison: the gas cloud consists of pure hydrogen gas with density $n_{\text{H}} = 10^{-3} \text{ cm}^{-3}$, the collisional ionization coefficient $\beta = 3.1 \times 10^{-16} \text{ cm}^3 \text{ s}^{-1}$ and the recombination coefficient is $\alpha_{\text{B}} = 2.59 \times 10^{-13} \text{ cm}^3 \text{ s}^{-1}$ (with the on-the-spot approximation); the photoionization cross section is $\sigma_{\gamma \text{HI}} = 8.13 \times 10^{-18} \text{ cm}^2$. The source emits ionizing radiation at a constant rate of $\dot{N}_{\gamma} = 5 \times 10^{48} \text{ photons s}^{-1}$. The computational volume has linear extent of 20 kpc; the SPH particle distribution is glass-like with approximately 32^3 particles. In this problem we also test the RSL approximation, using $\tilde{c} = c/10$.

We first compare several implementations of the injection of radiation energy by the source (§2.9) and of the optically thin closure relation (§2.5.1); results are shown in Fig. 7. Without requiring that the optically thin direction be radial, the ionization front is not spherical when radiation is injected over one smoothing length (left panel), a consequence of the fact that the SPH particles are not exactly uniformly distributed around the source. This can be remedied by either injecting radiation into gas particles up to two smoothing lengths away from the source (middle panel) or by requiring that the radiation should move radially away from the source, *i.e.* $\hat{\mathbf{n}} = \hat{\mathbf{r}}$ (right panel).

For the actual test, we inject radiation in all gas particles within two smoothing lengths from the source but without imposing a propagation direction, as in the middle panel of Fig. 7. The simulation results at time $t = 500 \text{ Myr}$ are compared to the analytical solution derived in Appendix C in Fig. 8. By this time, the system is in a steady-state where ionizations balance recombinations and the ionization front

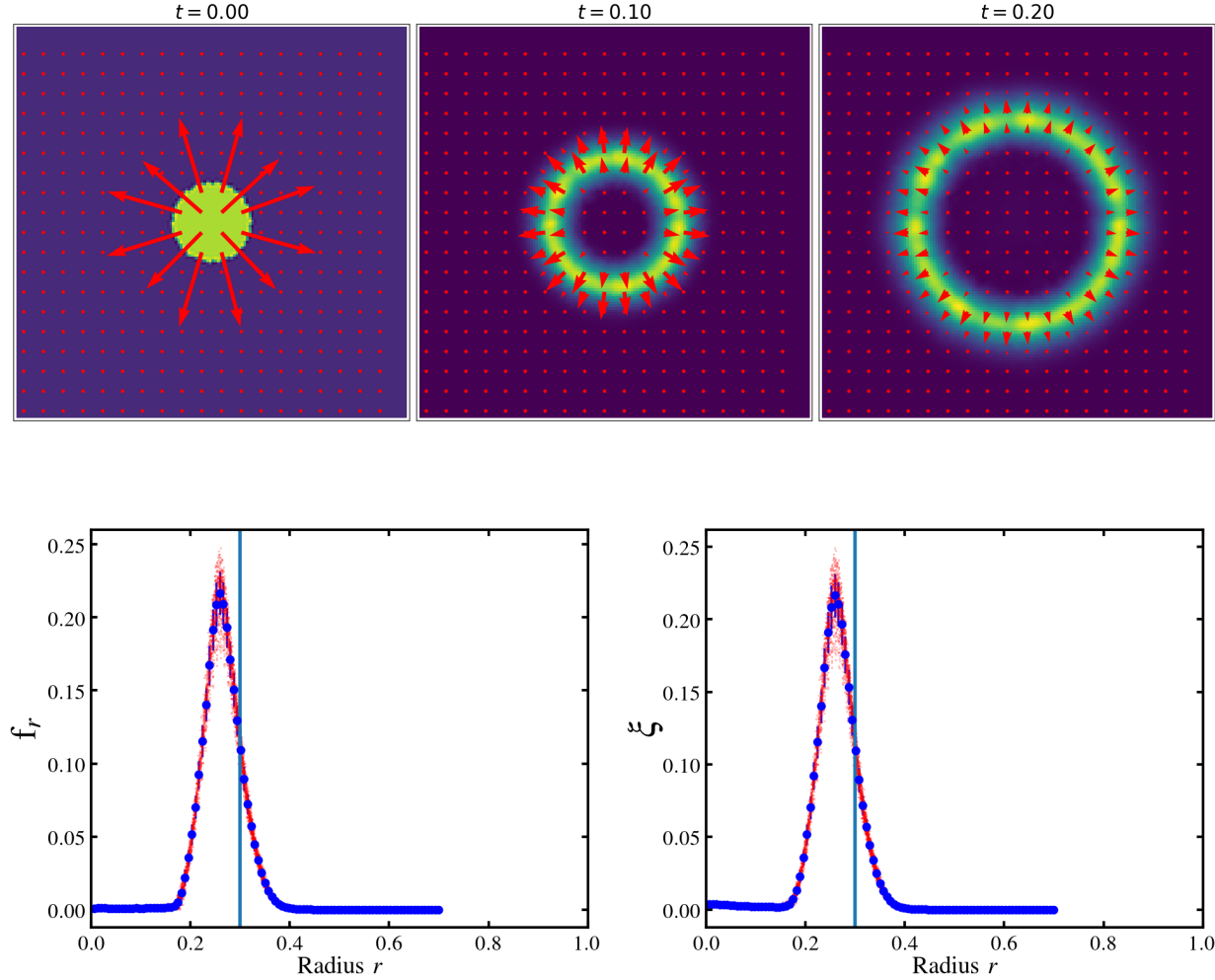


Figure 6. Propagation in 2D: propagation of a shell of light away from a source at the speed of light, $c = 1$. *Upper panel:* radiation energy density of the shell of light in units of its initial value. The *left panel* shows the initial state, where radiation is filled uniformly within a circle with radius $r = 0.1$ and points out radially. Panels to the right show the system at times $t = 0.1$ and $t = 0.2$. The SPH particle distribution is glass-like, with 128×128 particles filling the computational volume of horizontal extent $\Delta x = 2$ and vertical extent $\Delta y = 2$. Colours represent the radiation energy density and *red arrows* show the radiation fluxes; the colour scale is not the same in each panel to bring out the smoothness of the radiation density as the shell moves out. *Lower panel:* radiation flux (*left panel*) and radiation density (*right panel*) as a function of radius at time $t = 0.2$. The *red points* represent values of all individual SPH particles, *blue points* show binned values. The *blue vertical lines* at $r = 0.3$ show the location of the radiation front at time $t = 0.2$.

is at the location of the Strömgren radius. We can compare the neutral fraction in the simulation to the exact analytical solution.

The mean value of the neutral fraction as a function of radius, $x(r) = n_{\text{HI}}(r)/n_{\text{H}}$, follows the analytical result closely with relatively small scatter. There are small systematic deviations from the analytical solution near $r = 0$, where radiation is injected, and at $r \geq 6$, where the analytical value of neutral fraction drops faster than the simulated value. The latter is due to radiation ‘leaking’ beyond the Strömgren radius in the simulation due to the artificial dissipation. The overall performance of the scheme is relative good: (1) the neutral fraction is approximately spherically symmetric; (2) the scheme is photon-conserving and therefore the location of the Strömgren radius agrees well with

the analytical solution; (3) the scheme is accurate both in the optically thin region near the source as well as in the optically thick region outside the Strömgren radius, as well as in the intermediate region. We note that some cone-based (e.g. Pawlik & Schaye 2008) or short-characteristic (e.g. Finlator et al. 2009) RT schemes could produce artificial ‘ray-like’ features in the neutral fraction, depending on angular resolution; no such features appear in the present scheme¹⁵.

The effect of using the RSL approximation on the time

¹⁵ Deviations from spherical symmetry near the Strömgren radius are apparent in Fig. 7 due to low spatial resolution and irregular particle distribution, but these are significantly less severe than the “ray effect” in the cone-based or short-characteristic methods.

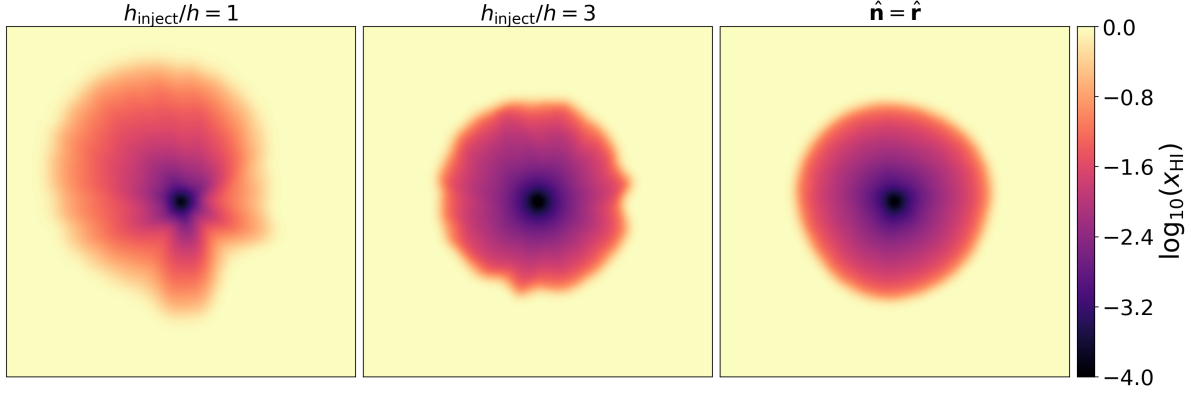


Figure 7. Isothermal Strömgren sphere from Iliev et al. (2006) Test 1: a source of radiation, located at the centre of the panels, photoionizes hydrogen gas, kept at constant density and constant temperature. Panels show the neutral fraction, $n_{\text{HI}}/n_{\text{H}}$, at time $t = 500$ Myr in a slice through the centre of the three-dimensional volume. *Left panel:* radiation is injected in all gas particles within one smoothing length from the source, see §2.9 for the method of injection. *Central panel:* radiation is injected in all gas particles within two smoothing lengths from the source. *Right panel:* as in left panel, but the direction in which radiation travels is set to $\hat{\mathbf{n}} = \hat{\mathbf{r}}$, see §2.5.1 for details. The ionization front becomes more spherical if the injection region is enlarged, or if the radiation is forced to propagate radially.

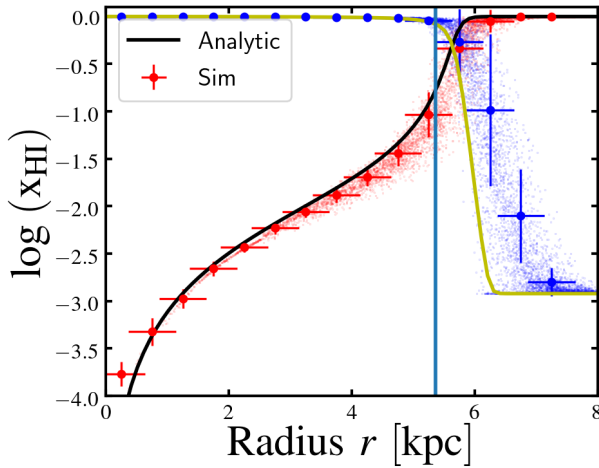


Figure 8. Isothermal Strömgren sphere from Iliev et al. (2006) Test 1: a source of radiation, located at radius $r = 0$, photoionizes hydrogen gas, kept at constant density and constant temperature. The system is shown a time $t = 500$ Myrs after the source is switched on. *Red points* are the neutral hydrogen fraction, $x_{\text{HI}} = n_{\text{HI}}/n_{\text{H}}$, of individual gas particles, with the *thick blue points* showing binned values, with horizontal error bars indicating the bin width, and vertical error bars the standard deviation; the *black line* is the analytical solution derived in Appendix C. *Small blue points*, and *thick black points* with black error bars show the corresponding ionized fraction, $1 - x_{\text{HI}}$, with the *yellow line* the analytical solution. The *vertical blue line* is the approximate analytic location of the Strömgren radius from the balance between injection and recombination (Eq. C5). The mean interparticle separation of the SPH particles is 0.625 kpc. Here we inject radiation over two smoothing lengths.

evolution of the I-front is illustrated in Fig. 9. We use a similar setup as above, but to capture the early phase of the expansion of the ionization front (1) we inject radiation over only one smoothing length but impose that the radiation

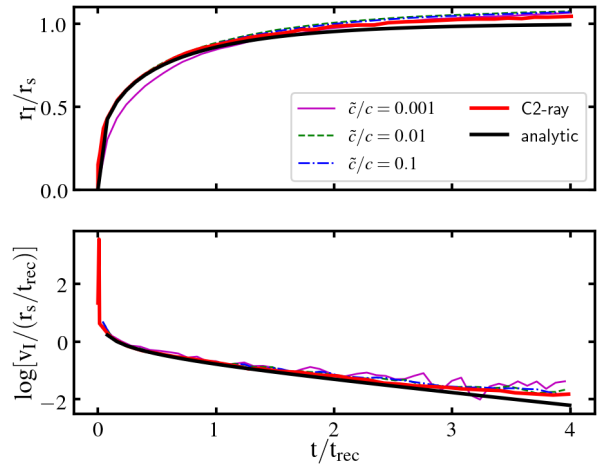


Figure 9. Test 1 (Iliev et al. 2006): pure hydrogen isothermal HII region expansion from time $t = 0$ to 500 Myr. *Top:* the evolution of the radius of the ionization front, defined by where 50% hydrogen in the spherical shell is ionized, divided by the Strömgren radius (Eq. C6). *Bottom:* the evolution of the velocity of the ionization front, divided by the Strömgren radius over the recombination time $t_{\text{rec}} = (n_{\text{H}}\alpha_B)^{-1}$. The c/\tilde{c} lines represent our simulation results with different reduced speeds of light and the fixed optically thin direction (§2.5.1). The black lines show the analytic solutions (Eq. C5 and its derivative; note that the analytic solution is only approximately correct). Finally, the ‘C2-ray’ lines represent the C2-ray (Mellema et al. 2006) result in Iliev et al. (2006).

propagates radially outwards, *i.e.* $\hat{\mathbf{n}} = \hat{\mathbf{r}}$; (2) we use higher resolution, 64^3 particles.

The traditional analytical solution for the time-dependent location of the ionization front, $r_I(t)$, of Eq. (C5) assumes that the front is infinitely thin and that the downstream gas is fully ionized. In reality, the downstream gas

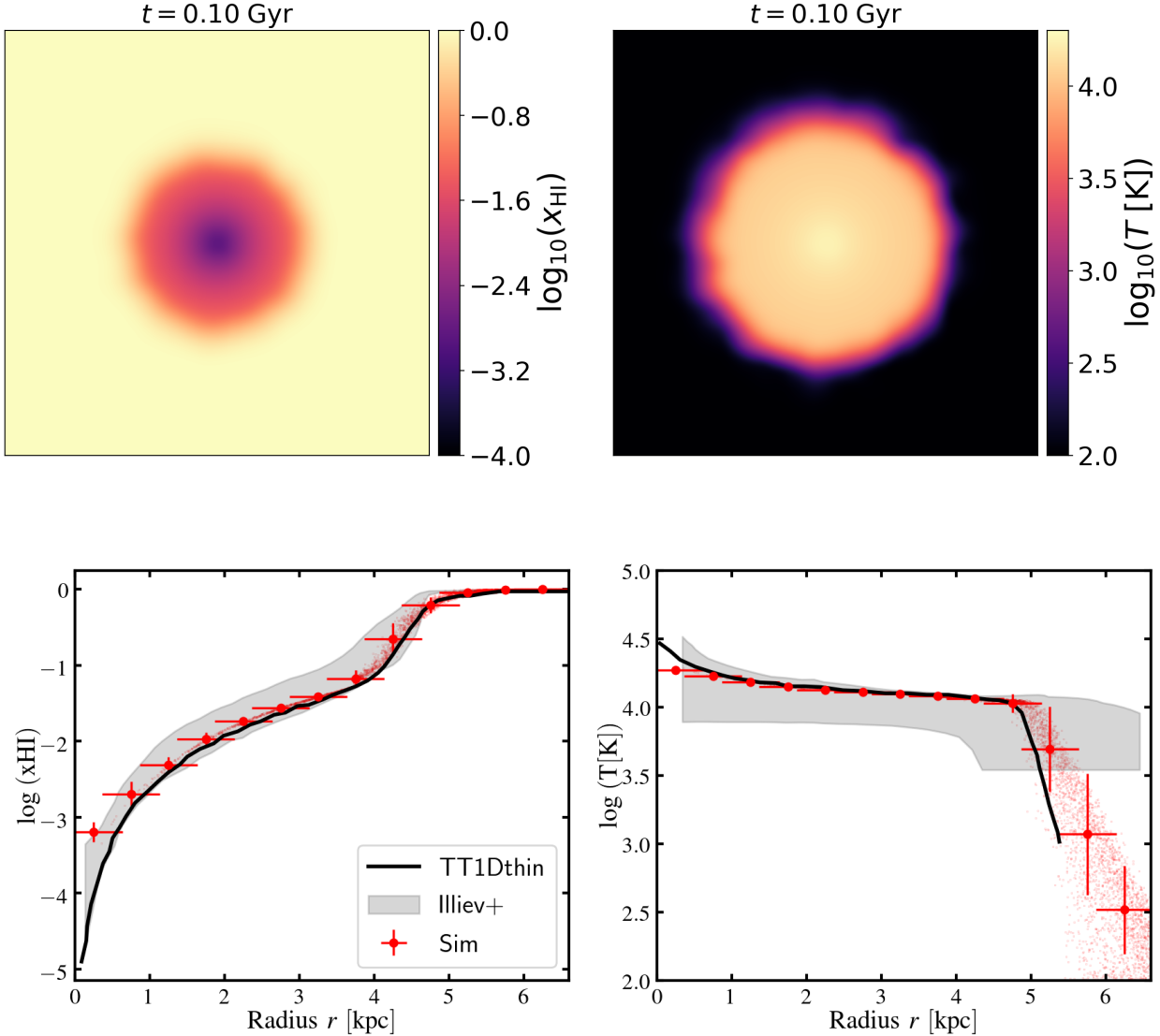


Figure 10. Iliev et al. (2006) Test2: HII region expansion in a uniform gas with varying temperature and static gas particles at time $t = 100$ Myr. *Top left:* a slice of the hydrogen neutral fraction through the center; *Top right:* a slice of the gas temperature through the center; *Bottom left:* hydrogen neutral fraction as a function of radius; *Bottom right:* temperature as a function of radius. The red points represent the values of individual particles. The vertical error bars show the mean and standard deviation. The horizontal error bars show the smoothing length. The solid black line is the ‘TT1D thin’ result (Pawlik & Schaye 2011) and the shaded region is the upper and lower bounds of the Iliev et al. (2006) results. Here we inject radiation over three smoothing lengths.

is not completely ionized and the analytical solution of Eq. (C5) is only approximately correct¹⁶. Because of this, we compare our simulation results to another simulation code, namely C2-ray (Mellema et al. 2006) (see also Iliev et al. 2006) and, follow them by defining the position of the I-front as the radius at which $x_{\text{HI}} = 0.5$.

Fig. 9 demonstrates that our results converge for $\tilde{c} \rightarrow c$, and even when $\tilde{c} = c/100$ are close to those obtained with C2-ray. Using $\tilde{c} = c/1000$, we notice deviations of a few tens of percent at times less than a recombination time, and much

smaller than 10 per cent later on. This matches our expectation discussed in §2.11 (see also Rosdahl et al. 2013). The scheme works well at low resolution even when using non-uniform particle distributions. This is important because in typical applications (*e.g.* reionization simulations or simulations of the interstellar medium) the gas distribution around the ionizing sources is often at best marginally resolved.

¹⁶ The mean free path of ionizing photons is $\lambda = n_{\text{H}}\sigma_{\gamma} \approx 0.04$ kpc and not resolved in the simulation setup.

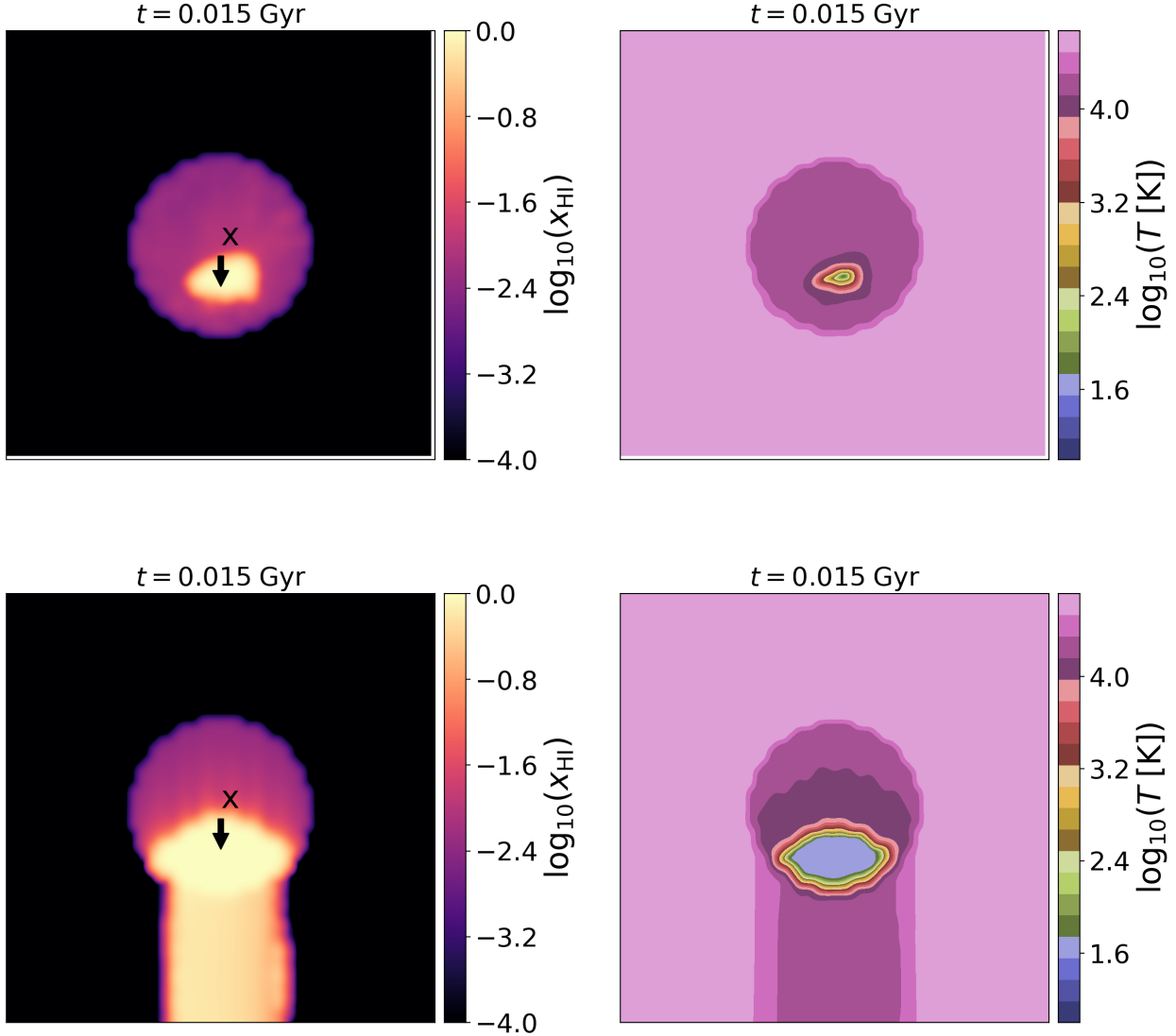


Figure 11. Iliev et al. (2006) Test 3: I-front trapping in a dense clump. *Left:* a slice of mass-weighted hydrogen neutral fraction through the midplane of the simulation volume at $t = 15$ Myr; *Right:* same but for temperature. *Upper panels:* for the default optically thin direction, $\hat{\mathbf{n}} = \hat{\mathbf{f}}$; *Lower panels:* for an imposed fixed optically thin direction in the x direction (see §2.5.1), as shown by the arrows.

3.3 Radiation tests without hydrodynamics: variable temperature

3.3.1 Static Strömgren Sphere with Thermodynamics

We repeat the previous test, but now allow photo-heating of the ionized gas, testing the interaction between the radiative transfer and the photo-chemistry solver. The parameters of the test are identical to the previous case; the photo-heating and cooling processes are detailed in Appendix A (the test makes the on-the-spot approximation). We use the optically thin value for the photo-heating energy rate per ionization, ϵ_γ (see Appendix A). The underlying particle distribution is glass-like with 32 particles on a side; the injection radius is three smoothing lengths (see §2.9); and $\tilde{c} = 0.01c$. Fig. 10 summarises our simulation results.

We compare our results to results for the same setup

published by Iliev et al. (2006), since this test has no known analytical solution. Unfortunately the comparison is not straightforward because some codes in that paper use different values for the thermo-chemistry coefficients (see Fig. 2 in Iliev et al. 2006), and some codes use multi-frequency RT to account for spectral hardening. Spectral hardening leads to pre-heating of gas upstream from the ionization front. To make the comparison appropriate, we also compare to TT1D (TestTrophic1D), which is a 1D radiative transfer code developed by Pawlik & Schaye (2008, 2011) for testing the TRAPHIC code. We will compare to their ‘TT1D thin’ result, which uses the same assumptions as ours, *i.e.* one frequency bin (grey approximation) and photoheating in the optically thin limit. Fig. 10 demonstrates that our scheme produces a roughly spherical morphology at this resolution with the mean value at a given radius matching those obtained by

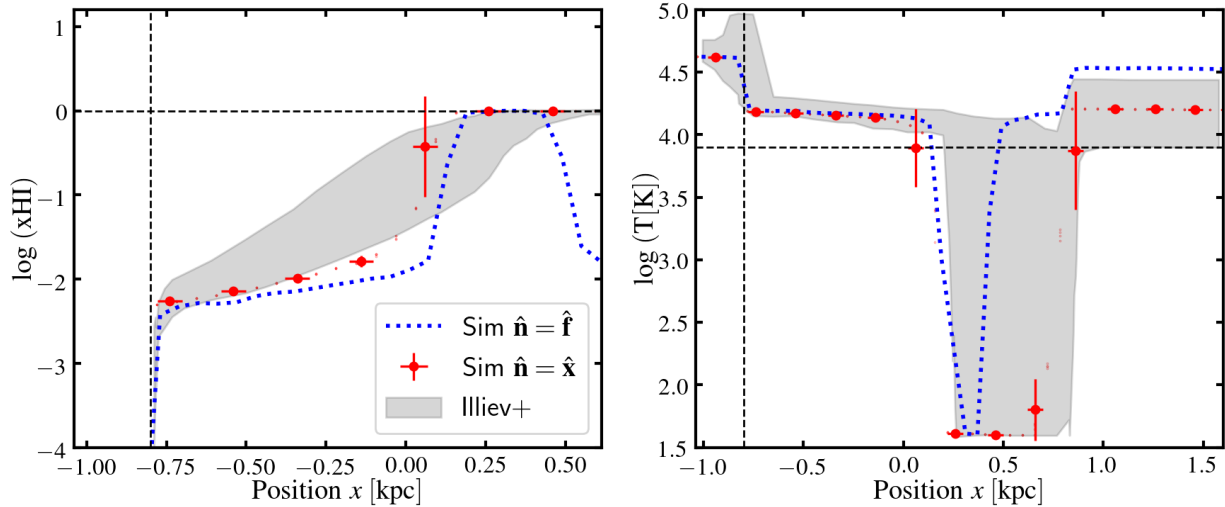


Figure 12. Iliev et al. (2006) Test 3: I-front trapping in dense clump at $t = 15$ Myr. *Left:* the neutral fraction along the axis of symmetry through the centre of the clump, where $x = 0$; *Right:* the corresponding plot for temperature. The red points represent the values of individual particles (particles with distance < 0.1 kpc from the axis). The vertical errorbars show the mean and standard deviation and the horizontal errorbars show the smoothing length. The blue dashed lines show the result if we do not fix the optically thin direction. The shaded region encompasses the upper and lower bounds of the Iliev et al. (2006) results. Vertical dashed lines show the initial clump front position, whereas horizontal dashed lines show the initial neutral fraction and temperature. We only show the results for the case when the direction of the flux is imposed to be the optically thin direction (§2.5.1).

TT1Dthin. In addition, our result falls within the grey-band defined by the range of simulation results published by Iliev et al. (2006).

3.3.2 Ionization Front trapping with a Dense Clump

Next, we illustrate our scheme’s ability to trap an ionization front and cast a shadow, by repeating ‘Test 3’ in Iliev et al. 2006. The setup is as follows: a cubic volume of linear extent 4.0 kpc is filled with hydrogen gas of density $n_{\text{out}} = 2 \times 10^{-4} \text{ cm}^{-3}$ and temperature $T_{\text{out}} = 8000$ K. A spherical cloud with radius 0.8 kpc, hydrogen density $n_{\text{clump}} = 0.04 \text{ cm}^{-3}$ and temperature $T_{\text{clump}} = 40$ K is placed at the centre of the volume. The system is irradiated from the top with a black-body spectrum with temperature $T_{\text{BB}} = 10^5 \text{ K}$, injecting a constant photon flux of $10^6 \text{ photons s}^{-1} \text{ cm}^{-2}$ from the upper computational boundary. We impose absorbing boundary conditions at the lower computational boundary and periodic boundary conditions at all other computational boundaries.

The SPH particle distribution is glass-like with approximately 64^3 particles (which is lower than the tests published in Iliev et al. (2006) but enough to demonstrate the performance of our scheme). We model the over-density of the gas in the clump by increasing the hydrogen fraction of the SPH particles in the clump. We use the RSL approximation, setting $\tilde{c} = c/10$.

We show the simulation results in Fig. 11, with (lower panels) and without (upper panels) imposing the optically thin propagation direction for the radiation, $\hat{\mathbf{n}} = \hat{\mathbf{x}}$, (§2.5.1). As expected, the gas in front of the high-density region is highly ionized; inside the high-density region but upstream from the ionization front it is ionised to a level $n_{\text{HI}}/n_{\text{H}} \sim$

10^{-2} ; the ionization front is trapped inside the high-density region at $x \sim 0.1$ kpc, and finally the gas is mostly neutral behind the ionization front in the shadow behind the high-density region.

We follow the reasoning of §2.8.3 to estimate the temperature immediately after the ionization front has passed,

$$T_1 = \frac{2 - x_0}{2 - x_1} T_0 + \frac{2}{3} \frac{x_0 - x_1}{2 - x_1} \frac{\epsilon_\gamma}{k_B}, \quad (61)$$

where x_0 and T_0 are the initial neutral fraction and temperature, x_1 and T_1 are the neutral fraction and temperature when the ionization front has passed, and $\epsilon_\gamma \approx 6.33$ eV is the photoheating per ionization. In front of the high-density region, we take $x_0 = 1$, $T_0 = 8000$ K and $x_1 \approx 0$ to find $T_1 = 10^{4.45}$ K; upstream from the ionization front inside the high-density region, we take $x_0 = 1$, $T_0 = 40$ K, $x_1 = 10^{-2}$ to find $T_1 = 10^{4.38}$ K. Once the front has passed, the gas will continue to be photoheated while also cooling radiatively. In front of the high-density region, the recombination time, $\tau_r \equiv 1/(\alpha_B n_{\text{H}}) \approx 600$ Myr, is long compared to the simulation time, and the gas is still heating slowly to its new equilibrium temperature of $10^{4.64}$ K. Inside the high-density region, $\tau_r \approx 3$ Myr is short compared to the simulation time and the gas should be in thermal equilibrium. Scaling the flux so that the neutral fraction is $10^{-2.2}$, close to what is found in the simulation at the front of the high-density region, yields an equilibrium temperature of $\approx 10^{4.18}$ K, consistent with what we find in the simulation (Fig. 12).

When the propagation direction is imposed, the over-dense gas traps the I-front at time $t = 15$ Myr, and the run of the neutral fraction and temperature from the top of the volume in the x -direction follows our analytical estimates. It also falls within the grey-region, defined by the the locus of the simulation results for the different codes for Test 3 in

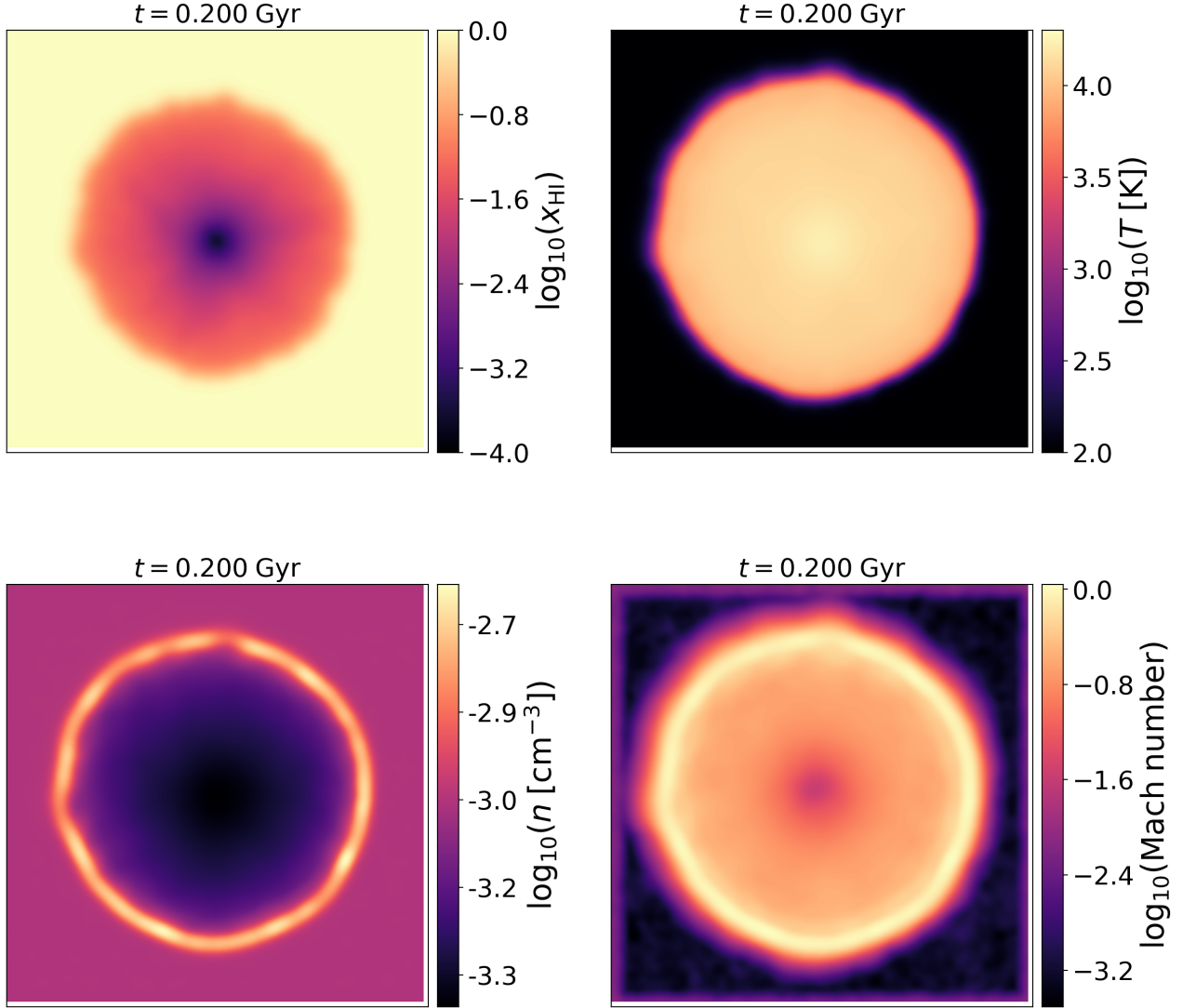


Figure 13. Slices of neutral fraction (*upper left*), temperature (*upper right*), gas density (*lower left*), and Mach number (*lower right*) through an HII region expanding in an initially uniform medium (Iliev et al. 2009 Test 5) at $t = 200$ Myr through the centre of the HII region. Hydrodynamics is turned on and we inject radiation over two smoothing lengths.

Iliev et al. (2006), as shown in Fig. 12. The shadow is relatively sharp, with a small level of ionization at its boundary due to the numerical/artificial diffusion. As expected, the gas is also cooler in the shadow with the temperature there agreeing with the results of some of the codes in Iliev et al. (2006). As in the previous test case, our results are not directly comparable to some of the codes in Iliev et al. (2006), in particular codes that perform multi-frequency RT capture the pre-heating ahead of the ionization front due to the smaller optical depth of higher-energy photons.

When the direction of propagation is not imposed (top panels in Fig. 11 and Fig. 12), the ionization front is still trapped in the high-density region and there is still a fraction of self-shielded gas. However, the numerical and/or artificial diffusion wipes-out the shadow. Some high-density gas

down-stream from the ionization front also gets ionized as a consequence of artificial diffusion.

While fixing the optically-thin direction is less relevant for simulations with many sources, this approach is useful for a few radiation sources or the propagation of radiation fronts in a few directions, which we are currently investigating.

3.4 Radiation tests with hydrodynamics and variable temperature

In this section we present tests with heating, cooling, and hydrodynamics with radiation¹⁷.

¹⁷ We ignore the $\nabla \mathbf{v} : \mathbb{P}$ and radiation pressure terms (see §2.3) in these test problems.

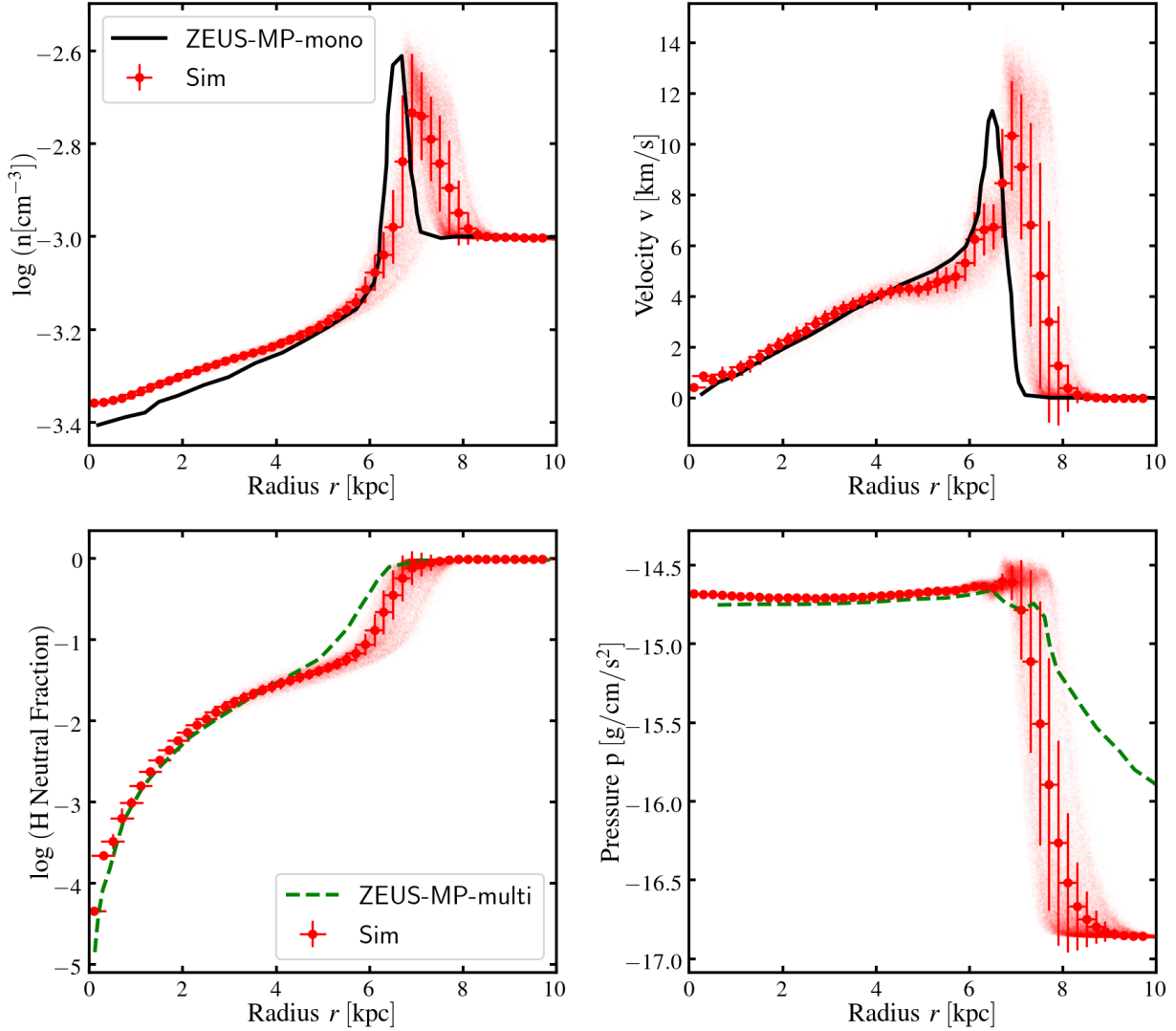


Figure 14. Gas density (*upper left*), gas velocity (*upper right*), neutral fraction (*lower left*), and pressure (*lower right*) as a function of radius of the HII region expansion in an initially uniform medium (Iliev et al. 2009 Test 5) at $t = 200$ Myr. The red points represent the values of individual particles. The vertical error bars show the mean and standard deviation. The horizontal error bars show the smoothing length. The lines are the results from the ZEUS-MP code (Whalen & Norman 2006) in Iliev et al. (2009). Black solid represents monochromatic light, i.e. a single frequency bin, similar to our implementation, whereas green dashed lines represent multi-frequency transfer. Injecting radiation over two smoothing lengths results causes the ionization front to propagate slightly faster than seen in ZEUS-MP.

3.4.1 Strömgren Sphere with hydrodynamics

The first test is a repeat of the HII region, but now allowing the gas to expand as it is heated; this is Test 5 in Iliev et al. (2009). The problem setup and conditions are exactly identical to the variable temperature Strömgren sphere test in §3.3, but we simulate also the hydrodynamics response of the gas. We use the default SPHENIX SPH formulation for hydrodynamics (§2.5) with 64^3 particles in the computational volume.

We do *not* fix the optically thin direction here, but instead inject radiation over two smoothing lengths. We find that the ionized region is nevertheless almost spherically symmetric (as it should be). However, the location of the front is slightly further out compared to the profile com-

puted with ZEUS-MP. This is because this way of injecting radiation does not quite guarantee that the flux drops correctly with distance in the injection region. Figure 13 shows that the gas profiles are approximately spherically symmetric and there is no evidence of any numerical instabilities.

In Fig. 14 we compare our simulation results (red points show values for individual SPH particles, blue points show the mean and scatter of values in radial bins) to those of ZEUS-MP single-frequency bin result (black solid lines), as published by Iliev et al. (2009). For the gas neutral fraction and pressure, the single-frequency bin result is not available, so we compare to the multi-frequency ZEUS-MP result instead.

As the gas is ionized and heated, the surrounding gas

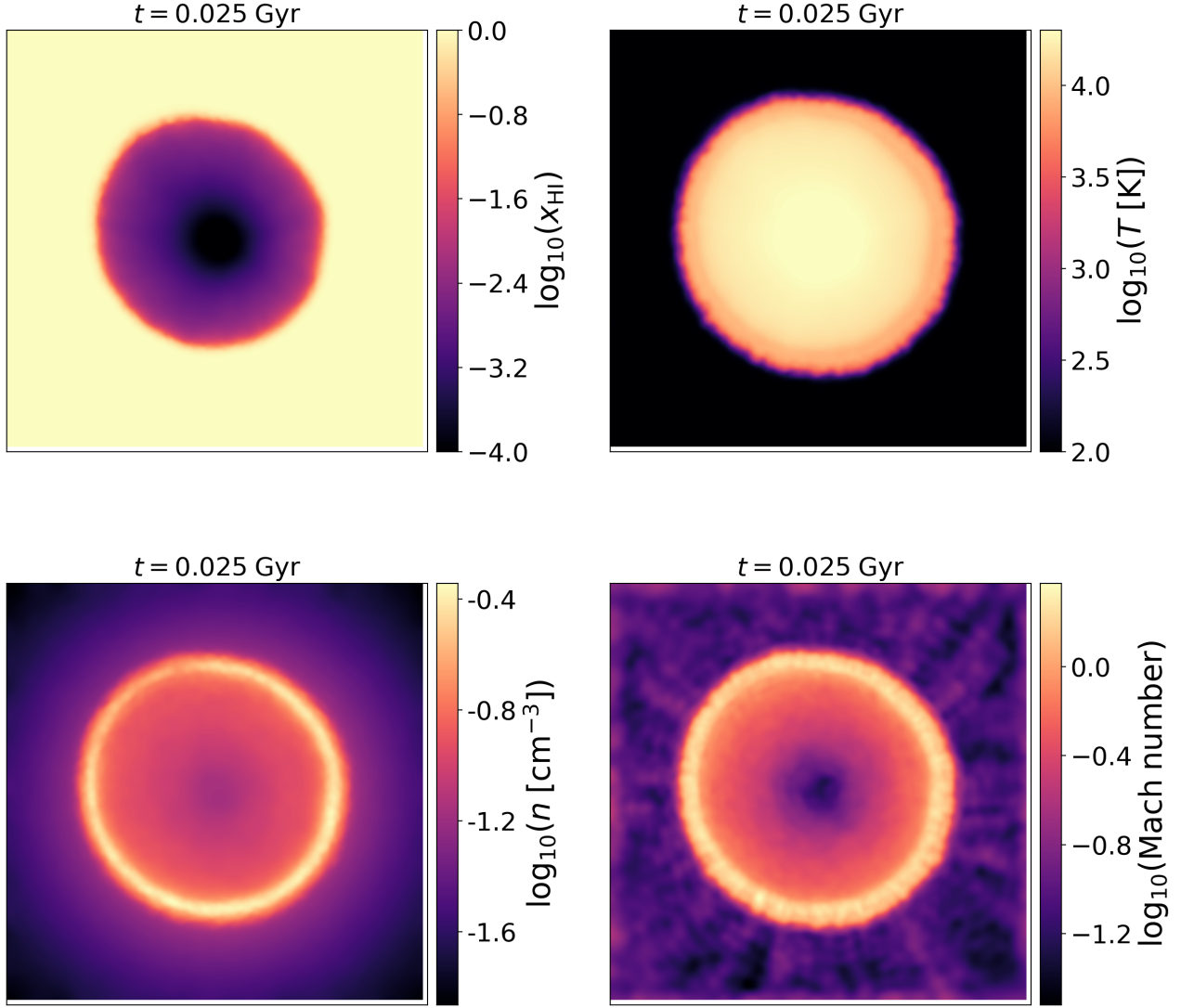


Figure 15. Slices of neutral fraction (*upper left*), temperature (*upper right*), gas density (*lower left*), and Mach number (*lower right*) through an HII region expanding in a medium with initial density profile $\propto r^{-2}$ (Iliev et al. 2009 Test 6) at $t = 25$ Myr through the centre of the HII region. Hydrodynamics is turned on and we inject radiation over two smoothing lengths.

is swept-up in a dense shell. The location of the shell agrees well with that found by ZEUS-MP, as do gas neutral fraction, density and velocity profiles. In our simulation, the shell is somewhat wider than that found by ZEUS-MP, partly because of our much lower resolution and possibly due to the applied artificial viscosity in the hydrodynamics solver.

Our pressure profile agrees with ZEUS-MP-multi until $r = 8$ kpc, where ZEUS-MP-multi shows a slower falloff in pressure. This is because ZEUS-MP-multi includes also *spectral hardening*, where high frequency photons penetrate further into the neutral medium. Our current single-bin method cannot model this effect.

3.4.2 Strömgren Sphere in a $1/r^2$ density profile with hydrodynamics

Finally, we examine how our code performs in the case when the density is not uniform (Iliev et al. 2009 Test 6). This allows us to validate our hierarchical time-stepping scheme (§2.10) and test the propagation of radiation down a density slope.

We initialise a density profile $n_H(r)$ as a function of radius r from the center, given by

$$n_H(r) = \begin{cases} n_{\text{core}}, & \text{if } r < r_{\text{core}}, \\ n_{\text{core}}(r_{\text{core}}/r)^2, & \text{if } r > r_{\text{core}}, \end{cases} \quad (62)$$

by distributing $\sim 64^3$ equal-mass SPH particles in a $(2 \text{ kpc})^3$

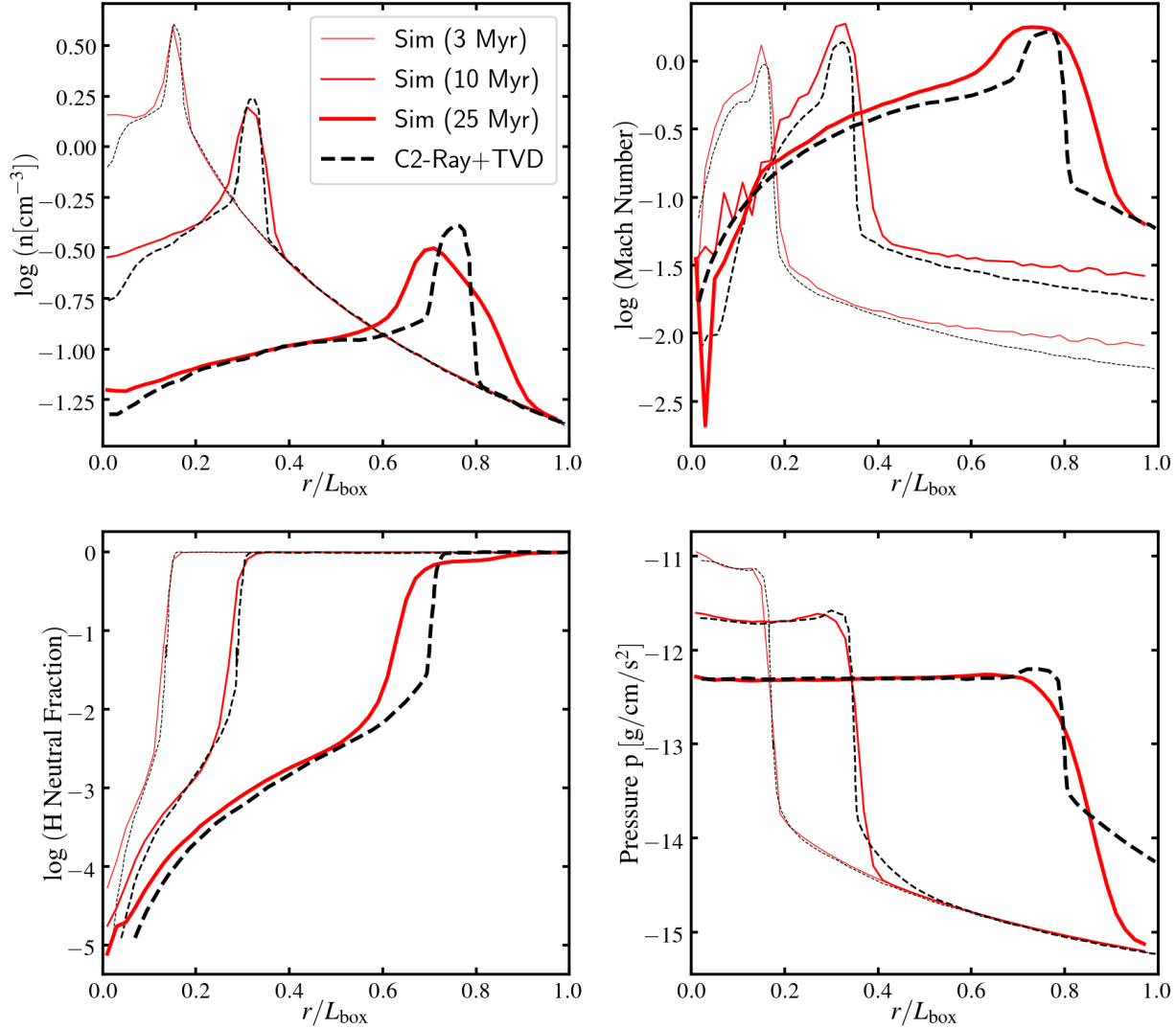


Figure 16. Gas density (*upper left*), Mach number (*upper right*), neutral fraction (*lower left*), and pressure (*lower right*) as a function of radius of the HII region expanding in an initially $1/r^2$ density profile (Iliev et al. 2009 Test 6) at times $t = 3, 10, 25$ Myr (thicker lines at later times). The computational volume in the original Iliev et al. 2009 test has a linear extent of $L_{\text{box}} = 0.8$ kpc. The *red solid lines* represent the mean values from our simulations; the *black lines* are the results from the C2-Ray+TVD code, which uses multi-frequency RT transfer.

box^{18} . We take $n_{\text{core}} = 3.2 \text{ cm}^{-3}$ and $r_{\text{core}} = 91.5 \text{ pc}$. We also set up a star particle at the center of the box which emits 10^5 K black body spectrum photons at a rate of $\dot{N}_\gamma = 10^{50} \text{ photons s}^{-1}$. We choose to inject radiation over one smoothing length and set $\tilde{c} = 0.01c$ in this test.

Initially, the R-type ionization front moves quickly on a time-scale $\ll 1 \text{ Myr}$ stalling at the initial Strömgren radius at $r_s \sim 70 \text{ pc}$. Then the gas itself starts to expand as it is heated and the ionization front expands slowly towards the edge of the computational volume. The ionization front accelerates once it exits the core region, due to the lower gas density at a larger radius.

¹⁸ We use a slightly larger box size than Iliev et al. (2009) (box size = 1.6 kpc) since we adopt periodic boundary condition rather than transmissive BCs and we want to avoid edge effects.

In Fig. 15 we plot slices through the neutral gas fraction, temperature, density, and Mach number at time $t = 25 \text{ Myr}$. The profiles are approximately spherically symmetric in the ionized region, although there are some deviations from spherical symmetry caused by the non-uniform particle distribution. There is also some noise visible in the Mach number slice outside the ionization front, because it is difficult to set up a completely static SPH density field when the density distribution has a steep gradient.

In Fig. 16, we compare spherically-averaged radial profiles to the results obtained with the C2-Ray+TVD code (Mellema et al. 2006; Trac & Pen 2004). Our results agree reasonably well on the location and speed of the ionization front, as well as on the run of density, mach number, ionised fraction and pressure. The biggest differences occur in the outer parts that have not been reached yet by the radia-

tion. These differences are a consequence of how the initial conditions are set up: in SPH, it is difficult to set up the initial conditions very accurately. Furthermore, C2-Ray+TVD has higher pressure downstream from the ionization front, because, unlike in our implementation, it performs multi-frequency RT, so that gas downstream from the ionization front undergoes preheating.

4 DISCUSSION

In the previous sections, we have demonstrated that our RT implementation accurately propagates radiation in the optically thin limit, preserving the direction of propagation and advancing the radiation front at the correct speed (§2 and §3.1). In three dimensions, it accurately reproduces the initial expansion of an ionization front around a source, and its asymptotic slow down to the Strömgren radius. The implementation also handles ionization front trapping (§3), reproducing results accurately also when the hydrodynamics of the gas is accounted for, even at moderate numerical resolution (§3.4).

Importantly, the method has favourable computational scaling, which is proportional only to the number of gas particles, and independent of the number of sources. By implementing a ‘reduced speed of light’ method, the time-step associated with radiation propagation can be dramatically increased (see §2.11). The thermo-chemistry uses sub-cycling in order to decouple the short ionization timescales from the much longer radiation propagation timescale (see §2.8).

The RT implementation inherits the full spatial and temporal adaptivity of the underlying gas dynamics scheme (e.g. §3.4). The method as described can be combined with any SPH code, without any need for extra structures (e.g. grids, rays, photon packets, or angular discretization).

However, the method also has limitations, e.g. those associated with the closure relation and numerical noise. In this section, we discuss these limitations in more detail.

4.1 Limitations of the Two-Moment M1 method

4.1.1 Approximations in the Moment Closure

As discussed in §2, the two-moment method results from truncating an infinite hierarchy of moment equations by postulating a closure relation for the Eddington tensor. The choice of closure relation affects the accuracy of the method.

The ‘M1 closure relation’ is not exact in the regime intermediate between optically thin and optically thick, even in the case of a single source. As shown by Levermore (1984), this is because in such a situation the closure relation cannot be uniquely determined by the first two moments. Secondly, this closure relation cannot handle situations where particles receive radiation from two or more directions, even in the optically thin regime (see §2.4 and §4.1.1). In such cases, beams of radiation ‘collide’ with each other rather than simply pass through one another as they should do. The reason for this is twofold. Firstly, the M1 closure relation of Eq. (17) erroneously implies that the radiation is optically thick when two beams collide (see also Fig. 1 in Rosdahl et al. 2013). Secondly, the form of the Eddington tensor in Eq. (13) im-

plicitly assumes that radiation is moving in a single direction (single stream, plus an additional isotropic component).

We illustrate the ‘collision of radiation’ in Fig. 17. The setup is as follows: two sources emit a burst of radiation isotropically into an optically thin medium. This results in two spherical shells of radiation, propagating away from each source. When these shells overlap, they *should* simply pass through each other. When this situation is simulated with the M1 closure relation, the shells ‘collide’ instead, erroneously producing two spikes of radiation. Such collisions could significantly distort the radiation morphology e.g. when sources are associated with multiple star clusters or multiple galaxies.

There are several ways to improve the method to reduce the impact of such collisions. Firstly, we introduced the modified M1 closure relation in Eq. (19). This new closure relation does not lead to radiation collision in one dimension, as shown in Fig. 18. The reason is that this modified closure relation correctly identifies that the radiation is optically thin even where the two beams collide (unlike the original M1 close relation).

Unfortunately, the modified closure scheme still cannot handle the collision of optically thin beams, which is not head-on. Hence it does not resolve the problem illustrated in Fig. 17. A possible way forward would be to resort to higher order methods, e.g. Vikas et al. (2013) and Levermore (1996). However, a stable and efficient high-order method has not been discussed in the astrophysics literature, as far as we are aware. Another avenue might be to calculate the closure relation itself more accurately, for example using short characteristic (Finlator et al. 2009; Jiang et al. 2012) or using a Monte Carlo scheme (Foucart 2018). Unfortunately, both these schemes are computationally more expensive in the case of multiple bright sources.

4.1.2 Numerical/Artificial Noise

Another limitation of the moment method, which is not restricted to the two-moment or M1 methods, is numerical noise. Such noise can destroy the coherence of the radiation even in the optically thin regime (see e.g. Fig. 1), or cause radiation to propagate into a shadow (see e.g. Fig. 11).

There are two major sources of noise. Firstly, the discretization of the density field into a disordered set of SPH particles, which is especially problematic when the symmetry of the particle distribution differs from that of the radiation field and/or when the numerical resolution is low. In addition, SPH suffers from ‘zeroth-order errors’ that are also particularly severe when the particle distribution is irregular (see §1, Dehnen & Aly 2012); our SPH formulation is designed to minimize these (see §2.5). Higher-order SPH schemes could reduce such SPH noise further (e.g. Vila 1999; Gaburov & Nitadori 2011; Rosswog 2015; Hopkins 2015; Frontiere et al. 2017).

The second major source of noise is the discontinuity-capturing artificial dissipation, which can introduce unphysical diffusion and damping. We have tried to limit the severity of such artefacts by introducing *anisotropic* viscosity as well as a *higher-order* artificial diffusion scheme. Even so, our artificial diffusion is not completely anisotropic, so that a small amount of radiation still diffuses artificially perpendicular to the propagation direction of a beam of radiation (see Figs. 5

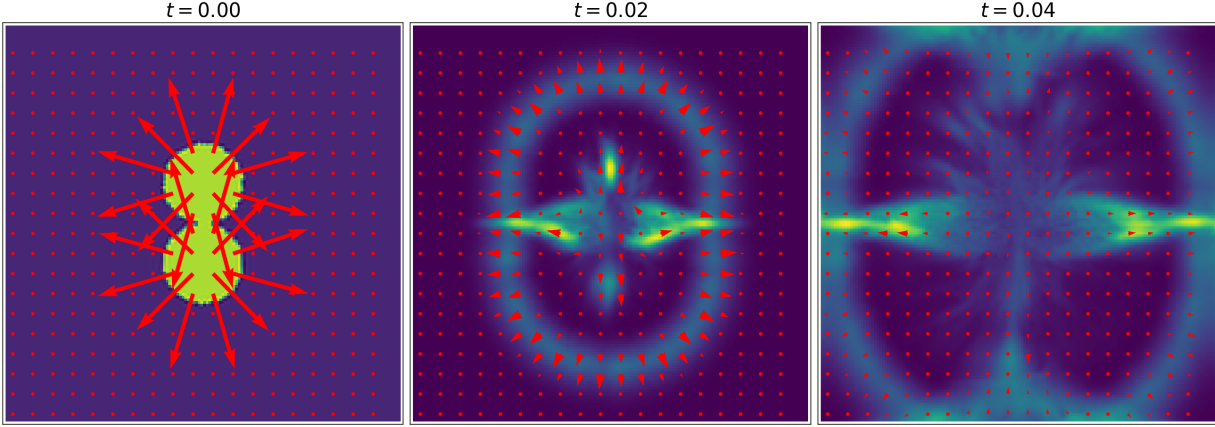


Figure 17. Radiation collision in two dimensions: spherical radiation fronts emanate from two sources into an optically thin medium. The setup is the same as Fig. 6, but with two spherical fronts instead of one. The panels from left to right show the initial conditions and the state at later times of $t = 0.02$ and 0.04 when the spherical fronts overlap. The simulation uses the modified M1 closure relation (Eqs. 13 and 19). Colors represent the radiation energy density, red arrows show the radiation fluxes. Whereas the shells should pass through each other, this closure relation results in a collision of the two fronts, resulting in the formation of horizontal beams of light.

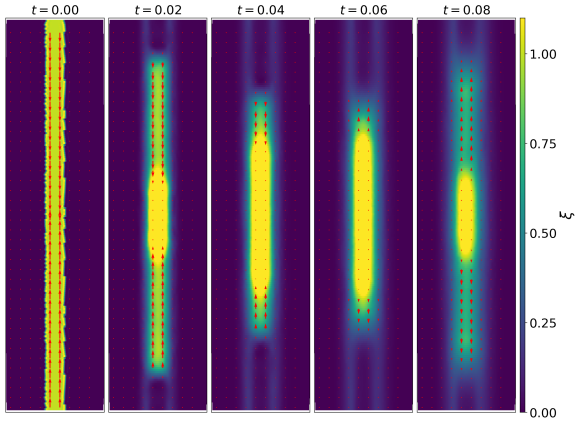


Figure 18. A short beam of radiation propagating to the top, colliding with a short beam of radiation propagating to the bottom, simulated with the default two-moment method (see §2.7) in an optically thin medium (with the same condition as in Fig.1, except there is an extra radiation beam pointing downward). Colors represent the radiation energy density, whereas the red arrows show the radiation fluxes. This shows our modified M1 closure (Eq.19) can handle the head-on beam collision problems.

and 11). We suggest that higher order artificial anisotropic diffusion, similar to that used in the HLL Riemann solver (Harten et al. 1983), might reduce these artefacts.

Our method can further reduce unphysical diffusion in cases where it is possible to impose the direction of propagation of the radiation.

4.1.3 Computational Cost

Another limitation of the M1 method is that the computational cost may be high in some physically interesting situations, *e.g.* when capturing the final stages of reionization when the reduced speed of light needs to be close to c to capture the speed of ionization fronts correctly (e.g. Bauer et al. 2015). Possible improvements include using a ‘variable speed of light approximation’ (see §2.11, Katz et al. 2017) or implementing the radiation transfer on graphics processing units (Ocvirk et al. 2016). Subcycling the radiative transfer module can further improve the performance of the overall code (Rosdahl et al. 2013; Kannan et al. 2019).

However, we emphasise that the computational cost of our method scales with the number of gas particles, N_{gas} , more favourably than ray-tracing methods (which additionally scale with the number of sources) and OTVET (which scales with the $N \log N$ scaling of its Poisson solver).

4.2 A comparison with other M1 codes

The two-moment M1 method is a popular scheme in the field of galaxy formation simulations and is implemented in *e.g.* ATON (Aubert & Teyssier 2008), RAMSES-RT (Rosdahl et al. 2013), and AREPO-RT (Kannan et al. 2019). The first two codes are Eulerian schemes, whereas AREPO-RT is a moving mesh scheme (Springel 2010).

Our implementation in the SWIFT code takes advantages of the Lagrangian nature of SPH, which is important, particularly when gas flows at high speeds. This is a great advantage compared to Eulerian codes, especially at relatively low resolution (Robertson et al. 2010) and high redshift (Pontzen et al. 2020). While Eulerian mesh codes can gain adaptivity through the adaptive mesh refinement, the refinement and de-refinement are not trivial and can be noisy.

AREPO-RT and our code can follow fluid motions and

are highly adaptive, so both of them are advantageous in galaxy formation simulations, where the large dynamic range and high speeds of the gas are both numerically challenging.

We think that the main advantages of our scheme are its computational efficiency and its parallelizability. The moving mesh code requires mesh reconstruction, which can be computationally expensive; such reconstruction is not necessary in SPH. SPH codes can also be parallelized efficiently through task-based parallelism, *e.g.* ChaNGa (Jetley et al. 2008) and SWIFT (Schaller et al. 2016), the code in which our method is implemented.

5 SUMMARY

We have developed a numerical radiation hydrodynamics scheme based on the two-moment method and using an improved closure relation. The two-moment method is based on the first two moments of the radiation moment hierarchy, and the hierarchy is closed with an Eddington closure relation. The M1 Eddington tensor closure is the simplest anisotropic closure that maximizes the entropy (see §2), our modified closure relation improves the stability of the method, in particular in the optically thin regime. The numerical scheme is implemented in the smoothed particle hydrodynamics (SPH) code SWIFT (Schaller et al. 2016). The interaction of radiation with a pure hydrogen gas is implemented in non-equilibrium, using sub-cycling to improve computational speed.

Key aspects of the method and its implementation include:

- the first stable and accurate SPH implementation of the two moment method (Eqs. 24 and 25);
- improvements to the M1 closure relation (Eq. 19), making the method (1) less prone to noise in the optically thin regime (enabling the implementation of the two moment method in SPH) and (2) correct in the optically thin limit;
- anisotropic artificial viscosity and high-order artificial diffusion schemes (§2.6) to capture discontinuities in the radiation. These are essential to propagate radiation accurately in the optically thin regime;
- an efficient non-equilibrium thermo-chemistry solver with sub-cycling (§2.8);
- implementation in SWIFT, a task-based parallel SPH galaxy simulation code (Schaller et al. 2016).

The accuracy and stability of the scheme is demonstrated in §3. The scheme:

- preserves the directions and speed of propagation in the optically thin regime;
- can simulate radiation hydrodynamics in dynamical multi-scale problems;
- has accuracy comparable to other radiative transfer codes in the cosmological code comparison papers (Iliev et al. 2006, 2009).

Note that the method yields robust results for spherically symmetric problems, *e.g.* Strömgren sphere, even without imposing that radiation propagates radially, provided that the injection region is sufficiently well sampled; see §2.9 & 3.2.

The main advantage of our scheme (and of moment methods in general) as compared to other radiative transfer schemes, is that it is computationally efficient in large-scale simulations with numerous sources, since this cost is independent of the number of sources (which has been demonstrated in many other studies; see §1). Our scheme is also highly adaptive in both space and time, since the radiation field is directly sampled by individual SPH particles.

Our scheme can be also implemented in other SPH codes without requiring substantial structural changes. This is because the two-moment equations resemble the set of hydrodynamic equations themselves, *e.g.* the radiation energy density equation resembles the gas density equation, and the radiation flux equation resembles the momentum equation of hydrodynamics. The artificial dissipation terms for the propagation of radiation are also very similar to the artificial viscosity and diffusion terms in SPH.

This method was developed to enable tracking of the propagation of ionizing radiation through the intergalactic medium or interstellar medium in galaxy simulations. It should be sufficiently accurate to correctly model the propagation of ionization fronts and cast shadows behind optically thick absorbers, while at the same time being sufficiently efficient to be able to handle thousands of sources without overly slowing down the calculations.

The M1 method has also been applied to study the effect of diffuse radiation or account for multiple scattering events, for example, when studying the transport of IR radiation in the interstellar medium, where multiply-scattered IR photons are thought to be important in transferring momentum to gas (*e.g.* Skinner & Ostriker 2013; Rosdahl & Teyssier 2015; Kannan et al. 2019). We intend to extend our code to be able to study these problems in the future.

We are aiming to release this code to the community in the near future, after we have completed the following two improvements. First, we are implementing multi-frequency radiative transfer so that we can include Helium in the calculations. Multi-frequency radiation also enables the modelling of spectral hardening. Secondly, we are improving the efficiency of the implementation by decoupling the update of the hydrodynamics variables and the radiation variables, *i.e.* sub-cycling the radiation transport module. Taking advantage of the very different time-scales for the motion of gas and of radiation should lead to a large speed-up in computing time. We will report on these improvements and demonstrate the efficiency of our code elsewhere.

ACKNOWLEDGEMENTS

We thank J. Borrow, M. Schaller, M. Ivkovic, L. Hausamann, and C. Correa for their assistance with the implementation in SWIFT, and A. Richings, Y. Revaz, and A. Benítez-Llambay for helpful discussions. We thank Joakim Rosdahl for a thoughtful and constructive referee's report, which led to significant improvements to our paper.

This work was supported by the Science and Technology Facilities Council (STFC) through Consolidated Grants ST/P000541/1 and ST/T000244/1 for Astronomy at Durham. We acknowledge support from the European Research Council through ERC Advanced Investigator grant, DMIDAS [GA 786910] to CSF. This work

used the DiRAC@Durham facility managed by the Institute for Computational Cosmology on behalf of the STFC DiRAC HPC Facility (www.dirac.ac.uk). The equipment was funded by BIS capital funding via STFC capital grants ST/K00042X/1, ST/P002293/1, ST/R002371/1 and ST/S002502/1, Durham University and STFC operations grant ST/R000832/1. DiRAC is part of the National e-Infrastructure.

The research in this paper made use of the SWIFT open source simulation code (<http://www.swiftsim.com>, Schaller 2018) version 0.9.0 This work also made use of matplotlib (Hunter 2007), numpy (van der Walt et al. 2011), scipy (Jones et al. 2001), swiftsimio (Borrow & Borisov 2020), and NASA’s Astrophysics Data System.

DATA AVAILABILITY

The data underlying this article will be shared on reasonable request to the corresponding author (TKC).

REFERENCES

- Abel T., Haehnelt M. G., 1999, *ApJL*, 520, L13
 Abel T., Wandelt B. D., 2002, *MNRAS*, 330, L53
 Agertz O., et al., 2007, *MNRAS*, 380, 963
 Altay G., Theuns T., 2013, *MNRAS*, 434, 748
 Altay G., Croft R. A. C., Pelupessy I., 2008, *MNRAS*, 386, 1931
 Anninos P., Zhang Y., Abel T., Norman M. L., 1997, *New Astron.*, 2, 209
 Aubert D., Teyssier R., 2008, *MNRAS*, 387, 295
 Baek S., Di Matteo P., Semelin B., Combes F., Revaz Y., 2009, *A&A*, 495, 389
 Baes M., Camps P., 2015, *Astronomy and Computing*, 12, 33
 Bauer A., Springel V., Vogelsberger M., Genel S., Torrey P., Sijacki D., Nelson D., Hernquist L., 2015, *MNRAS*, 453, 3593
 Borrow J., Borisov A., 2020, *Journal of Open Source Software*, 5, 2430
 Borrow J., Bower R. G., Draper P. W., Gonnet P., Schaller M., 2018, *Proceedings of the 13th SPHERIC International Workshop*, Galway, Ireland, June 26-28 2018, pp 44–51
 Borrow J., Schaller M., Bower R. G., Schaye J., 2020, *arXiv e-prints*, p. arXiv:2012.03974
 Bromm V., Yoshida N., Hernquist L., McKee C. F., 2009, *Nature*, 459, 49
 Buchler J. R., 1983, *Journal of Quantitative Spectroscopy and Radiative Transfer*, 30, 395
 Cantalupo S., Porciani C., 2011, *MNRAS*, 411, 1678
 Cantalupo S., Porciani C., Lilly S. J., Miniati F., 2005, *ApJ*, 628, 61
 Cen R., 1992, *ApJS*, 78, 341
 Chow E., Monaghan J. J., 1997, *Journal of Computational Physics*, 134, 296
 Cohen S. D., Hindmarsh A. C., Dubois P. F., 1996, *Computers in Physics*, 10, 138
 Commerçon B., Teyssier R., Audit E., Hennebelle P., Chabrier G., 2011, *A&A*, 529, A35
 Cullen L., Dehnen W., 2010, *MNRAS*, 408, 669
 Davis S. W., Stone J. M., Jiang Y.-F., 2012, *ApJS*, 199, 9
 Dehnen W., Aly H., 2012, *MNRAS*, 425, 1068
 Dubroca B., Feugeas J., 1999, *Academie des Sciences Paris Comptes Rendus Serie Sciences Mathematiques*, 329, 915
 Ferland G. J., Peterson B. M., Horne K., Welsh W. F., Nahar S. N., 1992, *ApJ*, 387, 95
 Ferland G. J., et al., 2017, *RMxAA*, 53, 385
 Finlator K., Özel F., Davé R., 2009, *MNRAS*, 393, 1090
 Foucart F., 2018, *MNRAS*, 475, 4186
 Frontiere N., Raskin C. D., Owen J. M., 2017, *Journal of Computational Physics*, 332, 160
 Gaburov E., Nitadori K., 2011, *MNRAS*, 414, 129
 Gingold R. A., Monaghan J. J., 1977, *MNRAS*, 181, 375
 Gnedin N. Y., Abel T., 2001, *New Astron.*, 6, 437
 Gnedin N. Y., Ostriker J. P., 1997, *ApJ*, 486, 581
 González M., Audit E., Huynh P., 2007, *A&A*, 464, 429
 Graziani L., Maselli A., Ciardi B., 2013, *MNRAS*, 431, 722
 Gunn J. E., Peterson B. A., 1965, *ApJ*, 142, 1633
 Harten A., Lax P. D., Leer B. v., 1983, *SIAM Review*, 25, 35
 Hasegawa K., Umemura M., 2010, *MNRAS*, 407, 2632
 Hayes J. C., Norman M. L., 2003, *ApJS*, 147, 197
 Hernquist L., Katz N., 1989, *ApJS*, 70, 419
 Hopkins P. F., 2015, *MNRAS*, 450, 53
 Hopkins P. F., Grudić M. Y., 2019, *MNRAS*, 483, 4187
 Hopkins P. F., Kereš D., Oñorbe J., Faucher-Giguère C.-A., Quataert E., Murray N., Bullock J. S., 2014, *MNRAS*, 445, 581
 Hopkins P. F., Grudić M. Y., Wetzel A., Kereš D., Faucher-Giguère C.-A., Ma X., Murray N., Butcher N., 2020, *MNRAS*, 491, 3702
 Hui L., Gnedin N. Y., 1997, *MNRAS*, 292, 27
 Hunter J. D., 2007, *Computing in Science and Engineering*, 9, 90
 Iliev I. T., et al., 2006, *MNRAS*, 371, 1057
 Iliev I. T., et al., 2009, *MNRAS*, 400, 1283
 Jetley P., Gioachin F., Mendes C., Kale L. V., Quinn T., 2008, in *2008 IEEE International Symposium on Parallel and Distributed Processing*. IEEE Computer Society, pp 1–12
 Jiang Y.-F., Oh S. P., 2018, *ApJ*, 854, 5
 Jiang Y.-F., Stone J. M., Davis S. W., 2012, *ApJS*, 199, 14
 Jones E., Oliphant T., Peterson P., et al., 2001, *SciPy: Open source scientific tools for Python*, <http://www.scipy.org/>
 Jonsson P., 2006, *MNRAS*, 372, 2
 Jubelgas M., Springel V., Dolag K., 2004, *MNRAS*, 351, 423
 Kannan R., Vogelsberger M., Marinacci F., McKinnon R., Pakmor R., Springel V., 2019, *MNRAS*, 485, 117
 Katz H., Kimm T., Sijacki D., Haehnelt M. G., 2017, *MNRAS*, 468, 4831
 Kegerreis J. A., Eke V. R., Gonnet P., Korycansky D. G., Massey R. J., Schaller M., Teodoro L. F. A., 2019, *MNRAS*, 487, 5029
 Kessel-Deynet O., Burkert A., 2000, *MNRAS*, 315, 713
 Kim J.-G., Kim W.-T., Ostriker E. C., Skinner M. A., 2017, *ApJ*, 851, 93
 Kim J.-h., Wise J. H., Abel T., Jo Y., Primack J. R., Hopkins P. F., 2019, *ApJ*, 887, 120
 Krumholz M. R., Thompson T. A., 2012, *ApJ*, 760, 155

- Lanson N., Vila J.-P., 2008, *SIAM Journal on Numerical Analysis*, 46, 1912
- Levermore C. D., 1984, *J. Quant. Spec. Radiat. Transf.*, 31, 149
- Levermore C. D., 1996, *Journal of Statistical Physics*, 83, 1021
- Levermore C. D., Pomraning G. C., 1981, *ApJ*, 248, 321
- Liu X.-D., Osher S., Chan T., 1994, *Journal of Computational Physics*, 115, 200
- Lucy L. B., 1977, *AJ*, 82, 1013
- Madau P., Meiksin A., 1994, *ApJL*, 433, L53
- Mellema G., Iliev I. T., Alvarez M. A., Shapiro P. R., 2006, *New Astron*, 11, 374
- Mihalas D., Mihalas B. W., 1984, *Foundations of radiation hydrodynamics*. Oxford University Press, New York, USA
- Mihalas D., Auer L. H., Mihalas B. R., 1978, *ApJ*, 220, 1001
- Minerbo G. N., 1978, *Journal of Quantitative Spectroscopy and Radiative Transfer*, 20, 541
- Monaghan J. J., 1997, *Journal of Computational Physics*, 136, 298
- Monaghan J. J., 2002, *MNRAS*, 335, 843
- Morris J. P., Monaghan J. J., 1997, *Journal of Computational Physics*, 136, 41
- Ocvirk P., et al., 2016, *MNRAS*, 463, 1462
- Ocvirk P., Aubert D., Chardin J., Deparis N., Lewis J., 2019, *A&A*, 626, A77
- Osterbrock D. E., 1989, *Astrophysics of Gaseous Nebulae and Active Galactic Nuclei*. Palgrave Macmillan.. University Science Books, Mill Valley, CA, USA
- Owen J. M., 2004, *Journal of Computational Physics*, 201, 601
- Pawlik A. H., Schaye J., 2008, *MNRAS*, 389, 651
- Pawlik A. H., Schaye J., 2011, *MNRAS*, 412, 1943
- Pawlik A. H., Rahmati A., Schaye J., Jeon M., Dalla Vecchia C., 2017, *MNRAS*, 466, 960
- Petkova M., Springel V., 2009, *MNRAS*, 396, 1383
- Petkova M., Springel V., 2011, *MNRAS*, 415, 3731
- Pomraning G. C., 1973, *The equations of radiation hydrodynamics*. Pergamon Press, Oxford
- Pontzen A., Rey M. P., Cadiou C., Agertz O., Teyssier R., Read J. I., Orkney M. D. A., 2020, *arXiv e-prints*, p. arXiv:2009.03313
- Price D. J., 2008, *Journal of Computational Physics*, 227, 10040
- Price D. J., 2012, *Journal of Computational Physics*, 231, 759
- Price D. J., et al., 2018, *PASA*, 35, e031
- Raviart P. A., 1985, in Brezzi F., ed., *Numerical Methods in Fluid Dynamics*. Springer Berlin Heidelberg, Berlin, Heidelberg, pp 243–324
- Reynolds D. R., Hayes J. C., Paschos P., Norman M. L., 2009, *Journal of Computational Physics*, 228, 6833
- Rijkhorst E. J., Plewa T., Dubey A., Mellema G., 2006, *A&A*, 452, 907
- Robertson B. E., Kravtsov A. V., Gnedin N. Y., Abel T., Rudd D. H., 2010, *MNRAS*, 401, 2463
- Rosdahl J., Teyssier R., 2015, *MNRAS*, 449, 4380
- Rosdahl J., Blaizot J., Aubert D., Stranex T., Teyssier R., 2013, *MNRAS*, 436, 2188
- Rosswog S., 2015, *MNRAS*, 448, 3628
- Rosswog S., 2020a, *MNRAS*, 498, 4230
- Rosswog S., 2020b, *ApJ*, 898, 60
- Sargent W. L. W., Young P. J., Boksenberg A., Tytler D., 1980, *ApJS*, 42, 41
- Schaller M. e. a., 2018, *SWIFT: SPH With Inter-dependent Fine-grained Tasking*, *Astrophysics Source Code Library* (ascl:1805.020)
- Schaller M., Dalla Vecchia C., Schaye J., Bower R. G., Theuns T., Crain R. A., Furlong M., McCarthy I. G., 2015, *MNRAS*, 454, 2277
- Schaller M., Gonnet P., Chalk A. B. G., Draper P. W., 2016, in *Proceedings of the Platform for Advanced Scientific Computing Conference. PASC '16*. Association for Computing Machinery, New York, NY, USA, doi:10.1145/2929908.2929916, <https://doi.org/10.1145/2929908.2929916>
- Schaye J., et al., 2015, *MNRAS*, 446, 521
- Shapiro P. R., Giroux M. L., 1987, *ApJL*, 321, L107
- Skinner M. A., Ostriker E. C., 2013, *ApJS*, 206, 21
- Skinner M. A., Dolence J. C., Burrows A., Radice D., Vartanyan D., 2019, *ApJS*, 241, 7
- Smith A., Safranek-Shrader C., Bromm V., Milosavljević M., 2015, *MNRAS*, 449, 4336
- Smith A., Kannan R., Tsang B. T. H., Vogelsberger M., Pakmor R., 2020, *ApJ*, 905, 27
- Spitzer L., 1978, *Physical processes in the interstellar medium*. A Wiley-Interscience Publication, New York, NY, USA, doi:10.1002/9783527617722
- Springel V., 2005, *MNRAS*, 364, 1105
- Springel V., 2010, *MNRAS*, 401, 791
- Springel V., Hernquist L., 2002, *MNRAS*, 333, 649
- Springel V., Pakmor R., Zier O., Reinecke M., 2020, *arXiv e-prints*, p. arXiv:2010.03567
- Strömberg B., 1939, *ApJ*, 89, 526
- Susa H., 2006, *PASJ*, 58, 445
- Theuns T., Leonard A., Efsthathiou G., Pearce F. R., Thomas P. A., 1998, *MNRAS*, 301, 478
- Thomas J., 1998, *Numerical Partial Differential Equations: Finite Difference Methods*. Vol. 22, Springer Science & Business Media, New York, NY, USA
- Trac H., Pen U.-L., 2004, *New Astron*, 9, 443
- Tricco T. S., Price D. J., 2012, *Journal of Computational Physics*, 231, 7214
- Turner N. J., Stone J. M., 2001, *ApJS*, 135, 95
- Vandenbroucke B., Wood K., 2018, *Astronomy and Computing*, 23, 40
- Verhamme A., Schaerer D., Maselli A., 2006, *A&A*, 460, 397
- Verner D. A., Ferland G. J., Korista K. T., Yakovlev D. G., 1996, *ApJ*, 465, 487
- Vikas V., Hauck C. D., Wang Z. J., Fox R. O., 2013, *Journal of Computational Physics*, 246, 221
- Vila J. P., 1999, *Mathematical Models and Methods in Applied Sciences*, 09, 161
- Wadsley J. W., Keller B. W., Quinn T. R., 2017, *MNRAS*, 471, 2357
- Whalen D., Norman M. L., 2006, *ApJS*, 162, 281
- Whitehouse S. C., Bate M. R., 2004, *MNRAS*, 353, 1078
- Wise J. H., Abel T., 2011, *MNRAS*, 414, 3458
- Zheng Z., Miralda-Escudé J., 2002, *ApJ*, 578, 33
- van der Walt S., Colbert S. C., Varoquaux G., 2011, *Computing in Science Engineering*, 13, 22

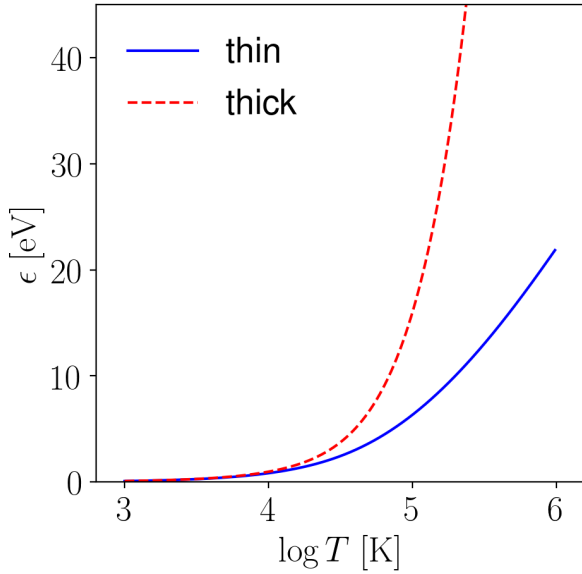


Figure A1. Injected energy, ϵ , in eV per photo-ionisation as a function of the temperature, T , of the irradiating black-body spectrum. Solid blue line is the optically thin case, dashed red line is the optically thick case.

APPENDIX A: THERMO-CHEMISTRY RATE COEFFICIENTS

The hydrogen photo-ionization rate, $\Gamma_{\gamma, \text{HI}}$ in units s^{-1} , is (e.g. Osterbrock 1989)

$$\Gamma_{\gamma, \text{HI}} = \int_{\nu_{\text{HI}}}^{\infty} \frac{4\pi J_{\nu}}{2\pi\hbar\nu} \sigma_{\gamma}(\nu) d\nu, \quad (\text{A1})$$

where $h\nu_{\text{HI}} \approx 13.6$ eV is the hydrogen binding energy, J_{ν} is the angular-averaged specific intensity I (in unit of $\text{erg cm}^{-2}\text{s}^{-1}\text{Hz}^{-1}$), and σ_{γ} is the photo-ionization cross-section of hydrogen as a function of frequency, ν , where we used the fit from Verner et al. (1996). Defining the frequency-averaged photo-ionization cross-section

$$\langle\sigma_{\gamma}\rangle \equiv \left[\int_{\nu_{\text{HI}}}^{\infty} \frac{4\pi J_{\nu}}{2\pi\hbar\nu} \sigma_{\gamma}(\nu) d\nu \right] \left[\int_{\nu_{\text{HI}}}^{\infty} \frac{4\pi J_{\nu}}{2\pi\hbar\nu} d\nu \right]^{-1}, \quad (\text{A2})$$

the photo-ionization rate of Eq. (A1) is

$$\Gamma_{\gamma, \text{HI}} = \langle\sigma_{\gamma}\rangle \int_{\nu_{\text{HI}}}^{\infty} \frac{4\pi J_{\nu}}{2\pi\hbar\nu} d\nu = \langle\sigma_{\gamma}\rangle \tilde{c}n_{\gamma}, \quad (\text{A3})$$

where the frequency-averaged photon flux is:

$$\tilde{c}n_{\gamma} \equiv \int_{\nu_{\text{HI}}}^{\infty} \frac{4\pi J_{\nu}}{2\pi\hbar\nu} d\nu. \quad (\text{A4})$$

For reference, the spectrum of a black-body (BB) with temperature $T = 10^5$ K has $\langle\sigma_{\gamma}\rangle = 1.62 \times 10^{-18} \text{cm}^2$.

The energy injected into the gas per photo-ionization is

$$\epsilon_{\gamma} = \left[\int_{\nu_{\text{HI}}}^{\infty} \frac{4\pi J_{\nu}}{\hbar\nu} \sigma_{\gamma}(\nu) (\hbar\nu - \hbar\nu_{\text{HI}}) d\nu \right] \times \left[\int_{\nu_{\text{HI}}}^{\infty} \frac{4\pi J_{\nu}}{2\pi\hbar\nu} \sigma_{\gamma}(\nu) d\nu \right]^{-1}, \quad (\text{A5})$$

in the ‘optically thin’ limit where the probability that a photon of frequency ν is responsible for the ionization is set by the photo-ionization cross-section.

In the ‘optically thick’ limit, we simply assume that every photon with $h\nu \geq h\nu_{\text{HI}}$ causes an ionization, and replace $\sigma_{\gamma} \rightarrow 1$. This increases the value of ϵ_{γ} as higher-energy photons contribute relatively more to the ionizations (e.g. Abel & Haehnelt 1999). This is only an approximation: in the optically thick-limit, hard photons with $h\nu \gg h\nu_{\text{HI}}$ tend to partially ionize gas upstream from the ionization front, which is not describe accurately by simply increasing the value of ϵ_{γ} .

In the special case of a BB spectrum, $J_{\nu} = B_{\nu}$, with

$$B_{\nu} = \frac{4\pi\hbar\nu^3}{c^2} \frac{1}{\exp(2\pi\hbar\nu/k_{\text{B}}T) - 1}, \quad (\text{A6})$$

the photo-heating per photo-ionization is

$$\frac{\epsilon_{\gamma}}{kT} = \frac{\int_{\zeta_T}^{\infty} \zeta^3 (\exp(\zeta) - 1)^{-1} \sigma_{\gamma, \text{HI}}(\zeta) d\zeta}{\int_{\zeta_T}^{\infty} \zeta^2 (\exp(\zeta) - 1)^{-1} \sigma_{\gamma, \text{HI}}(\zeta) d\zeta} - \zeta_T, \quad (\text{A7})$$

where $\zeta_T \equiv 2\pi\hbar\nu_{\text{th}}/(k_{\text{B}}T) \approx 1.578 \times 10^5 \text{K}/T$ is a dimensionless fraction. The value of ϵ_{γ} as a function of the temperature T of the BB is plotted in Fig. A1. For reference, $\epsilon_{\gamma} \approx 6.33$ eV (16.0 eV) in the optically-thin (thick) case, when $T = 10^5$ K.

Table A1 lists the interpolation formula for the ionization, recombination, heating, and cooling coefficients for hydrogen, as used in the thermo-chemistry described in section §2.8. For reference, the cooling rate due to collisional line excitation, collisional ionization, thermal Bremsstrahlung and recombination radiation (in the on-the-spot approximation), in units of $\text{erg cm}^{-3} \text{s}^{-1}$, are respectively

$$\rho \frac{du}{dt} \Big|_{\text{line}} = -x(1-x) \Gamma_{\text{line, eHI}} n_{\text{H}}^2 \quad (\text{A8})$$

$$\rho \frac{du}{dt} \Big|_{\text{Ion}} = -x(1-x) \Gamma_{\text{ion, eHI}} n_{\text{H}}^2 \quad (\text{A9})$$

$$\rho \frac{du}{dt} \Big|_{\text{Brems}} = -(1-x)^2 \Gamma_{\text{ff, eHII}} n_{\text{H}}^2 \quad (\text{A10})$$

$$\rho \frac{du}{dt} \Big|_{\text{Recomb}} = -(1-x)^2 \Gamma_{\text{B, eHII}} n_{\text{H}}^2, \quad (\text{A11})$$

whereas the photo-heating rate is

$$\rho \frac{du}{dt} \Big|_{\text{Heat}} = x\epsilon_{\gamma} \Gamma_{\gamma, \text{HI}} n_{\text{H}}. \quad (\text{A12})$$

These rates are plotted in Fig. A2, together with the thermal equilibrium values of the temperature and neutral fraction. For a gas temperature of $10^4 \text{K} \leq T \leq 10^5 \text{K}$, line cooling typically dominates the cooling rate, whereas at lower temperatures recombination cooling takes over. For reference, the case-A and case-B recombination coefficients are $\alpha_{\text{A}} = 4.29 \times 10^{-13} \text{cm}^3 \text{s}^{-1}$ and $\alpha_{\text{B}} = 2.59 \times 10^{-13} \text{cm}^3 \text{s}^{-1}$ respectively, and the collisional ionization coefficient $\beta = 1.25 \times 10^{-17} \text{cm}^3 \text{s}^{-1}$ at a gas temperature of $T = 10^4 \text{K}$.

APPENDIX B: THERMO-CHEMISTRY SUB-CYCLING

Here we analyze the computational efficiency of using sub-cycling in the thermo-chemistry solver, as described in §2.8. Note that during sub-cycling, we only need to solve a few equations (at most quadratic) for each active gas particle,

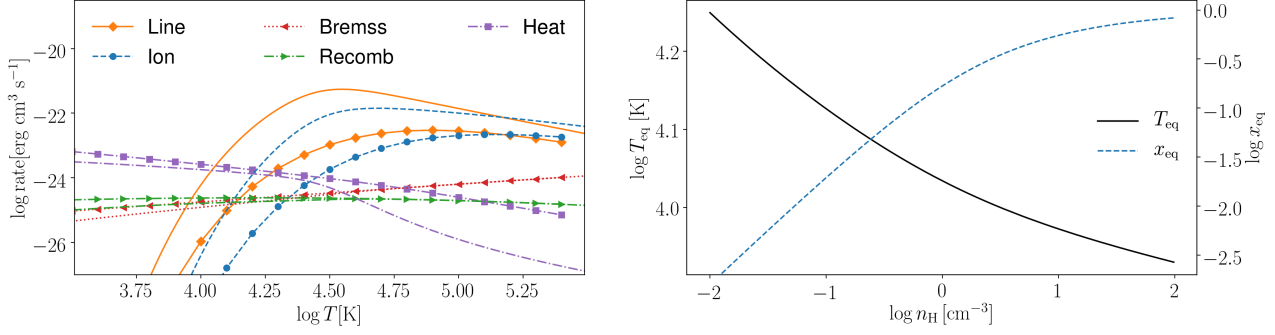


Figure A2. Left panel: Heating and cooling rates from Table A1 as a function of temperature under thermal equilibrium: collisional line cooling rate, $x(1-x)\Gamma_{\text{line,eHI}}(T)$ (orange solid), collisional ionization cooling rate, $x(1-x)\Gamma_{\text{ion,eHI}}(T)$ (blue dashed), Bremsstrahlung cooling rate, $(1-x)^2\Gamma_{\text{ff,eHII}}(T)$ (red dotted), recombination cooling rate $(1-x)^2\Gamma_{B,eHII}(T)$ (green long-dashed) and photo-heating rate, $\epsilon_\gamma x\Gamma_{\gamma,\text{HI}}/n_H$ (purple dot-dashed). Each rate is shown twice: for a hydrogen number density of $n_H = 1 \text{ cm}^{-3}$ (lines with symbols), and for $n_H = 10^{-2} \text{ cm}^{-3}$ (lines without symbols). The assumed photo-ionization rate is $\Gamma = 10^{-12} \text{ s}^{-1}$ and the energy injected per photo-ionization is $\epsilon_\gamma = 6.33 \text{ eV}$, appropriate for a black-body spectrum of temperature 10^5 K . Right panel: corresponding equilibrium temperature (T_{eq} , solid black line) and neutral fraction (x_{eq} , blue dashed line).

α_A	Recombination rate (Hui & Gnedin 1997) by fitting Ferland et al. (1992)
α_B	$= 1.269 \times 10^{-13} \text{ cm}^3 \text{ s}^{-1} \lambda^{1.503} [1.0 + (\lambda/0.522)^{0.470}]^{-1.923}$
	$= 2.753 \times 10^{-14} \text{ cm}^3 \text{ s}^{-1} \lambda^{1.5} [1.0 + (\lambda/2.740)^{0.407}]^{-2.242}$
β	Collisional ionization rate Theuns et al. (1998) modified from Cen (1992)
	$= 1.17 \times 10^{-10} \text{ cm}^3 \text{ s}^{-1} T^{1/2} \exp(-157809.1/T)(1 + T_5^{1/2})^{-1}$
$\Gamma_{\text{ion,eHI}}$	Collisional ionization cooling rates Theuns et al. (1998) modified from Cen (1992)
	$= 2.54 \times 10^{-21} \text{ erg cm}^3 \text{ s}^{-1} T^{1/2} \exp(-157809.1/T)(1 + T_5^{1/2})^{-1}$
$\Gamma_{\text{line,eHI}}$	Collisional excitation cooling rates Theuns et al. (1998) modified from Cen (1992)
	$= 7.5 \times 10^{-19} \text{ erg cm}^3 \text{ s}^{-1} \exp(-118348/T)(1 + T_5^{1/2})^{-1}$
$\Gamma_{A,eHII}$	Recombination cooling rates taken from Hui & Gnedin (1997) (fitted from Ferland et al. (1992))
$\Gamma_{B,eHII}$	$= 1.778 \times 10^{-29} \text{ erg cm}^3 \text{ s}^{-1} \text{ K}^{-1} T \lambda^{1.965} [1.0 + (\lambda/0.541)^{0.502}]^{-2.697}$
	$= 3.435 \times 10^{-30} \text{ erg cm}^3 \text{ s}^{-1} \text{ K}^{-1} T \lambda^{1.970} [1.0 + (\lambda/2.250)^{0.376}]^{-3.720}$
$\Gamma_{\text{ff,eHII}}$	Bremsstrahlung cooling rate Theuns et al. (1998) modified from Cen (1992) and Spitzer (1978)
	$= 1.42 \times 10^{-27} \text{ erg cm}^3 \text{ s}^{-1} T^{1/2} \{1.1 + 0.34 \exp(-[5.5 - \log(T)]^2/3)\}$

Table A1. Coefficients for heating and cooling of hydrogen. $T_n = T/(10^n \text{ K})$ and temperature T is in K. $\lambda = 315614 \text{ K}/T$. If the on-the-spot approximation is applied, we used the case B recombination cooling (in Eq. 41). Otherwise, the case A recombination cooling is used.

making the computational cost small compared to calculating hydrodynamical or gravitational forces, or performing the radiative transfer, all of which require loops over neighbouring particles and potentially communication between compute nodes. Therefore, the number of sub-cycling steps per global time-step is a measure of the efficiency of sub-cycling.

We plot this ratio for the single gas particle test (see §2.8.3) in Fig. B1, and for the static 3D Strömgren test (see §3.2) in Fig. B2. The number of sub-cycling steps per global time-step is typically highest in *nearly* neutral regimes, where the ratio can be up-to an order of magnitude. This is because the gas in this regime is far from equilibrium, and the sub-cycle time-step is limited by the photo-ionization time scale, $\tau_i = 1/\Gamma_{\gamma,\text{HI}}$, which can be *much* shorter than the global time-step set by the CFL condition. Once the gas is highly ionized, sub-cycle time-step is usually set by the recombination time-scale, which is typically much longer than τ_i . In addition, the gas may be in ionization equilibrium or even thermal equilibrium, so that the chemistry time-step is long. In the kind of astrophysical application that we have in mind, for example reionization simulations, sub-cycling is

essential since otherwise the short time-step required in gas being over run by an ionization front will grind the code to a halt. Finally, our sub-cycling scheme parallelizes well, since it does not require any communication.

APPENDIX C: ANALYTIC SOLUTION OF THE STRÖMGREN SPHERE

In the classical Strömgren sphere problem (Strömgren 1939), a source emitting ionizing photons at a constant rate \dot{N}_γ is embedded in a spherical cloud, initially filled with completely neutral hydrogen atoms with density $n_{\text{HI}} = n_H$. As the source switches on, an ionization front expands around the source, and the gas inside the ionization front, radius R_I , will be mostly ionized, $x \equiv n_{\text{HI}}/n_H \ll 1$, and outside R_I will be mostly neutral.

The equations describing the evolution of the neutral fraction and photon density of such an idealized system are

$$\frac{\partial n_{\text{HI}}}{\partial t} = -n_{\text{HI}} c \sigma_\gamma n_\gamma + n_e n_{\text{HII}} \alpha_A - n_e n_{\text{HI}} \beta, \quad (\text{C1})$$

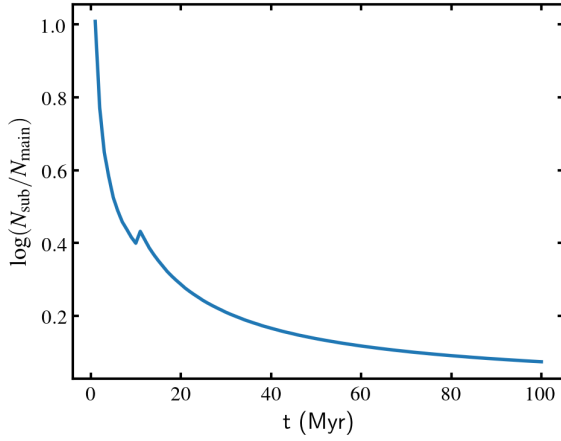


Figure B1. The number of sub-cycles per global time-step in the single particle photo-ionization heating test, described in §2.8.3, as a function of time. The global time-step $\Delta t_{\text{main}} = 0.1$ Myr. This ratio can be up-to a factor of ten initially, reducing to tens of percents after the gas reaches equilibrium.

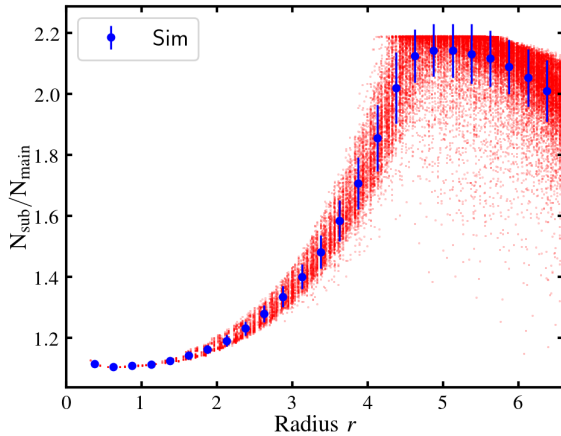


Figure B2. The number of sub-cycles per global time-step for the variable temperature Strömgren sphere test with static gas particles described in §3.2. This ratio is plotted for every SPH particle (red dots) as a function of its distance to the centre, at time $t = 100$ Myr; blue points with error bars show the mean and variance in radial bins. The speed-up due to sub-cycling is around a factor of two, mainly near the location of the ionization front.

$$\begin{aligned} \frac{\partial n_\gamma}{\partial t} &= -n_{\text{HI}}\sigma_\gamma n_\gamma + n_e n_{\text{HII}}(\alpha_A - \alpha_B) + S_\gamma, \\ &= \frac{\partial n_{\text{HI}}}{\partial t} - \alpha_B n_e n_{\text{HII}} + S_\gamma. \end{aligned} \quad (\text{C2})$$

As a first approximation to describe such a system, we assume that the gas inside R_I is fully ionized, $x = 0$, and outside R_I is fully neutral, $x = 1$, and that the ionization front is infinitely sharp. We further neglect collisional ionization, setting $\beta = 0$. In this case, $n_{\text{HI}}(r) = n_{\text{HI}}\Theta(R_I - r)$, where $\Theta(x)$ is the step function. Integrating each term of

Eq. (C2) over the volume centered at the source, we find

$$\begin{aligned} \int \frac{\partial n_{\text{HI}}}{\partial t} dV &= \int \frac{\partial}{\partial t} [n_{\text{HI}}\Theta(R_I - r)] dV \\ &= n_{\text{HI}} \int \delta(R_I - r) \frac{\partial R_I}{\partial t} dV \\ &= -4\pi R_I^2 n_{\text{HI}} \frac{\partial R_I}{\partial t} \\ \int \alpha_B n_e n_{\text{HII}} dV &\approx \alpha_B n_{\text{H}}^2 \frac{4\pi}{3} R^3 \\ \int S_\gamma dV &= \dot{N}_\gamma. \end{aligned} \quad (\text{C3})$$

Combined, these yield the well-known equation,

$$\dot{N}_\gamma = 4\pi R_I^2 n_{\text{H}} \frac{\partial R_I}{\partial t} + \alpha_B n_{\text{H}}^2 \frac{4\pi}{3} R_I^3, \quad (\text{C4})$$

with solution

$$R_I(t) = R_S [1 - \exp(-t/\tau_r)]^{1/3}. \quad (\text{C5})$$

Here, the recombination time $\tau_r = (\alpha_B n_{\text{H}})^{-1}$ and the Strömgren radius

$$R_S \equiv \left(\frac{3\dot{N}_\gamma}{4\pi\alpha_B n_{\text{H}}^2} \right)^{1/3}. \quad (\text{C6})$$

For times $t \gg \tau_r$, and greater than the ionization time scale τ_i ,

$$\tau_i \equiv \frac{(4\pi/3)n_{\text{H}}\dot{N}_\gamma}{R_S^3}, \quad (\text{C7})$$

the ionization front reaches an equilibrium location where ionizations balance recombinations.

To derive the profile of the hydrogen neutral fraction in equilibrium analytically, we work with the time independent equation in the on-the-spot approximation, $\alpha_A \rightarrow \alpha_B$,

$$\frac{\partial n_\gamma}{\partial t} = -\nabla \cdot \mathbf{f}_\gamma - n_{\text{HI}}\sigma_\gamma n_\gamma = 0, \quad (\text{C8})$$

In spherical symmetry (and neglecting the scattered radiation), $\mathbf{f}_\gamma = n_\gamma c \hat{\mathbf{r}}$ so that

$$\nabla \cdot (cn_\gamma \hat{\mathbf{r}}) + n_{\text{HI}}\sigma_\gamma n_\gamma = 0. \quad (\text{C9})$$

Writing this in spherical coordinates yields

$$\frac{1}{r^2} \frac{\partial}{\partial r} (r^2 n_\gamma) + n_{\text{HI}}\sigma_\gamma n_\gamma = 0, \quad (\text{C10})$$

with formal solution

$$n_\gamma = \frac{\dot{N}_\gamma}{4\pi c r^2} \exp\left(-\int_0^r n_{\text{HI}}(r')\sigma_\gamma dr'\right). \quad (\text{C11})$$

This derivation implicitly assumes that the mean free-path of photons is much less than R_S , which should be a good approximation for typical HII regions.

The steady-state neutral hydrogen profile follows by balancing ionizations and recombinations, *i.e.* substituting the previous relation into Eq. (C1) and setting $\partial n_{\text{HI}}/\partial t = 0$,

$$\frac{x\sigma_\gamma \dot{N}_\gamma}{4\pi r^2} \exp(-\tau(r)) = (1-x)^2 n_{\text{H}}\alpha_B - x(1-x)\beta n_{\text{H}}^2, \quad (\text{C12})$$

where the optical depth is given by

$$\tau(r) = n_{\text{H}}\sigma_\gamma \int_0^r x(r') dr'. \quad (\text{C13})$$

The nature of the solution is brought out better by casting these equations in dimensionless form,

$$\begin{aligned} \frac{\tau_S x}{q^2} \exp(-\tau) &= 3(1-x)^2 - 3\frac{\beta}{\alpha_B} x(1-x) \\ \tau &= \tau_S \int_0^q x(q') dq', \end{aligned} \quad (\text{C14})$$

where the dimensionless radius $q \equiv r/R_s$, and the ‘Ström-gren optical depth’ $\tau_S \equiv n_H \sigma_\gamma R_s$. This is an integral equation for the neutral fraction, $x(q)$. We follow Altay & Theuns (2013) to convert this into an easier to integrate differential equation: take the logarithm of both sides and differentiate with respect to q , which yield

$$\left[\frac{1}{x} + \frac{2(1-x) - (1-2x)\beta/\alpha_B}{(1-x)^2 - x(1-x)\beta/\alpha_B} \right] \frac{dx}{dq} = \tau_S x + \frac{2}{q}, \quad (\text{C15})$$

with boundary condition for $q \rightarrow 0$

$$x \rightarrow \frac{3}{\tau_S} q^2. \quad (\text{C16})$$

Provided that collisional ionizations can be neglected, the differential equation simplifies to

$$\frac{dx}{dq} = \frac{x(1-x)}{1+x} \left(\tau_S x + \frac{2}{q} \right), \quad (\text{C17})$$

which shows that there is a one-parameter family of solutions that are characterised by the value of τ_S . The numerical integration of Eq. (C15) with its associated boundary conditions is plotted as the line labelled ‘Analytic’ in Fig. 8.

APPENDIX D: MOMENT DERIVATIONS

This short Appendix aims to elucidate the analogy between taking moments of the Boltzmann equation to derive the fluid equations, and taking moments of the RT equation to derive the moment equations for radiation. The collisional Boltzmann equation is

$$\frac{\partial}{\partial t} f + \mathbf{v} \cdot \frac{\partial}{\partial \mathbf{x}} f + \mathbf{a} \cdot \frac{\partial}{\partial \mathbf{v}} f = \left(\frac{Df}{Dt} \right)_{\text{coll}}, \quad (\text{D1})$$

where the right hand side (R.H.S.) is the collision term, and the distribution function f is a function of position, \mathbf{x} , velocity \mathbf{v} , and time, t . We will suppress this dependency to avoid clutter. Moments of the equation are derived by multiplying Eq. (D1) with some function $Q(\mathbf{v})$ and integrating over velocities,

$$\begin{aligned} \frac{\partial}{\partial t} \int Q(\mathbf{v}) f d\mathbf{v} &+ \frac{\partial}{\partial \mathbf{x}} \cdot \int \mathbf{v} Q(\mathbf{v}) f d\mathbf{v} \\ &+ \mathbf{a} \cdot \int \left\{ \frac{\partial}{\partial \mathbf{v}} Q(\mathbf{v}) f - f \frac{\partial}{\partial \mathbf{v}} Q(\mathbf{v}) \right\} d\mathbf{v} \\ &= \int Q(\mathbf{v}) \left(\frac{Df}{Dt} \right)_{\text{coll}} d\mathbf{v}. \end{aligned} \quad (\text{D2})$$

The first term in curly brackets is the flux Qf evaluated at the integration limits of the velocity. Provided we integrate over all velocities, we can assume that f goes to zero sufficiently fast that this term vanishes. Writing the velocity as $\mathbf{v} = \mathbf{V} + \mathbf{w}$, where \mathbf{V} is the mean and \mathbf{w} is the random component of \mathbf{v} , the density, momentum, pressure and viscous

stress tensor, are defined as

$$\begin{aligned} \rho &\equiv m \int f d\mathbf{v} \\ P &\equiv \frac{1}{3} \int w^2 f d\mathbf{v} \\ \Pi^{ij} &\equiv P \delta^{ij} - \int w^i w^j f d\mathbf{v}. \end{aligned} \quad (\text{D3})$$

The fluid equations then follow by realising that integrals over collision term on the R.H.S. of Eq. (D2) vanish for functions Q that are conserved during collisions. This is the case for $Q = m$ (the particle’s mass), and $Q = m\mathbf{v}$ (the particle’s momentum), which then yield the first two moment equations (the continuity and Euler equations),

$$\begin{aligned} \frac{\partial}{\partial t} \rho &+ \frac{\partial}{\partial \mathbf{x}} \cdot \rho \mathbf{V} = 0 \\ \frac{\partial}{\partial t} \rho \mathbf{V}^i &+ \frac{\partial}{\partial \mathbf{x}^j} \left(\rho \mathbf{V}^j + P \delta^{ij} - \Pi^{ij} \right) - \rho \mathbf{a}^i = 0. \end{aligned} \quad (\text{D4})$$

Contrast this derivation with taking moments of the radiative transfer equation (e.g Levermore & Pomraning 1981)¹⁹,

$$\frac{1}{c} \frac{\partial}{\partial t} I + \mathbf{n} \cdot \frac{\partial}{\partial \mathbf{x}} I = \left(\frac{DI}{Dt} \right)_{ss}, \quad (\text{D5})$$

where the specific intensity I is a function of position, \mathbf{x} , direction, θ, ϕ in spherical coordinates, frequency, ν , and time, t . The Cartesian coordinates of the unit vector in direction \mathbf{n} are $\mathbf{n} = (\sin(\theta) \cos(\phi), \sin(\theta) \sin(\phi), \cos(\theta))$. The R.H.S. now represents photon sources and sinks.

We proceed as before, by multiplying with some function $Q(\theta, \phi)$, which can be a scalar or a tensor, and integrating the RT equation over solid angle $d\Omega$, but not over frequency. We then take $Q = 1$ and $Q = \mathbf{n}$ to yield the first two moment equations,

$$\begin{aligned} \frac{\partial}{\partial t} E + \frac{\partial}{\partial x^i} F^i &= \int \left(\frac{DI}{Dt} \right)_{ss} d\Omega \\ \frac{1}{c^2} \frac{\partial}{\partial t} F^i + \frac{\partial}{\partial x^j} \mathbb{P}^{ij} &= \int \mathbf{n}^i \left(\frac{DI}{Dt} \right)_{ss} d\Omega \\ E &= \frac{1}{c} \int I d\Omega = 3P \\ \mathbb{P}^{ij} &\equiv P \delta^{ij} - \Pi^{ij} \\ \mathbf{F}^i &= \int \mathbf{n}^i I d\Omega \\ \Pi^{ij} &= P \delta^{ij} - \int \mathbf{n}^i \mathbf{n}^j I d\Omega. \end{aligned} \quad (\text{D6})$$

Here, E is the energy density, P the radiation pressure, \mathbf{F} the flux, and the trace-less tensor Π is the radiation equivalent of the viscous stress tensor. These are the moment equations of Eq. (8) and Eq. (9) in the fluid frame, $\mathbf{v} = 0$.

In the special case where the sources plus sinks term have the form of isotropic absorption, $(DI/Dt)_{ss} = -\kappa I$,

¹⁹ Here we only briefly illustrate the concept, so we suppress the acceleration term of Eq. (D5) for simplicity. This missing term is included in §2.3 which is based on the derivation by Buchler (1983). Gnedin & Ostriker (1997) (see also e.g. Petkova & Springel 2009; Cantalupo & Porciani 2011) did include the rate of change of frequency in Eq. (D5) but only to include cosmological redshifting of photons while neglecting changes of radiation energy density from gas velocity.

where κ is the isotropic absorption coefficient, the sink terms in Eq. (D6) are $-\kappa E$ and $-\kappa \mathbf{F}$ for the first and second equation, respectively. Provided that the term $(1/c^2)\partial \mathbf{F}/\partial t$ can be neglected, the moment equations then combine to

$$\frac{\partial}{\partial t} E = \nabla \cdot \left[\frac{1}{\kappa} \nabla \mathbb{P} \right] - \kappa E, \quad (\text{D7})$$

which is a diffusion equation. In the isotropic case, $\Pi^{ij} = 0$, and a Gaussian package of the form $E(\mathbf{x}, t) = (2\pi\sigma^2)^{-3/2} \exp[-x^2/(2\sigma^2)] \exp(-\kappa t)$ is a solution, spreading out as $\sigma^2(t) = \sigma^2(t=0) + 2t/(3\kappa)$ while dimming, $\propto \exp(-\kappa t)$. This paper has been typeset from a \LaTeX

\LaTeX file prepared by the author.